INITIATION, ABLATION, PRECURSOR FORMATION, AND INSTABILITY ANALYSIS OF THIN FOIL LINER Z-PINCHES

A Dissertation

Presented to the Faculty of the Graduate School

of Cornell University

in Partial Fulfillment of the Requirements for the Degree of

Doctor of Philosophy

by

Isaac Curtis Blesener

August 2012

INITIATION, ABLATION, PRECURSOR FORMATION, AND INSTABILITY ANALYSIS OF THIN FOIL LINER Z-PINCHES

Isaac Curtis Blesener, Ph.D.

Cornell University 2012

This dissertation presents the results of mostly experimental work studying the early-time behavior of thin foil liners as compared to wire-array Z-pinches. It involves three studies, covering initiation, ablation and precursor formation, and instability analysis.

Initiation was studied by observing the optical emission of various thickness (0.6-23.5 μm Cu) liners using a streak camera. It was found that thinner liners initiated sooner, more quickly, and more uniformly than thicker liners. This correlated well with both an increase in instantaneous dJ/dt at the time of first emission as well as the inductive voltage at the time of first emission. The threshold for uniform initiation was $dJ/dt > 3.5 \times 10^{16} Acm^{-2}s^{-1}$. Uniform initiation is important for liners because nonuniformities could lead to enhanced instabilities and poor liner performance (compression, x-ray production, etc.).

Ablation and precursor formation of wire-arrays (16x75 μm Cu) and liners (6 μm Cu) were studied using r-θ density maps and radial mass profiles created by an axial X pinch radiography diagnostic. These images show very strong differences in this stage of the Z-pinch. Wire-arrays develop complex, azimuthally varying ablation structures that lead to dense precursors. Liners, however, show significantly reduced and azimuthally uniform ablation leading to an order of magnitude less dense precursor on axis. This is likely due to the discrete versus continuous nature of wire-arrays versus liners. With wire-arrays, plasma that

is created on the outside of the wires can reach the array axis by being swept through the gaps between the stationary wire cores. In contrast, liners have no "gaps" for plasma to flow through. Therefore, any plasma that is created on the outside of the liner is trapped there until the bulk of the liner moves with the implosion. Consequently, only the plasma that is created on the inside of the liner is able to contribute to precursor formation. This is an important result because reduced precursor formation is important for fuel compression and heating in MagLIF. Less precursor can also lead to enhanced x-ray production because there is less mass on axis to cushion the conversion of kinetic energy into x-rays during the implosion and stagnation phases.

Finally, in the instability studies, it was observed in laser shadowgraph images that liners develop a much larger amplitude instability on their outside surface as compared to wire-arrays. This is an important discovery and could be detrimental to liner performance (compression, x-ray production, etc.) because it could lead to enhanced magnetic Rayleigh-Taylor (MRT) instability during the implosion phase. The reason for the larger instability in liners is again probably due to the fact that plasma builds up on the outside of the liners with no where to go.

A possible source of the enhanced instability was found using 2D (xy) PERSEUS simulations comparing the results of MHD and Hall MHD simulations. The instability only developed in the Hall MHD case. The 2D nature of the simulation, along with all simulation parameters being equal between the two cases, rules out the possibility of MRT or m=0 for the cause of the instability (in the simulation). It was found that the Hall term was responsible for causing a shear-flow instability that developed later in time to resemble the experimental results.

BIOGRAPHICAL SKETCH

Isaac Curtis Blesener was born in Litchfield, MN on September 24, 1982, to Charlie and Kathleen Blesener. He has two older brothers, Lucas and Dominic, and is married to Kate Blesener.

Isaac graduated from Elk River Area High School in 2001. He received his BS and Diplom-Ingenieur degree from the Milwaukee School of Engineering and the Fachhochschule Lübeck, Germany in 2005. That summer, he entered the MS/Ph.D. program at Cornell University with the Laboratory of Plasma Studies where he met his wife Kate and worked as a Graduate Research Assistant for Professor Bruce Kusse.

Isaac is an auxiliary percussionist, an amateur illusionist, a full-time scientist, a passable mechanic, a barbecue enthusiast, a skeptic, a science fiction fan, a husband, a pet owner, and a human being.

To my loving wife, Kate.

I can't imagine my time at Cornell without you.

ACKNOWLEDGEMENTS

The successful completion of this research and dissertation would not have been possible without the support of many individuals. In particular, my special committee chair and thesis advisor, Professor Bruce Kusse has been instrumental in my professional development. He always knows when I need a push in the right direction and when to let me figure things out in my own time.

I would also like to thank my additional committee members, Professors Charles Seyler and Richard Lovelace, for helping me though this process, particularly while taking your courses and in discussions about PERSEUS.

I would also like to thank David Hammer, John Greenly, Pierre Gourdain, Sergei Pikuz, and Tania Shelkovenko for their help throughout my time at the Laboratory of Plasma Studies. You have taught me experimental techniques, helped me write papers, and generally helped me become a better scientist.

Harry Wilhelm and Todd Blanchard have helped me in the creation of many experimental setups and helped ensure both COBRA and XP behaved well (as best anyone can) for my experiments.

My friends and fellow graduate students have contributed to my success, both with direct help and advice and through helping me not take things too seriously. Thank you for that.

Brent Blue of General Atomics and Mike Cuneo and Dan Sinars of Sandia National Laboratories were extremely helpful in the initial planning stages of my liner experiments.

Pace VanDevender was instrumental in pointing me in the direction of liner initiation. His research into the history of the SCOPIO plasma initiation experiments was the motivation for my initiation work.

I thank the U.S. Department of Energy, the National Nuclear Security Administration, and Sandia National Laboratories for their financial support of my graduate work. The projects presented in this dissertation were funded by Sandia National Laboratories Contract No. AO258 and by the Stewardship Science Academic Alliances program of the National Nuclear Security Administration under DOE Cooperative Agreement No. DE-FC03-02NA00057.

Finally, I would like to thank my family and friend for all their love and support throughout my life. I am particularly grateful to my wife, Kate: the best thing that happened to me at Cornell.

TABLE OF CONTENTS

LIST OF TABLES

LIST OF FIGURES

CHAPTER 1

INTRODUCTION

1.1 Motivation & Applications

Wire-array and liner Z-pinches are able to produce extremely powerful x-ray sources (>2×10^{14} W with of energies ~2×10^{6} J) with great efficiency ($\gtrsim$15% conversion from stored electrical energy to radiated x-ray energy)[1, 2, 3]. In addition to their x-ray production, Z-pinches produce extremely hot and dense plasmas, making them very attractive for applications to inertial confinement fusion (ICF)[4, 5, 6, 7, 8, 9, 10], magnetized liner inertial fusion (MagLIF)[11, 12], high-energy-density physics (HEDP)[13, 14, 10], laboratory astrophysics[15, 16, 17], and radiation sciences[18].

A Z-pinch is a cylindrical distribution of mass that is driven with a low impedance (typically less than 1Ω) high power (10^{10} – 10^{13} W) pulsed power driver. The most simple configuration to envision would be the foil liner Z-pinch (see Fig. 1.1(a)), which consists of a solid cylindrical shell of material[19, 20]. However, until recently, it was impractical to construct thin foil liners that were both thin enough and smooth enough for use. This led to much of the research from the 1970's to the 1990's focusing on wire-array and gas puff Z-pinches[21, 22, 23]. Wire-arrays (see Fig. 1.1(b)) consist of thin wires (typically 5 – 10 μm) arranged in a circle, similar to a foil liner, although not a continuous distribution of mass[24, 25]. Gas puffs (see Fig. 1.1(c)) typically consist of a low density noble gas that can be distributed cylindrically; again, similar to a foil liner, but with a lower density, more diffuse mass distribution[26, 27]. In the mid 1990's, it was found that by increasing the number of individual wires (up

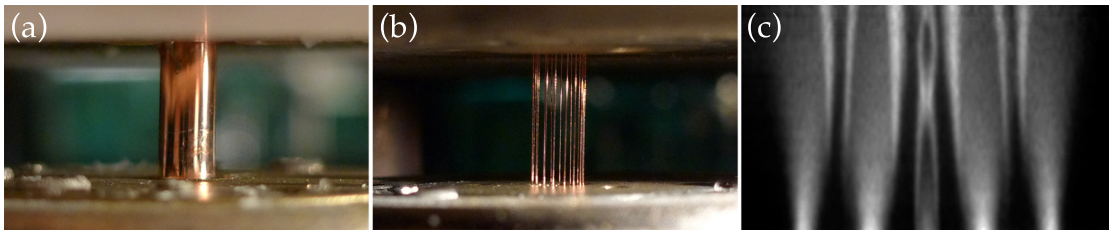

Figure 1.1: Examples of different types of Z-pinches. (a) 4 mm diameter, 6 μm thick copper liner, (b) 16 wire, 75 μm copper wire-array, and (c) laser fluorescence of a 3-layer gas puff, courtesy of Nianshen Qi.

to a point) in a wire-array Z-pinch, while keeping the total array mass roughly constant, significantly increased the x-ray radiation power[28]. This finding led to a focus on high-wire-number Z-pinches at the national labs leading into the early 2000's.

In earlier experiments during the 1970's and 1980's, it was found that the x-ray power from a Z-pinch scaled with the output current as I^4[29]. This incredible scaling factor led to the construction of higher current pulsed power generators. Another scaling parameter for Z-pinches is the Pi parameter[14]

$$\Pi = \frac{\mu I_{max}^2 \tau^2}{4\pi \hat{m} r_0^2} \tag{1.1}$$

where μ is the permeability of the material, I_{max} is the maximum output current of the driver, τ is the time in which the current reaches its maximum, $\hat{m}$ is the mass per unit length of the Z-pinch, and r_0 is the initial radius of the Z-pinch. If two Z-pinches have the same Pi parameter (and their drivers have roughly the same shape, regardless of τ or I_{max}), their implosions will occur at the same relative time, t/τ. For a sine-squared current pulse, it can be shown that the kinetic energy of an implosion is maximized when the parameter Π is approximately

4[14]. Using $\Pi = 4$ and solving Equation 1.1 for $\hat{m}$ we have:

$$\hat{m} = \frac{\mu I_{max}^2 \tau^2}{16\pi r_0^2} \tag{1.2}$$

Equation 1.2 shows that in order to properly match the load to the driver as one increases the current of the driver (to increase the x-ray power), the mass per unit length of the Z-pinch must increase as I_{max}^2. However, as newer, higher current drivers were built and more massive Z-pinches were used, the I^4 scaling turned into more like I^2 scaling[30], indicating that something in the pinch physics was no longer working with the more massive loads.

One thing that has been observed is that as the mass of the Z-pinch increased, the amount of precursor mass also increased. The increase in precursor mass acts as a cushion to soften the final conversion of kinetic and magnetic energy into x-ray energy during the final implosion process. If one can find a way to increase the Z-pinch mass while keeping the precursor mass relatively small, it may be possible to improve the x-ray power output. One possible way to accomplish this is to use foil liners instead of wire-arrays.

The hypothesis lies with the differences in magnetic field topology that the different mass distributions produce (see Fig. 1.2). During the initiation and ablation phases of the pinch, the current from each wire in the array creates its own magnetic field (local field) that dominates the global field created by the summation of all the currents. Foil liners, however, only have the global field on the outside of the surface, with no local fields at all. Depending on the skin depth of the liner, some global field can be present on the inside of the foil. In wire-arrays, ablation occurs roughly uniformly around the cross-section of a wire because of the influence of the local field. Material that is ablated on the outside of the wire, gets swept around the wire by global $\vec{J} \times \vec{B}$

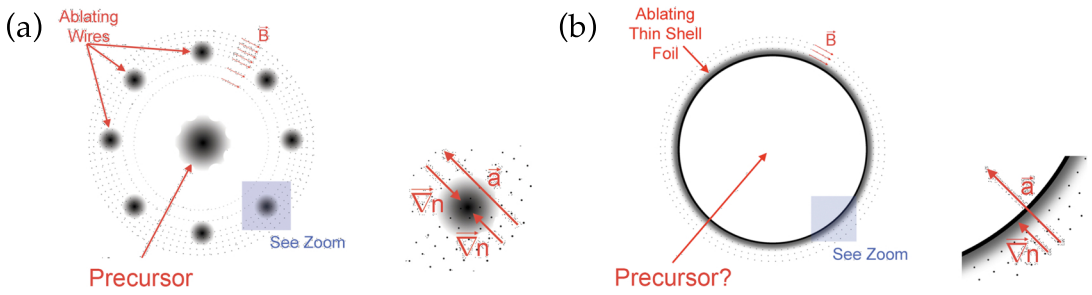

Figure 1.2: Topology differences between (a) wire-array and (b) foil liner Z-pinches.

forces while material on the inside also gets propogated to the axis. In contrast, material that is ablated on the outside of foil liners has no path for it to get "swept around" to the axis, so the only material that makes it to the axis is ablated material from the inside of the surface. This theory would suggest that foil liners would develop much less precursor mass and could, therefore, be a way to increase the scaling of x-ray power with current for Z-pinches. The objective of the research presented here is to better understand foil liners and how they compare to equivalent wire-arrays. Research includes ways to initiate foils as uniformly as possible, ablation characteristics and precursor formation of liners vs. wire-arrays, and instability studies of liners vs. wire-arrays.

1.2 Magnetically Self-Focussing Streams: The Z-Pinch

Current flowing in a conductor tends to have a self-focussing nature due to magnetic forces. This usually occurs in a plasma (e.g. lightning bolt or welding arc) but can also occur in a liquid or solid metal (e.g. lighting rod or various conductors (Fig. 1.3) inside a pulsed-power generator). An equilibrium condition, between thermal pressure and magnetic pressure, can be achieved and

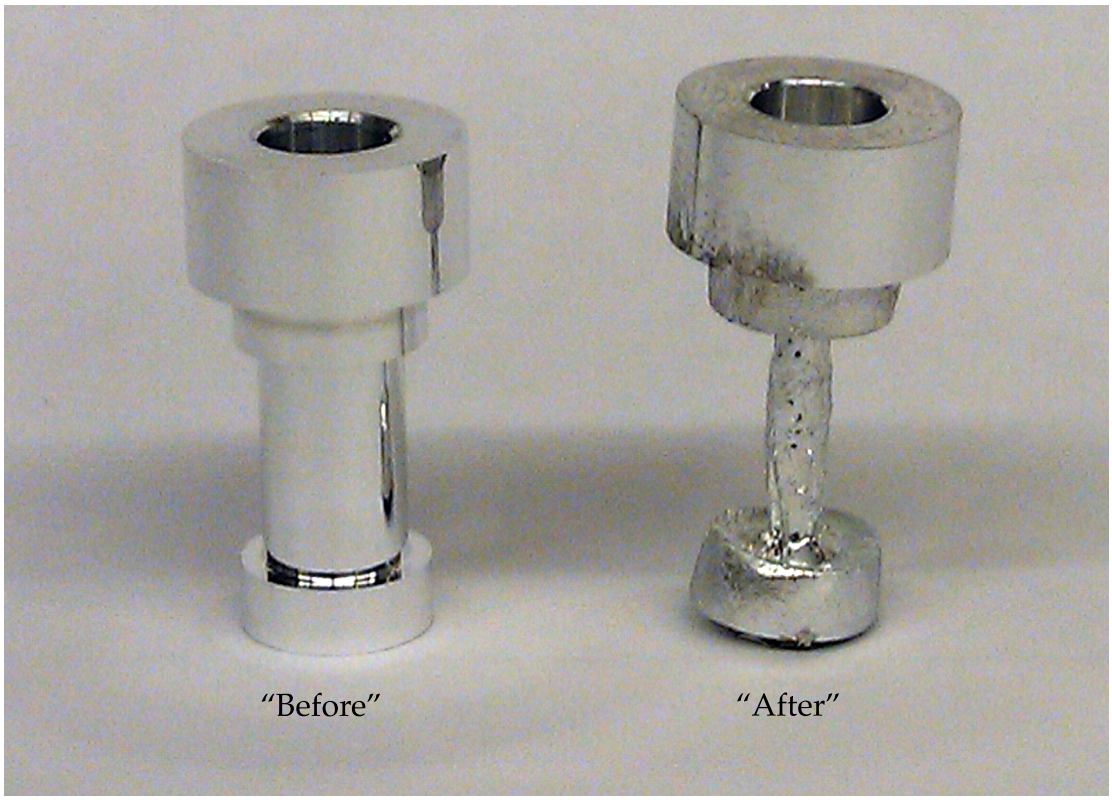

Figure 1.3: "Before" and "After" pictures of a 6.3 mm diameter, 300 μm wall thickness aluminum liner fired on COBRA (note: not the actual before and after, just similar targets). Because the load was entirely too massive to implode and stagnate, it merely liquified and self pinched.

was orignally characterized by W. H. Bennett in 1934[31].

In his paper, Bennett describes a cylindrically symmetric stream with the Z-axis as the axis of symmetry and direction of current flow (hence Z-pinch). Using only a singly ionized species, Bennett's Eq. 12 describes the number of particles (either electrons or oppositely flowing positives (i.e. ions)) per unit length of the stream, λ_0, and the critical current to achieve equilibrium, i_0, as:

$$\lambda_0 = \frac{c^2 \cdot 2K\,(T_1 + T_2)}{e^2\,(u+v)^2} \quad (/cm) \tag{1.3}$$

$$i_0 = \frac{c^2 \cdot 2K\,(T_1 + T_2)}{e\,(u+v)} \quad (statamperes) \tag{1.4}$$

where c is the speed of light, K is the Boltzmann constant, T_1 and T_2 are the transverse temperatures of the electrons and ions, repsectively, e is the electron charge, and u and v are the electron and ion velocities, respectively (with everything in cgs units).

Now, because I'm an experimentalist (and living in the 21^{st} century), my brain hurts when I think of statamperes and other fanciful cgs units. Therefore, I will show what these equations look like in SI as well as somewhat more common symbols for Bennett's equations. Equation 1.4 becomes:

$$\frac{\mu_0 I_B^2}{4\pi} = 2N_e(1 + 1/Z)kT \quad (N) \tag{1.5}$$

where μ_0 is the permeability of free space, I is the total current, Z is the average ionization state, and we have assumed a plasma that consists of N_e electrons and N_e/Z ions per unit length and uniform temperature T.

As stated earlier, Bennett described an equilibrium condition, where his i_0 or our I_B represents the critical current to exactly balance the magnetic field pressure with the thermal pressure. With less current, the plasma will expand, and with more current, the plasma will pinch.

The differential form of the Bennett relation (in SI units) is given by

$$\nabla\left(p + \frac{B^2}{2\mu_0}\right) = \frac{(\mathbf{B}\cdot\nabla)\,\mathbf{B}}{\mu_0} \tag{1.6}$$

where $p = p_e + p_i$ is the total pressure and B is the self-induced magnetic field. Equation 1.5 is essentially Equation 1.6, under the constraints that the current flow is restricted to only the z-direction (Z-pinch), and then integrated over the cylindrical volume. I leave it as an exercise for the reader to find the integral forms of the remaining two one-dimensional cases (θ-pinch and screw-pinch).

R. S. Pease[32] and S. I. Braginskiĭ[33] furthered Bennett's work by considering power balance as opposed to pressure balance. The critical current that balances resistive (Joule) heating with bremsstrahlung radiation is

$$I_{PB} = \left(\frac{8 \ln \Lambda}{\alpha F_b}\right)^{1/2} 2\left(1 + \frac{1}{Z}\right) I_A \tag{1.7}$$

where $\ln \Lambda$ is the Coulomb logarithm, α is the fine structure constant, F_b is taken to be $\sqrt{2\pi/27}$[34], and I_A is Alfvén-Lawson current defined as $I_A = ec/r_e$, where e is the electron charge and r_e is the classical electron radius. A derivation of Equation 1.7 can be found in Ref [35].

Equation 1.7 defines the critical current at which Joule heating is balanced by bremsstrahlung losses. If the current exceeds this equality, the Z-pinch will radiatively collapse. Conversely, if the current is less than this equality, the plasma will heat up, increasing thermal pressure, and requiring a larger Bennett current to maintain equilibrium.

CHAPTER 2

COBRA

2.1 Pulsed Power Basics

Z-pinches are generally driven by a very high current in a very short amount of time. In order to achieve this, a pulsed power generator is typically used. A very simple explanation of pulsed power would be to consider pulse compression while keeping the total energy roughly constant. A series of capacitors arranged in one or more Marx banks is charged (usually via a standard wall outlet) for several minutes. The energy stored during those several minutes is then transferred to lower and lower capacitance transmission lines with each transfer compressing the pulse in time. What took several minutes to transfer the initial energy is transferred in a few microseconds, then a few hundred nanoseconds, then 50 or 100 nanoseconds when it is finally transferred to the load. See Fig. 2.1 for an example of pulse compression. During this pulse compression, the total energy stored is roughly constant, thus dramatically increasing the power of the pulse. In this way, it is possible to deliver multiple terawatts of power to a load, but only for a very short amount of time. Given that the energy usage of the entire United States is 4,369 TWh/yr (0.5 TW average), it goes without saying that these drivers are anything but steady-state devices.

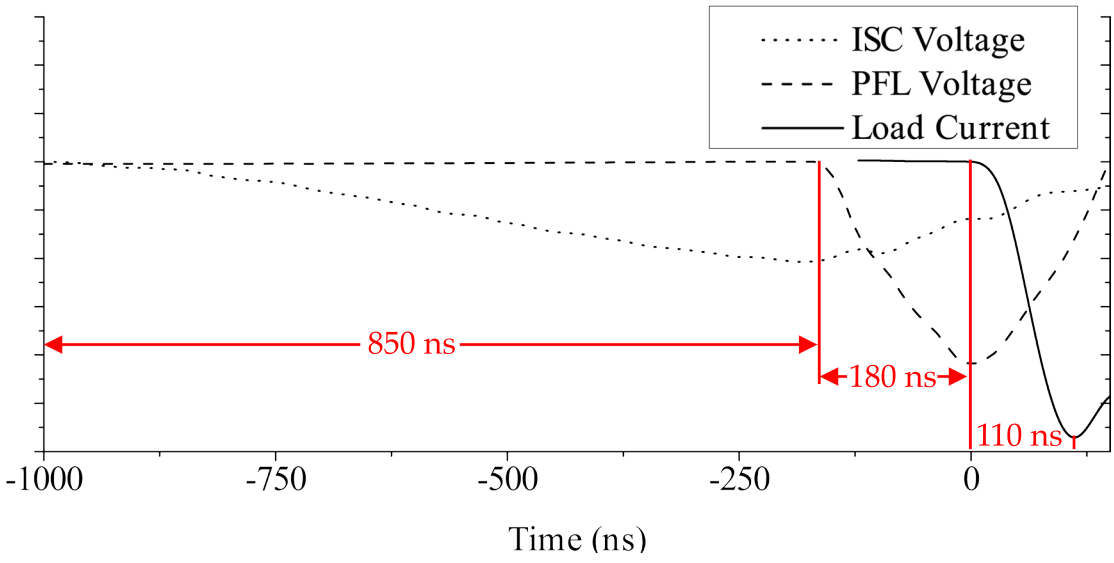

Figure 2.1: Voltage and current traces from COBRA showing pulse compression from the intermediate storage capacitor (ISC) to the pulse forming lines (PFL) and finally to the load.

2.2 General Description

The COrnell Beam Research Accelerator (COBRA) started its life out as a light ion-beam research accelerator (hence, the name). In 2003 and 2004, it was redesigned and rebuilt to fire Z-pinch loads, but the name stayed. COBRA is able to deliver 1 MA peak current into Z-pinch loads with a variable 100-250 ns rise time. The machine (see Fig. 2.2) has two Marx generators, each of which stores 55 kJ of electrical energy. Each Marx bank discharges into a parallel-plate water capacitor (called the intermediate storage capacitor (ISC)). Each ISC then discharges into two pulse forming lines (PFLs) via a self-breaking spark-gap switch. The four total PFLs are independently switched (either triggered or self-breaking) into the vacuum region of the machine via spark-gap switches. This final stage is where the variable rise time of the machine can occur. If all four PFLs are switched out at the same time, a fast pulse, around 100 ns will occur.

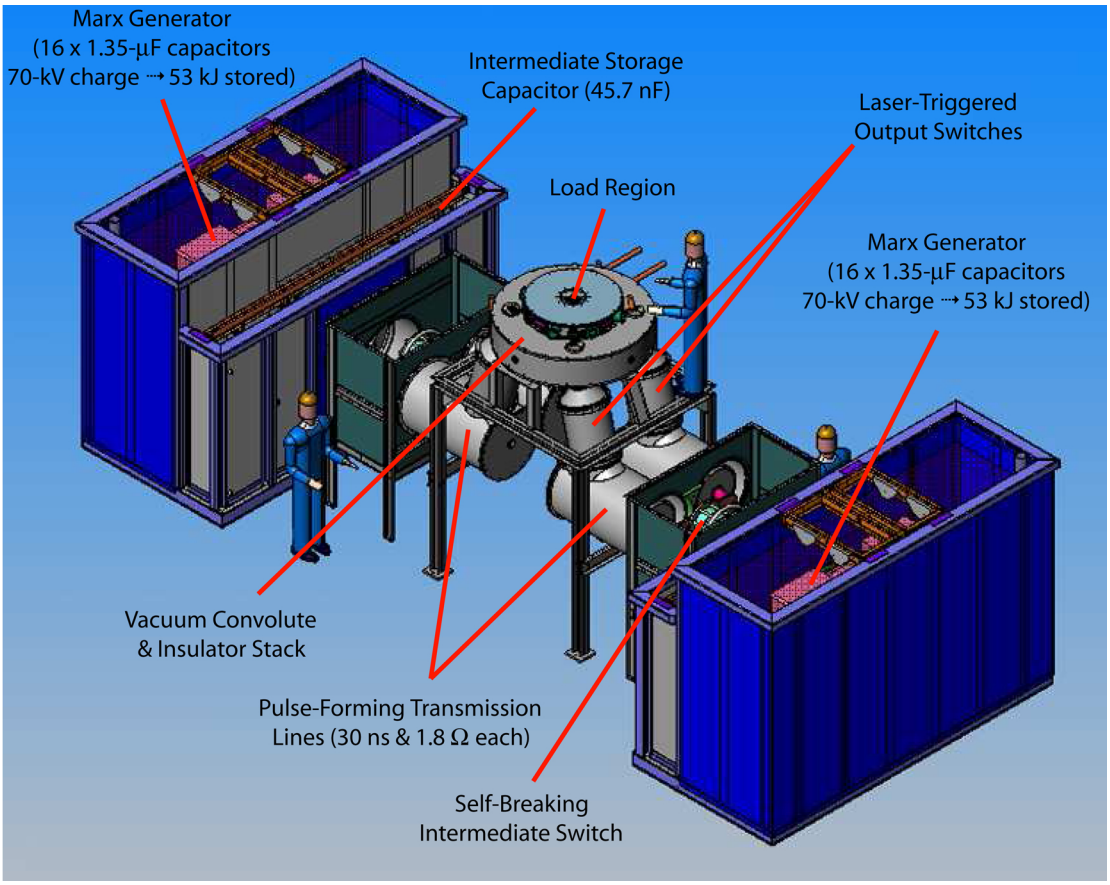

Figure 2.2: Drawing of COBRA showing scale and components.

If, however, they switch out at different times (by triggering them with a laser, using different switch pressures, or by circumstances beyond one's control), a longer pulse, up to about 250 ns can occur. See Fig. 2.1 for ISC and PFL voltage traces and current through the load. For more detailed information about COBRA's design and capabilities see Refs. [36, 37].

2.3 Diagnostics

The suite of diagnostics available for use on COBRA is quite extensive. What follows is a brief description of the more important ones for the research pre-

sented here.

2.3.1 Current Monitor

Because of the extremely high currents associated with pulsed power devices, a contact-free measurement of the current is usually performed.

The most basic device for making such a measurement is a B-dot probe. A B-dot probe is essentially just a loop of conductor that is placed in a region of magnetic field. The loop exploits Faraday's Law whereby the rate of change of the magnetic flux through the loop generates a voltage on the probe that can then be measured with an oscilloscope. The voltage at the scope therefore is proportional to the derivative of the magnetic field (hence the name B-dot or $\dot{B}$ probe) and by Ampere's law, is also proportional to the derivative of the current that produced the magnetic field. B-dot probes have some advantages and disadvantages. Advantages include their simplicity in design and construction in addition to their small size allowing them to be placed inside of wire-arrays, for instance. Their small size also has the benefit of reducing the inductance of the probe allowing them to have a very fast time-response. Also, their small size allows them to make local measurements (e.g. in the middle of a liner). Their main disadvantage is that their calibration is dependent on their distance away from the axis of current as well as their orientation to the magnetic field.

A Rogowski coil, named after Walter Rogowski[38], is in many ways just a lot of B-dot probes in series with each other to create a helical loop. The helical loop is placed around the current carrying conductor to be measured. Like the B-dot probe, it measures the derivative of the current (via the rate of change of

the magnetic flux through the loops), but it creates a signal that is N-times larger (N being the number of loops in the coil). If current is flowing in the $\hat{z}$-direction, the N loops are oriented to collect B_θ flux, but there is also one large loop created by the helix itself that would collect B_z flux. Therefore, in order to cancel out this signal, a conductor is usually looped back through the helix to cancel out the unwanted "B-dot" loop. See Fig. 2.3 for a simple drawing of how a Rogowski coil can be made out of a standard coaxial cable. As described, the coil is non-integrating, but can be made self-integrating by placing a small resistance in parallel at the output of the coil. The main advantage of a Rogowski coil is that their calibration is completely independent of their position or orientation, so long as the coil surrounds the conductor to be measured. The reason for this is because each of the individual loops is balanced by many other loops in generally opposite orientations and positions. For those who speak German, Rogowski and Steinhaus's original description can be found in Ref. [38].

Both B-dot loops and Rogowski coils are usually calibrated with the Cornell Coil Calibration Pulser (CCCP) against a Rogowski coil of known sensitivity (calibrated against a commercial probe). However, one can achieve surprisingly accurate calibration numbers by measuring the physical dimensions and calculating the theoretical values.

In practice on COBRA, B-dots are used to make dynamic measurements of current flow in a particular region of the plasma or other local magnetic field and a non-integrating Rogowski coil is used to measure the total current through the load. Additionally, B-dots are used to measure PFL and ISC currents.

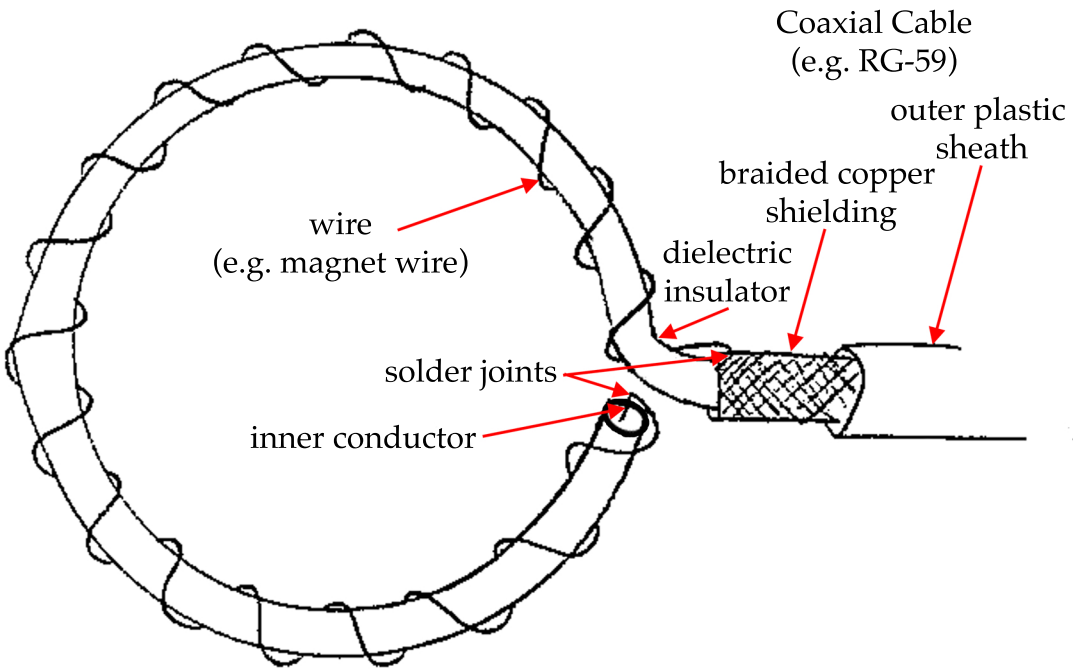

Figure 2.3: Drawing of Rogowski coil construction out of coaxial cable.

2.3.2 Silicon Diodes

Silicon (Si) diodes as described herein are photodetectors used in Z-pinch experiments primarily to detect x-rays, but in general they can be used to detect a much broader spectrum of light. A photodetector is similar to a regular semiconductor diode and is used in a reverse-biased configuration (typically about -50 V). When a photon of sufficient energy strikes the exposed Si substrate, it excites an electron, producing a photocurrent. Although the general spectral response of Si diodes are known, the sensitivity varies greatly over the 10 to 10,000 eV range where they are used. Therefore, they are not typically used as an absolute measure of x-ray flux.

2.3.3 Photoconducting Detectors (PCDs)

Diamond photoconducting detectors (PCDs) act very similar to Si diodes, but with a completely different mechanism and spectral characteristics[39, 40]. The conductance of the diamond substrate is linearly dependent on the incident photon flux to the surface. As x-rays are incident to the surface, the resistance of the diamond is decreased and more current flows through the detector. Therefore, by biasing the PCD at about -300 V, and measuring the voltage across a resistor in series with the detector, one can measure the photon flux. The main advantage of PCDs over Si diodes is they have a nearly linear spectral response up to about 5 keV. Therefore, they can be absolutely calibrated (in A/W) and used to measure x-ray flux. The two main disadvantages are their relatively high cost and that their sensitivity drops off sharply above 5 keV (depending on the thickness of the diamond). The reason for their high cost is not only due to the material cost (diamond), but also due to the complicated manufacturing process. In order to make electrical contact to the diamond, which is a good insulator, it first needs to be coated with a conductive layer. This contact is fairly robust, but makes repairing damaged contacts difficult. The spectral response is typically not a problem because most radiation of interest to our experiments is below 5 keV and it can even be accounted for as a sort of high-pass filter.

Both Si diodes and PCDs are primarily used in this research as timing diagnostics to determine when the X pinch images were taken.

2.3.4 Point-Projection Radiography

Point-projection radiography is used in Z-pinch experiments to either qualitatively or quantitatively measure the ion density of the plasmas. Point-projection radiography relies on using a very small x-ray source, such that it can be considered a point source. With the point source assumption, it is relatively straightforward to see how point-projection works. The closer the object (typically a Z-pinch) is to the source and the farther the detector (film) is from the object, the larger the magnification. This system has the significant advantage that no focusing elements are required. While focusing elements can be extremely beneficial with visible light techniques, x-ray focusing elements are generally very cumbersome, expensive, and have lower resolution than can be achieved without them. As the x-rays pass through the object to be imaged, they are absorbed and their intensity is attenuated proportional to the density, thickness, and material of the object. See Fig. 2.4 for a schematic overview of point-projection radiography and a sample image from [41].

On COBRA, X pinches are used to create the x-ray source[42], but it is possible to use a laser produced plasma as the x-ray source as well[43]. In its simplest form, an X pinch is two wires crossed at a single point and driven with a high current[44]. Recalling the Bennett pinch equilibrium (Equation 1.5), one can see that the magnetic pressure at the cross point will be four times larger (for a two-wire X pinch) than along one of the "legs" and thus, a pinching will occur at the cross point prior to any pinching along the legs. At this pinch point, a very small (a few microns) and short-lived (<150 ps) x-ray source is created[45]. These characteristics allow it to be considered an instantaneous point source, suitable for taking a "snapshot" of the very quickly changing plasma conditions

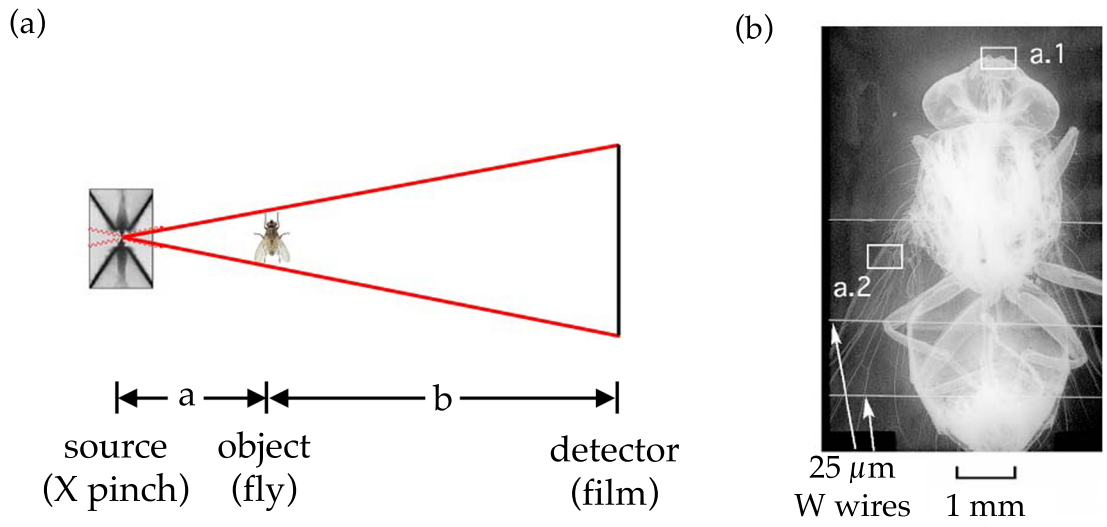

Figure 2.4: (a) Simple layout of point-projection radiography. (Not shown: x-ray filter) (b) Sample radiograph of housefly, used as cover art for Nature Review Genetics; September 2006.

in a Z-pinch. In practice, the X pinches used for point-projection radiography are often multiwire[42], nested[46], or hybrid X pinches[47], but the basic rules and characteristics still apply.

Because the detector is film, this diagnostic is time-integrated. "Snapshots" can still be created, however, because the sub-nanosecond X pinch radiation acts like a flash on a camera. But as many photographers have probably discovered, a flash won't work very well if there is another very bright light nearby (for instance the setting sun). Just like the sun can wash out the image from a camera, so too can the radiation from a Z-pinch wash out the exposure from the X pinch. For this reason, one of a number of methods is used to overcome this problem. Two methods involve inhibiting the radiation from the Z-pinch: overmassing the pinch so it does not radiate[42] or putting a monofilament material (fishing line) on axis to quench the radiation[48]. Another method involves observing only the regions of the plasma were strong radiation doesn't occur and

using heavily absorbing obstacles to block radiation from the strongly radiating regions[49]. Finally, one can use monochromatic imaging that involves finding a very narrow spectral range where the total fluence of radiation from point source is greater than that from the Z-pinch[50, 51, 43].

Although all methods of overcoming the Z-pinch radiation have been used on COBRA, the method employed in this research is over-massing. Recall again, the Pi parameter (Equation 1.1) that states for a given machine pulse, there exists an optimum mass that will maximize the kinetic energy of the implosion, which makes $\Pi = 4$. To get an earlier implosion, one can decrease the mass, which increases Π. To get a later implosion (or no implosion at all), one can increase the mass of the load, which decreases Π. Any load that results in $\Pi \lesssim 1$ will generally not implode. For these experiments, loads generally had a Pi parameter around 0.1.

The radiation from an X pinch that has the best spatial and temporal characteristics is continuum, but X pinches also produce intense line radiation. This radiation comes from a much larger region (1-2 mm) and lasts for several nanoseconds, which can ruin a radiograph by blurring the image. To deal with this problem, x-ray filtering is used. Essentially, one needs to find an X pinch material and filter material combination that provides crisp imaging. Luckily, this has already been investigated (primarily by Sergei Pikuz and Tania Shelkovenko[52]) and a combination that works very well is a molybdenum (Mo) X pinch with a 12.5 μm titanium (Ti) filter (see Fig.2.5). The strong line radiation (neon-like Mo) from the Mo X pinch are most intense from 2.5 to 2.75 keV, just below where the Ti filter starts transmitting x-rays in appreciable amounts (around 3 keV). Also, the Mo X pinch doesn't emit much continuum radiation above 6 keV where

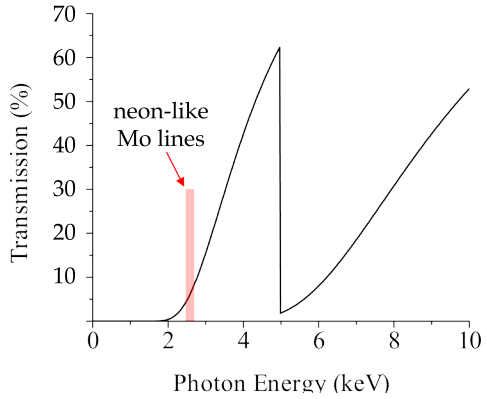

Figure 2.5: X-ray transmission vs. x-ray energy through 12.5 μm Ti filter showing neon-like Mo lines are significantly attenuated.

Figure 2.6: Illustration of diffraction-limited spatial resolution.

the Ti filter starts passing x-rays again. Therefore, with this X pinch and filter combination, it is common to say it uses 3-5 keV continuum radiation.

The spatial resolution of a point-projection x-ray image is determined by two effects: diffraction and geometry. The diffraction limited resolution, δx_d, is given by:

$$\delta x_d = \sqrt{\frac{\lambda ab}{a+b}} \quad (\mu m) \tag{2.1}$$

where λ is the wavelength of radiation in angstroms (Å), a is the distance from source to object in centimeters, and b is the distance from object to detector in centimeters (see Fig. 2.6 for illustration). In Fig. 2.6, by setting the path length difference between following the hypotenuse path and the straight path equal to $\lambda/2$, one can solve for δx_d to get Eq. 2.1. For the setup typically used in this

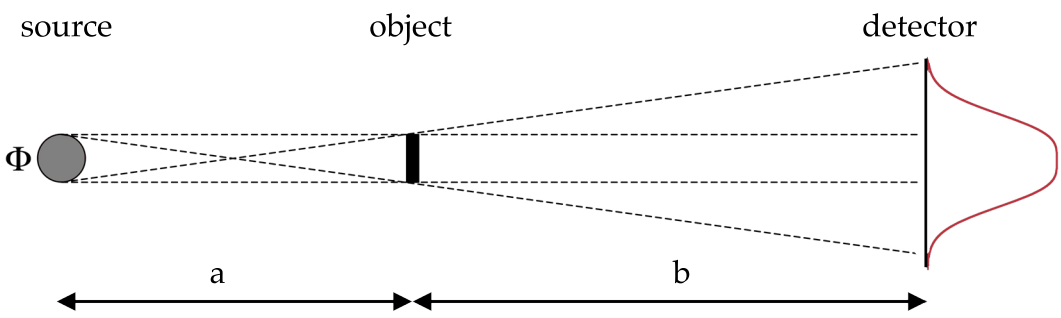

Figure 2.7: Illustration of geometry-limited spatial resolution.

research, the wavelength of incident radiation (using the 5 keV peak of the Ti transmission window) was 2.5 Å, the distance from the source to the center of the object was 5.6 cm, and the distance from the top of the Z pinch to the film was 34.7 cm. This lead to a diffraction limited spatial resolution of about 3.5 μm. Geometric spatial resolution, δx_g, is given by:

$$\delta x_g = \Phi \frac{b}{a+b} \quad (\mu m) \tag{2.2}$$

where Φ is the source size in μm, and a and b are the same as above and shown in Fig. 2.7. The distributed source leads to a blurring of the object at the detector. The source size of the X pinches used in this research have been previously measured to be 3 μm[46], which would result in a geoemetric resolution of about 2.6 μm. Therefore, as is the case with most X pinch radiography, the limiting factor in resolution is due to diffraction effects. The temporal resolution is determined by the duration of the X pinch radiation burst, which can be less than 150 ps and is usually assumed to be less than 1 ns because of limitations in measuring such fast pulses.

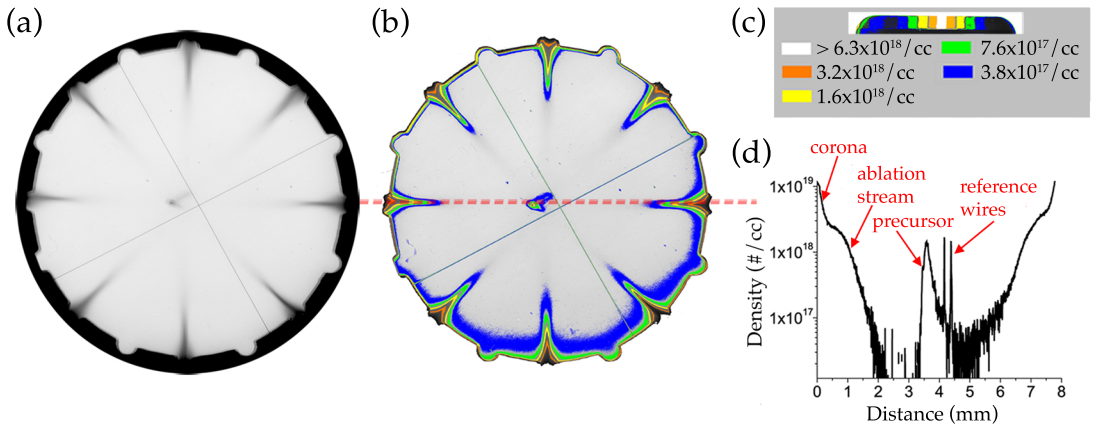

Figure 2.8: Stepwedge calibration showing (a) original grayscale image, (b) false colored calibrated image, (c) stepwedges and density key, and (d) calibrated density along the lineout indicated by the red dashed line.

The final topic of discussion for point-projection radiography is quantitative measurements, or calibration of the x-ray absorption. The way this is typically done for continuum radiation is to use a set of stepwedge filters in addition to the standard x-ray filtering on an otherwise unattenuated region of film[53, 48]. The stepwedge material should be made of the same material as the object to be imaged and there should be several steps (4 or 5 is sufficient but more is better) within the no-absorption to no-transmission range. Because both lines of sight (through the object and through the stepwedges) have the same main filtering, its contribution can be cancelled out. This leaves only the absorption of the stepwedges compared to only the absorption of the object (in this case, a Z-pinch). By developing both pieces or regions of film identically, it is possible to measure the exposure of each step and interpolate between them to provide a mapping of exposure to areal density. Therefore, if you know the thickness of the region of interest for the Z-pinch, you can determine the average volume density of that region. For an example of stepwedge calibration, see Fig. 2.8 and for more details, see Ref. [53].

One thing to be aware of is the temperature dependance of opacity for the material. Any material, if heated enough, will have significant opacity changes due to ionization, it is just a matter of to what degree the material is heated (pun intended). For typical Z-pinch temperatures, high Z materials (like tungsten (W)) have very little temperature dependance whereas low Z materials (like aluminum (Al)) have a significant temperature dependance on their opacities. Therefore, W is a suitable material for stepwedge calibration, because the cold stepwedges will have the same opacity as the relatively hot plasma. Aluminum, however is a poor candidate for stepwedge calibration. A material like copper (Cu), which was used in this research is somewhere in between. For high-Z materials, opacity versus temperature data is often times classified, so finding accurate information is difficult. For low- to mid-Z materials, PrismSPECT[54] software can be used to calculate x-ray transmission versus photon energy for various plasmas. Figure 2.9 shows x-ray transmission versus photon energy for carbon, aluminum, and copper at room temperature and 10 eV calculated using PrismSPECT. The parameters for the simulation consisted of a planar slab of 1 cm width, 10^{19} cm^{-3} ion density, LTE, .025 eV for room temperature and 10 eV for the hot case. One can see that for carbon, there are significant opacity differences in the 100 – 350 eV range. For aluminum, there are significant differences below 100 eV and near 1500 eV. For copper, only small differences appear in the very low energy region and near 1000 eV. For all materials, as the photon energy increases, opacity is dominated by the material density and the temperature differences become irrelevant.

Axial (end-on) X pinch point-projection radiography is used in this research to determine the ablation characteristics and precursor formation of Cu wire-arrays and liners. See Chapter 5 and 6 for more information.

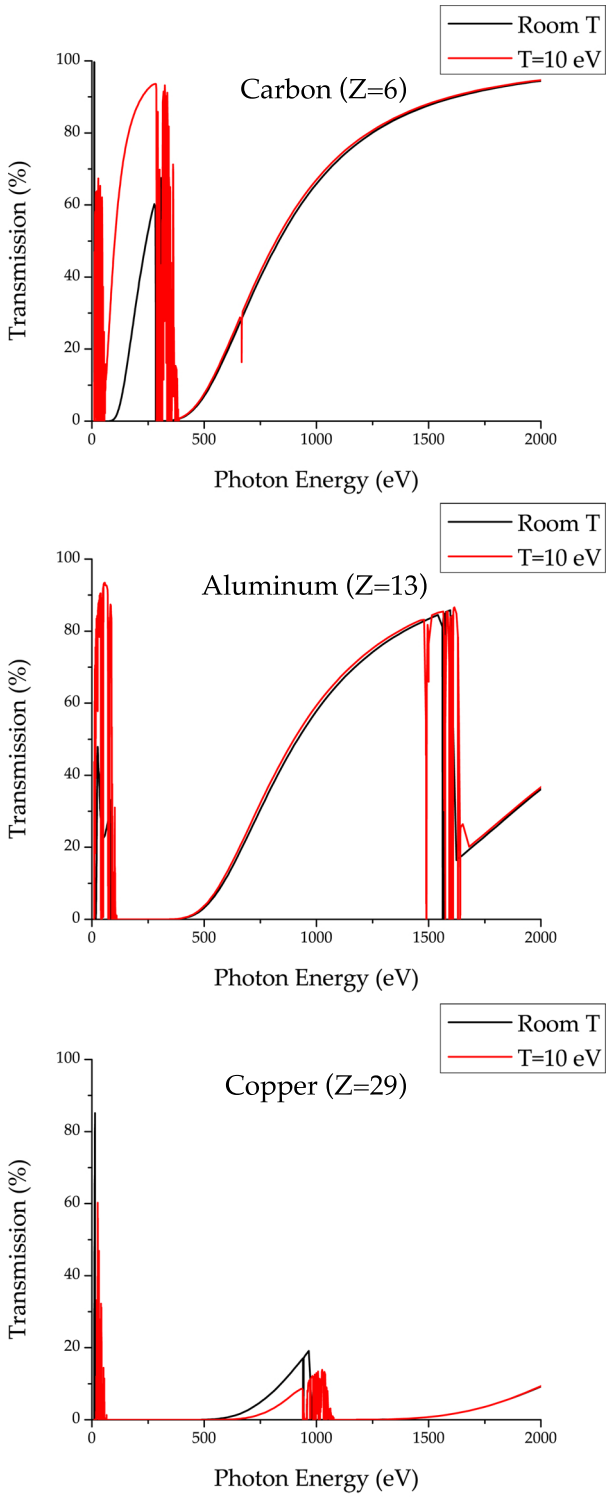

Figure 2.9: X-ray transmission versus photon energy for carbon, aluminum, and copper; comparing room temperature (black) and 10 eV (red) transmission profiles.

2.3.5 Laser Shadowgraphy

Laser shadowgraphy is a convenient way to get a quick, qualitative view of what is happening with the plasma. On COBRA, a green (frequency doubled Nd:YAG, 532 nm) laser that produces 150 ps pulses is used. The beam is split twice, to provide three separate beams for imaging. The beams are delayed with respect to one another such that there are 10 ns between each image. The images are recorded on standard digital cameras.

While it is possible to get quantitative density information from laser imagery (through interferometry or schlieren techniques), it is often used simply as just a shadow imager, creating "black and white" (actually black and green) two-tone images. The cutoff density for 532 nm wavelength is 3.9×10^{21} electrons/cm^3, which is somewhat regularly achieved in the densest regions of Z-pinches, but most of the shadow is actually created by light that is refracted out of the image by strong density gradients. See Fig. 2.10 for some examples of laser shadowgraphy.

Laser shadowgraphy is used in these experiments to measure the wavelength and amplitude growth of the axial instability on the outside of wire-arrays and thin foil liners.

2.3.6 Time-Gated Microchannel Plate (MCP) Camera

A time-gated Microchannel Plate (MCP) camera is used on COBRA, coupled with an array of pinholes (one pinhole per frame) and a digital camera. Each MCP produces a sequence of four self-emission pinhole images in the XUV (>1

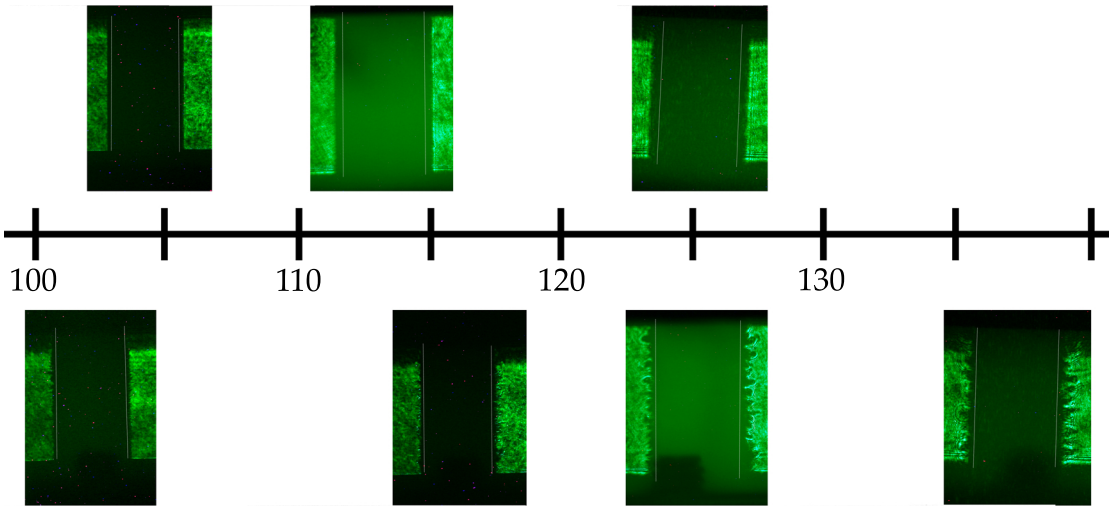

Figure 2.10: Sample of laser shadowgraphy showing a sequence of images (from multiple shots). Top images are from wire-arrays, bottom images are from foil liners, and time is in ns after current start.

keV) spectrum with the interframe time arbitrarily set to 10 ns and the exposure time set to 3 or 5 ns.

When XUV light is incident on the (XUV sensitive) MCP front surface, electrons are kicked off the surface and sent down an individual microchannel that acts much like a photomultiplier tube during its time-gated exposure. Each electron strikes the microchannel wall, producing multiple more electrons that, in turn, strike the wall further down. These electrons eventually strike a phosphor screen where they are converted back to light and recorded on a digital camera (See Fig. 2.11 for a sample MCP image). When one of the four independently triggered channels of the MCP is not active, the electrons that are produced at the front surface are not accelerated into the microchannels and therefore do not contribute to the exposure on the camera.

For this research, time-gated MCP pinhole images are used to determine initiation characteristics of various thickness thin foil liners.

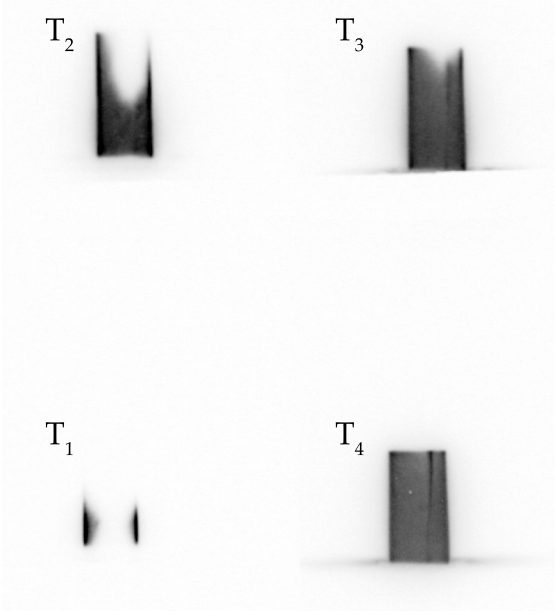

Figure 2.11: Sample of a sequence of MCP XUV pinhole images from a single shot. First frame is in lower left, following clockwise. 10 ns separate frames. Image has been converted from color and inverted so that the dark regions correspond to more exposure.

2.3.7 Optical Streak Camera

The optical streak camera on COBRA is typically used to continuously measure the visible light output of a Z-pinch along one or two slits. Similar to the MCP camera, when light is incident on the input of the streak camera, electrons are kicked off and accelerated towards a phosphor screen where they are converted back to light and recorded digitally. However, unlike the MCP camera where the acceleration is merely on or off, with the streak camera, an additional electric field, orthogonal to the electrons' travel, is ramped up in order to "streak" the electrons in one direction. Therefore, what you end up with is a two dimensional image, with one dimension being space (the slit that is focused onto the Z-pinch) and the other being time (variable from < 1 ns up to a few μs, but

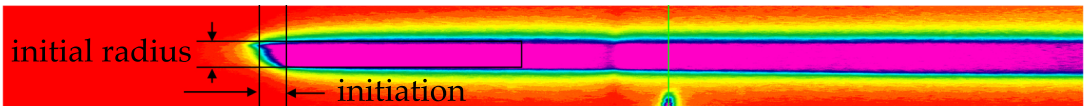

Figure 2.12: Sample of a false-colored optical streak across the diameter of a foil liner showing there is a significant time delay between the first optical emission and the entire radius lighting up. Streak window is 200 ns.

typically 200 ns). See Fig. 2.12 for a sample streak image.

The optical streak camera is used in this research to determine the radial light distribution as a function of time during the initiation stage of various thickness thin foil liners.

CHAPTER 3

WIRE-ARRAY AND THIN FOIL Z-PINCHES

3.1 Implosion Process

The implosion process of a Z-pinch can be separated into four fairly distinct stages: initiation, ablation, implosion, and stagnation (see Fig. 3.1). In the following sections, I will describe these stages for a wire-array and afterward, describe what differences exist for solid liners.

3.1.1 Initiation

The initiation stage occurs between the start of current flow to the formation of plasma around the wires. The formation of this "coronal plasma" around the wires can be observed with either light emission from the plasma or more typically (on COBRA) by analyzing the load voltage. When current starts to flow through the wires, they ohmically heat and expand and become more resistive, which leads to more heating. This process continues until plasma forms around the wires, at which point the resistance becomes negligible as the current flows through the plasma.

The voltage signal has three components:

$$V = RI + L\frac{dI}{dt} + I\frac{dL}{dt} \tag{3.1}$$

where V is the load voltage, R is the load resistance, I is the load current, and L is the load inductance. Early in time, before the wires begin to expand, the

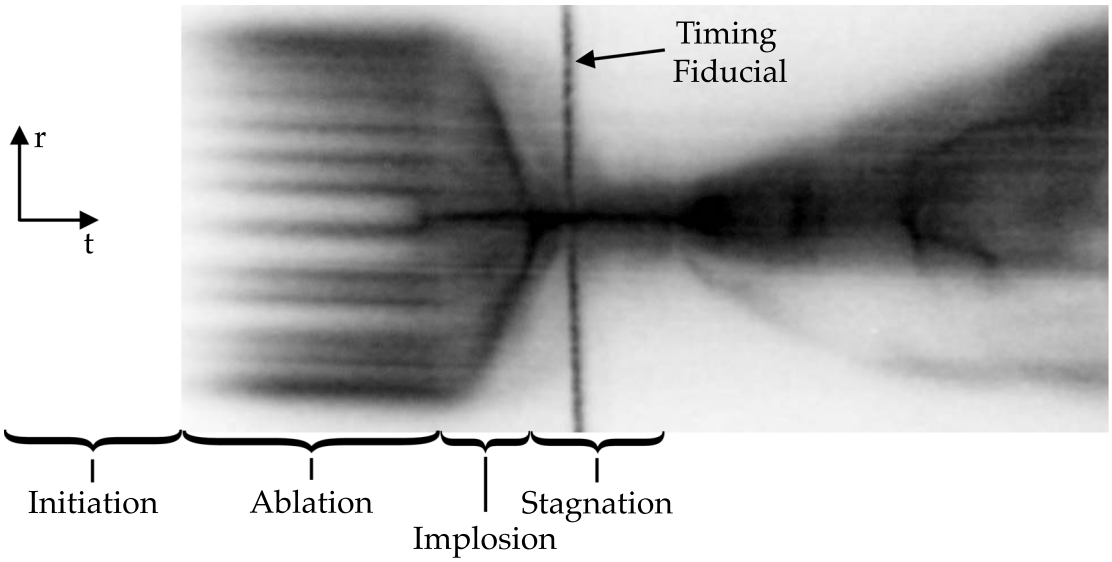

Figure 3.1: Optical streak across the diameter of an imploding 16-wire array showing initiation, ablation, implosion, and stagnation. The entire width of the streak is 200 ns.

inductance of the load is roughly constant, so the third term can be neglected and L can be replaced by L_0 which can be calculated or measured. Additionally, $\frac{dI}{dt}$ is directly measured with a Rogowski coil, so Equation 3.1 can be rearranged as:

$$V - L_0 \frac{dI}{dt} = RI \tag{3.2}$$

When plotted (see Fig. 3.2), Equation 3.2 will slowly rise, as both R and I increase, until plasma forms and the resistance drops to zero, at which point the signal will also abruptly drop. This drop is known as voltage collapse, for obvious reasons, and marks the end of the initiation stage.

3.1.2 Ablation

Current through the coronal plasma heats and ablates material from the dense cores that remain from each wire. This ablation is roughly uniform around each

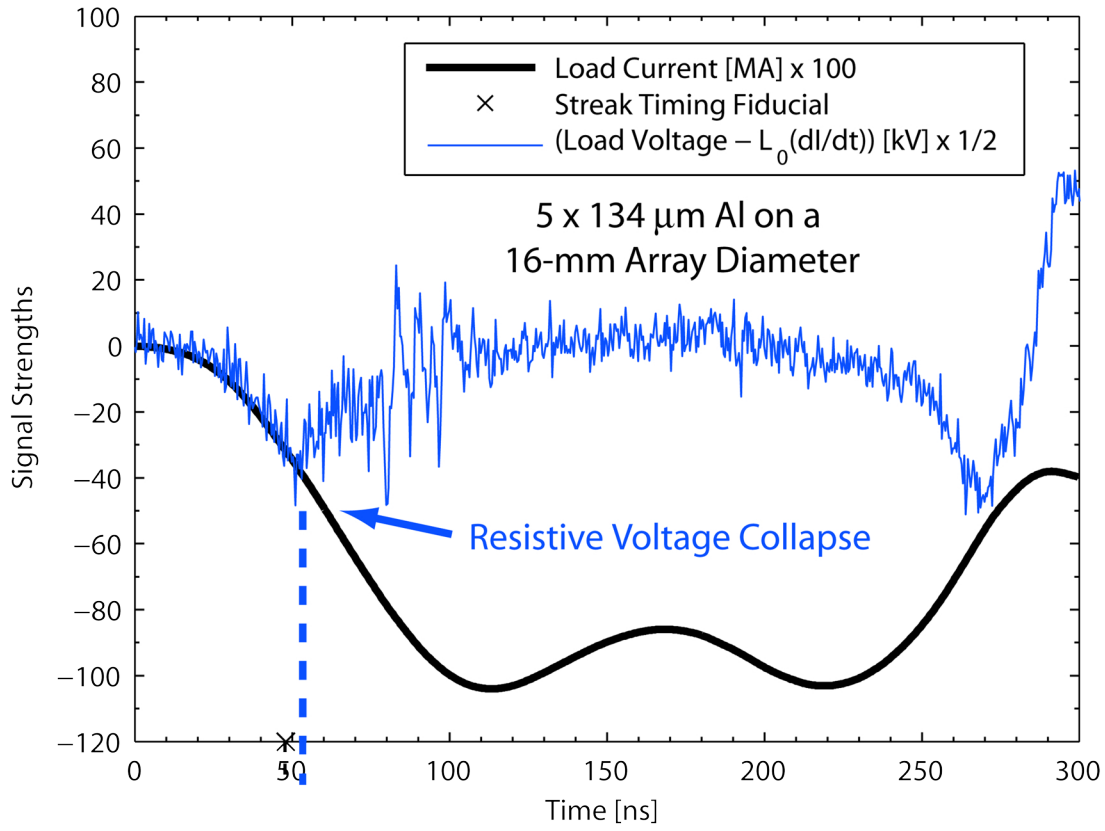

Figure 3.2: Plot of load current and resistive voltage from R.D. McBride's thesis showing voltage collapse occurring around 55 ns after the start of current.

wire, but is modulated along each wire. This "axial modulation" of the coronal plasma reaches a steady-state wavelength that is primarily material dependent, but also depends on wire-to-wire spacing and the change from local to global magnetic field configurations.

Once the magnetic field switches from being dominated by the local field to the global field, the ablated plasma, with current density $\mathbf{J}$, in the presence of magnetic field $\mathbf{B}$, is drawn toward the array axis by the global $\mathbf{J} \times \mathbf{B}$ Lorentz force. Material that is ablated from the inside of the wire is directly injected to the axis, while ablated material on the outside needs to be swept around the still remaining dense wire cores. The "ablation streams" accumulate on axis and

form a "precursor plasma," named as such because it arrives on axis prior to the implosion phase. The ablation stage continues until approximately 50% of the initial mass has been ablated, at which point gaps have formed along the wires and the implosion phase begins[55].

3.1.3 Implosion

By the time gaps have formed along the wires, the magnetic field has penetrated each of the wire cores and begins to act upon them directly. This leads to a rapid radial acceleration of the ~50% mass that remains in the initial wire position in the dense cores via the $\mathbf{J} \times \mathbf{B}$ force. Some "trailing mass" usually stays behind and does not participate in the later stagnation phase.

3.1.4 Stagnation

The implosion phase ends and the stagnation phase begins when the bulk of the mass reaches the axis and "stagnates" due to the streams' opposing momenta and the global $\mathbf{J} \times \mathbf{B}$ force still acting on the plasma. The significant kinetic energy of the implosion is then thermalized and converted to x-ray emission resulting in an intense x-ray burst at stagnation. In addition to the kinetic energy, the plasma on axis now carries a significant amount of current and experiences more $\mathbf{J} \times \mathbf{B}$ forces that cause heating and compression of the stagnated plasma. Eventually, the plasma becomes unstable and explodes outward as indicated at the end of Fig. 3.1.

3.2 Solid Liners

Significant differences exist in the initiation and ablation stages between solid liners and wire-array Z-pinches.

One significant difference between wire-arrays and solid liners is surface area: solid liners have a much greater surface area than just about any wire-array. Using examples from this research, the surface area of a sixteen wire, 75 μm wire diameter, 1 cm height array is 38 mm^2. The same amount of mass, distributed in a 4 mm diameter, 6 μm thick, 1 cm height solid liner has a surface area of 126 mm^2 using only the outside surface. That amounts to a factor of three difference, again using only the outside surface. Also, 75 μm wires are unusually large for most wire-arrays. If one were to use 10 μm wires and a 0.1 μm thick liner (again, that equates to the same mass), the difference in surface area would be a factor of 25 (using only the outside surface).

The reason surface area is important is because it equates to the surface where current will flow and it is inversely proportional to the inductance (and voltage). Having a lower voltage means initiation will happen later and having more surface area for the current to flow means forming plasma to shunt the current will be slower. With a slower and later initiation, it is more likely that nonuniformities will develop that could impact the later stages of the implosion.

The other main difference between wire-arays and solid liners is the obvious continuous versus discrete nature of the mass distribution. This has a significant impact during the ablation stage. As stated above, when wires ablate, they do so roughly uniformly around the cross-section of the wire and material that is ablated on the outside of the wire (with respect to the array axis) gets swept

around the wire (through the gaps between the wires) and toward the axis. For solid liners, depending on the skin depth, most of the current flows on the outside surface (path of least inductance) and therefore most of the ablation occurs on the outside surface. However, in contrast to wire-arrays, there are no "gaps between the wires" for the ablated plasma to get swept toward and make it to the axis. The ablated material just gets pushed back onto the outside surface where it builds up, which results in two things occurring. First, less material makes it to the axis to form a precursor plasma. Secondly, the buildup of plasma on the outside surface is somewhat similar to the axial instability in wire-arrays, but it never gets "shut off" like it does with wire-arrays because there is never a transition from local to global magnetic field; it just continues to grow and grow.

CHAPTER 4

INITIATION OF THIN FOIL LINERS

4.1 Motivation

Uniform initiation of a Z-pinch is extremely important. If plasma formation is not uniform during initiation, it can adversely affect the ablation, implosion, and stagnation of the pinch because asymmetries can seed instabilities.

In wire-arrays, uniform initiation is fairly simple to achieve. With the high voltages delivered in pulsed power drivers, and the relatively small surface area for plasma to form around the wires, one need only to achieve good electrical contact at the electrodes (particularly the cathode) to get uniform plasma formation. Making good electrical contact is usually done by forcing an individual wire against the electrodes by using weights on one or both ends. This gravity tensioning provides a sliding contact that allows for a vertical displacement of the electrodes which typically occurs when the load chamber is put under vacuum (on COBRA, the electrodes move about 100 μm closer to each other).

With solid liners, nearly everything that is "easy" about wire-arrays becomes difficult. The large surface area of the liners means more plasma needs to be created, which takes more time, and can lead to irregularities. The most common problem is filamentation, where arcs are formed on the liner surface that preferentially divert current along discrete paths. Making good electrical contact is not simple, either. Unlike wire-arrays, one cannot simply attach some weights and let the liner drape across the electrodes. What is typically done is to have one of the "contacts" actually just be a close fit (i.e. not actually making contact)

with the assumption that the gap will quickly be shunted by plasma. While this definitely does occur, it also introduces a source for nonuniform plasma initiation. For these experiments, the electrodes were designed to minimize any problems that could occur due to electrode contact.

In the 1980's, a set of plasma initiation experiments were performed during the SCORPIO campaign at Sandia National Laboratories. The SCORPIO data were classified Confidential at the time because they were thought to be too critical to release. However, with such a low classification level and because the experiments took place before the act of digitally cataloging everything was common practice, the research was not archived and was lost before restrictions were removed. This, unfortunately, means the information from these experiments is extremely scarce, even amongst those involved. Nevertheless, Pace VanDevender, former vice president at Sandia, has provided me with with what he has been able to pieced together from the SCOPIO campaign.

The SCORPIO experiments involved aluminum liners that were 1 cm in radius and 2 cm tall with a thickness of just 0.02 to 0.2 μm. Using schlieren photography, holography, and open shutter photography, it was found that the condition for uniform discharge (initiation) was

$$\frac{dJ}{dt} = 8 \times 10^{16} \quad \left(\frac{A}{cm^2 s}\right) \tag{4.1}$$

where $\frac{dJ}{dt}$ is the time derivative of the current density in the liner. Since that $\frac{dJ}{dt}$ is much higher than most present day liner experiments and because of the lack of documentation remaining from the original experiments, it was determined that it would be worthwhile to attempt to recreate some of the conditions of the experiment. By using modern drivers, diagnostics, and targets (liners), the goal of these initiation experiments was to determine if this result (Equation 4.1) is

confirmed, plausible, or busted.

4.2 Experimental Setup

The liners in these experiments were made of copper and were 4 mm in diameter and 1 cm in length. In order to test a range of dJ/dt values, the easiest parameter to change is the area through which the current flows (i.e. the thickness of the liner). Therefore, we had General Atomics make thirteen different liners for us with varying thickness (ranging from 0.6 to 23.5 μm) as shown in Table 4.1. In the table, the "Liner Designation" contains the following information: NT-S.LN; where NT is the nominal thickness, S is the shipment number from General Atomics, and LN is the liner number from General Atomics as given in the data sheets (see Appendix B).

Table 4.1: List of liner thicknesses for initiation experiments.

Liner Designation	Liner Thickness (μm)	COBRA Shot #
1-3.15	0.6	2151
1-3.09	1.6	2150
1-3.12	1.8	2149
3-2.04	2.5	2148
3-2.02	4.3	2147
3-2.06	4.3	2146
6-2.11	6.0	2144
6-2.12	6.9	2145
20-3.05	20.2	2143
20-3.13	20.5	2142
20-3.07	21.7	2141
20-3.01	23.0	2140
20-3.06	23.5	2139

The skin depth of a conductor is given by

$$\delta_{skin} = \sqrt{\frac{2\rho}{\mu\omega}} \tag{4.2}$$

where ρ and μ are the conductor's resistivity and absolute magnetic permeability, and ω is the angular frequency of the current driver. Using room temperature values for copper ($\rho = 1.68 \times 10^{-8}$ Ωm and $\mu = \mu_0$) and COBRA's 100 ns sine-squared pulse ($\omega = \pi \times 10^7$ s^{-1}), $\delta_{skin} = 29$ μm. This is a lower limit to the skin depth, because the copper becomes more resistive as it heats up. Therefore, all of the liners used in these experiments are thinner than the skin depth and current is distributed throughout the material.

The liners were manufactured at General Atomics by depositing a very thin layer of copper (<100 nm) on an acrylic mandrel and then electroplating the remainder of the thickness. This was a somewhat imprecise method, as indicated by the fact that the actual thickness was only sometimes within even 1 μm of the nominal thickness. However, they were able to measure, to within 0.1 μm the actual thickness. Once the liners were received at Cornell, the acrylic mandrel was typically removed by a leaching process (see Appendix C). It was determined experimentally (i.e. they broke) that liners thinner than about 3 μm would not be able to hold themselves together during the leaching process. Therefore, to remain consistent for this set of experiments, these liners remained on their acrylic mandrels. Because we were investigating the initiation stage, this was a reasonable compromise.

As mentioned earlier, electrical contact is of particular importance to initiation. Because the liners in this set of experiments remained on their acrylic mandrels they were very robust. Therefore, the liners were able to be put under tension by making the anode-cathode spacing ever-so-slightly longer than the

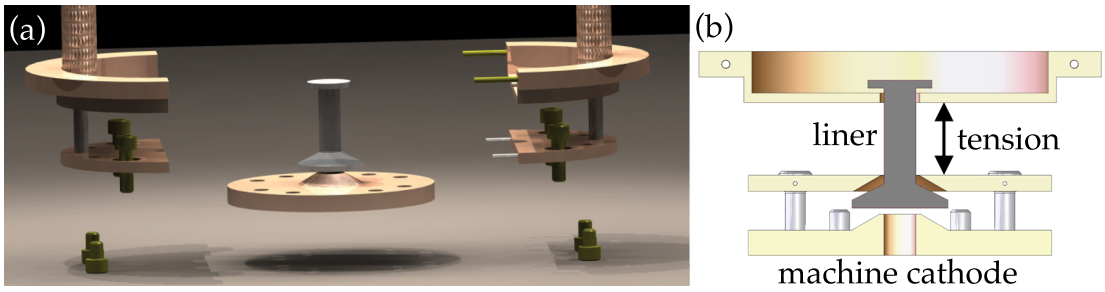

Figure 4.1: Renderings of liner hardware showing (a) an exploded view of how the hardware is assembled and (b) a cutaway of the assembled hardware showing how electrical contact is maximized between the liner in gray and the coupling hardware in brass.

1-cm length of the liners (see Fig. 4.1). In this way, the electrodes "dug in" to the liners a bit and made excellent electrical contact.

These experiments used the load current monitor (non-integrating Rogowski coil) to measure dI/dt (and to calculate dJ/dt by simply dividing the dI/dt by the cross-sectional area of the liner). Also, the visible streak camera and XUV MCP camera were used to determine the onset and duration of the initiation. The visible streak camera was set up with two horizontal slits (perpendicular to the direction of current); one approximately 2 mm above the cathode and one approximately 2 mm below the anode (see Fig. 4.2(a)). This allowed a continuous measure of the visible emission across the radius at two different axial positions. The horizontal slits were chosen because of the nature of the filamentary non-uniformities. A filament, at a specific azimuthal position, tends to remain stationary as the current slowly redistributes (albeit unevenly) across the azimuth. This is captured by the horizontal slit, with light starting at one point along the azimuth and spreading out to fill the entire width of the liner. The XUV pinhole cameras were set up at two different azimuthal positions to have orthogonal views to each other (see Fig 4.2(b)), with each camera capturing

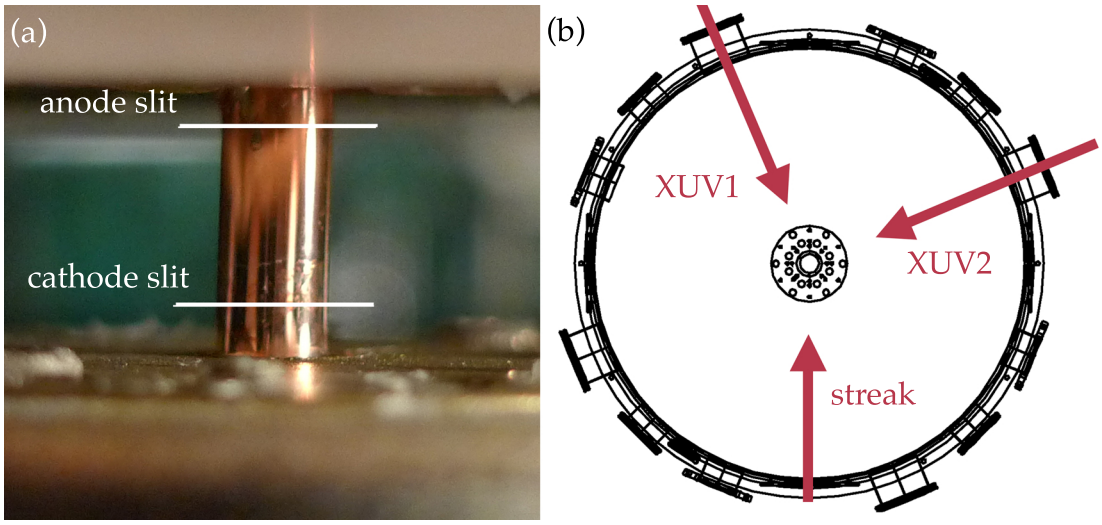

Figure 4.2: Diagnostic setup showing (a) a picture of liner in load hardware showing location and orientation of streak camera imaging slits and (b) an overview of the COBRA chamber showing the relative locations of the diagnostics with respect to the load at center.

4 images spaced 10 ns apart. These cameras allowed the axial and azimuthal uniformity to be determined, although only at discrete times.

An example of the data analysis is given in Figs. 4.3-5. In Fig. 4.3, the measured dJ/dt and current are plotted and time-synched with a false-colored visible streak image and two sets of XUV pinhole images. Synchronization is achieved with a timing fiducial on the streak image as well as monitor signals from the diagnostic laser (that creates the fiducial) and the XUV cameras. In Fig. 4.4, a zoomed in region of the false-colored visible streak image is shown. The primary metric that is extracted from this region is what is labeled as "delta". Delta is the time delay from the first light emitted from the liner surface to the time when the entire liner is lit up uniformly. The intensity threshold that was used in the false-colored images was dark blue. This was chosen because it reliably and consistently aligned with the original diameter of the liner. This

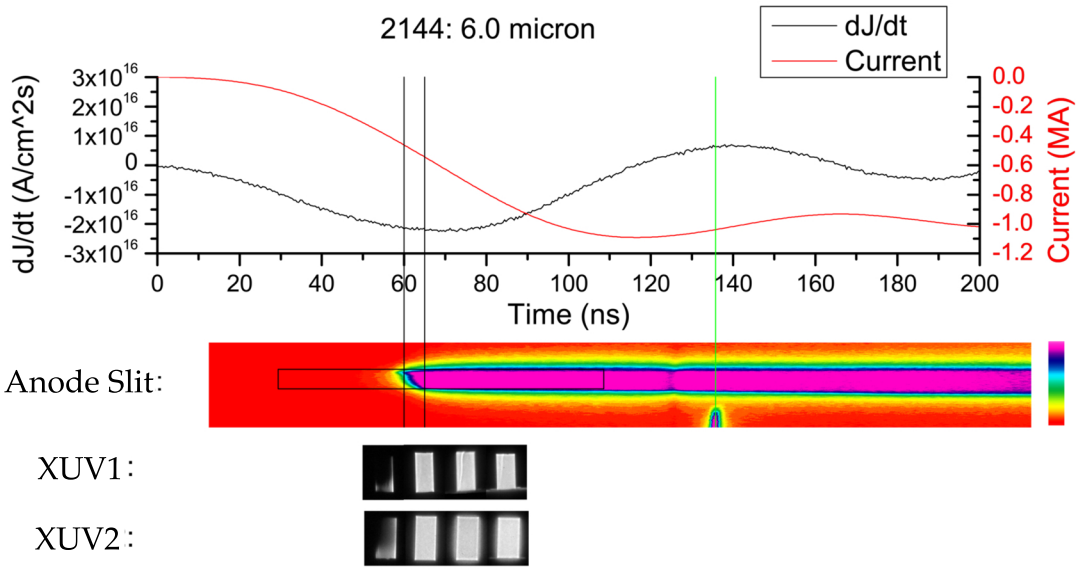

Figure 4.3: Example of data analysis showing correlated timing of current, dJ/dt, false-colored visible streak, and XUV pinhole images.

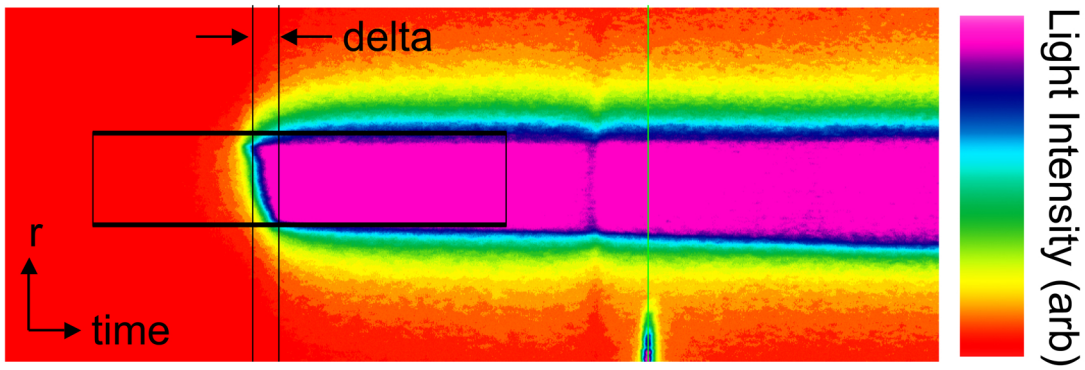

Figure 4.4: Example of data analysis showing "delta" - the time difference between first light and full illumination on a false-colored streak.

delta was then transferred back to the plot of dJ/dt, as shown in Fig. 4.5. The instantaneous dJ/dt at the time of first light was then recorded. This was done for every shot and a plot of delta vs. dJ/dt was then created (see Fig. 4.10 in the Results section).

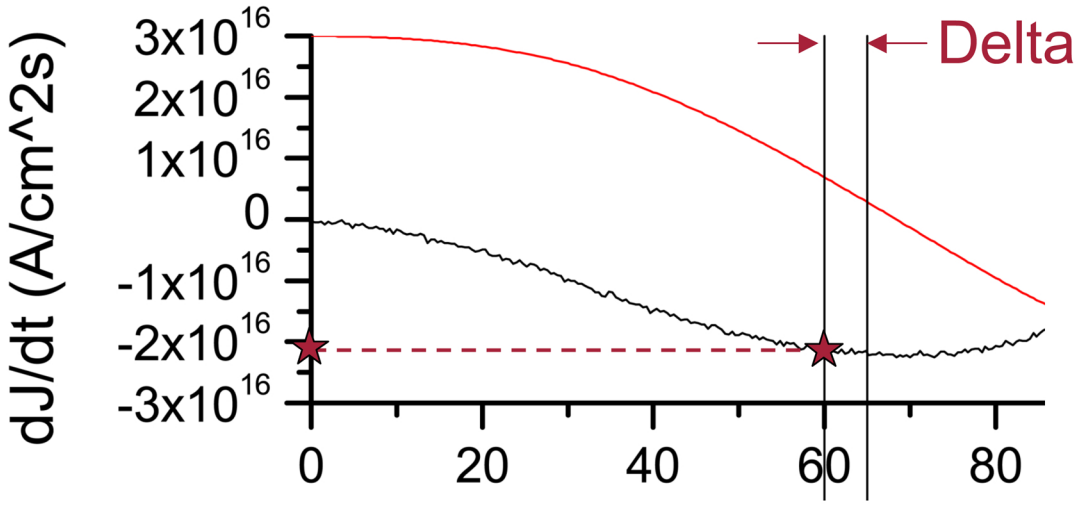

Figure 4.5: Example of data analysis showing "delta" being mapped back to dJ/dt plot, indicating the instantaneous dJ/dt at the time of first light. The red line is the current (scale not shown).

4.3 Results

The results were mostly as hypothesized; thin liners initiated quickly and thicker liners took more time to initiate. Presented here are data from representative examples of a thick, medium, and a thin liner.

Data from a thick (23.5 μm) liner is shown in Fig. 4.6. This liner did not begin to light up until very late in the pulse – around 110 ns. This is partially because it was a slower machine pulse, but mainly because of the large amount of mass that needed to be heated and initiated. From the visible streak image, the liner is shown to take almost 20 ns for the entire surface to be uniformly illuminated. This data is corroborated with the images from one of the XUV cameras. In the first frame, no light is recorded; in the second frame, it is partially and non-uniformly lit; and in the third frame, it is completely and uniformly illuminated. Given an inter-frame time of 10 ns, the XUV data is in good agreement with the

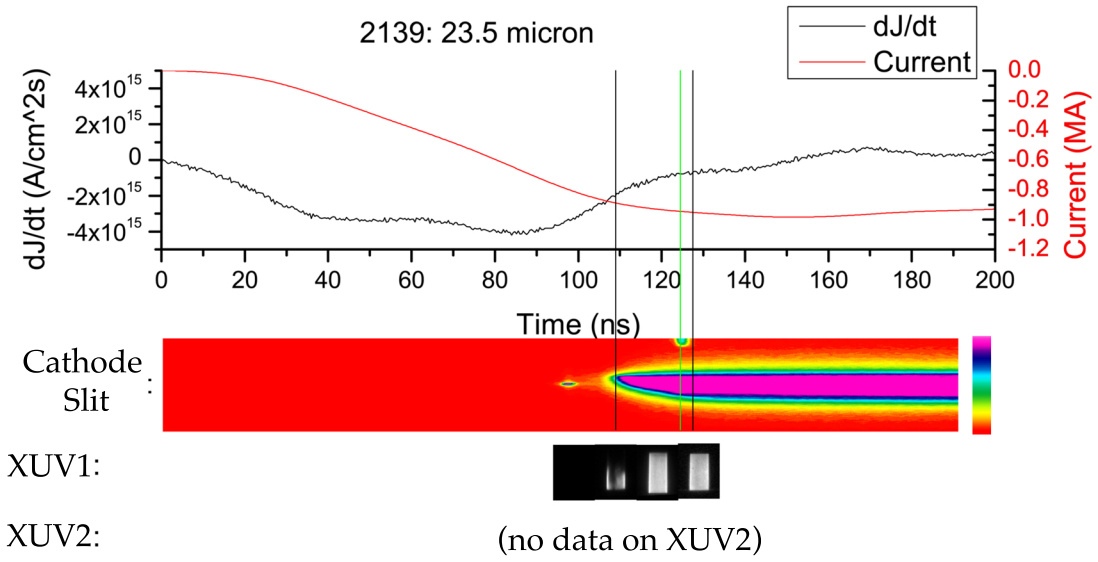

Figure 4.6: Sample data of a thick liner showing very slow initiation behavior.

visible streak data.

Data from a medium thickness (6.0 μm) liner is shown in Fig. 4.7. This liner lit up much sooner than the thick liner – around 60 ns compared to 110 ns. The visible streak shows that it also initiated much quicker; reaching uniform illumination in about 5 ns. Again, this is corroborated with the XUV images where it takes less than two frames to completely light up.

Finally, data from a thin (2.5 μm) liner is shown in Fig. 4.8. Following the trend from the previous data, this liner emits sooner and initiates quicker. Both the streak and the XUV images show that the liner initiated almost instantaneously – in about 1 ns.

In every case but one, the visible streak image and the XUV pinhole images were in good agreement with each other. The one, anomalous, shot was a thick (21.7 μm) liner shown in Fig. 4.9. Using the analysis outlined in the previous

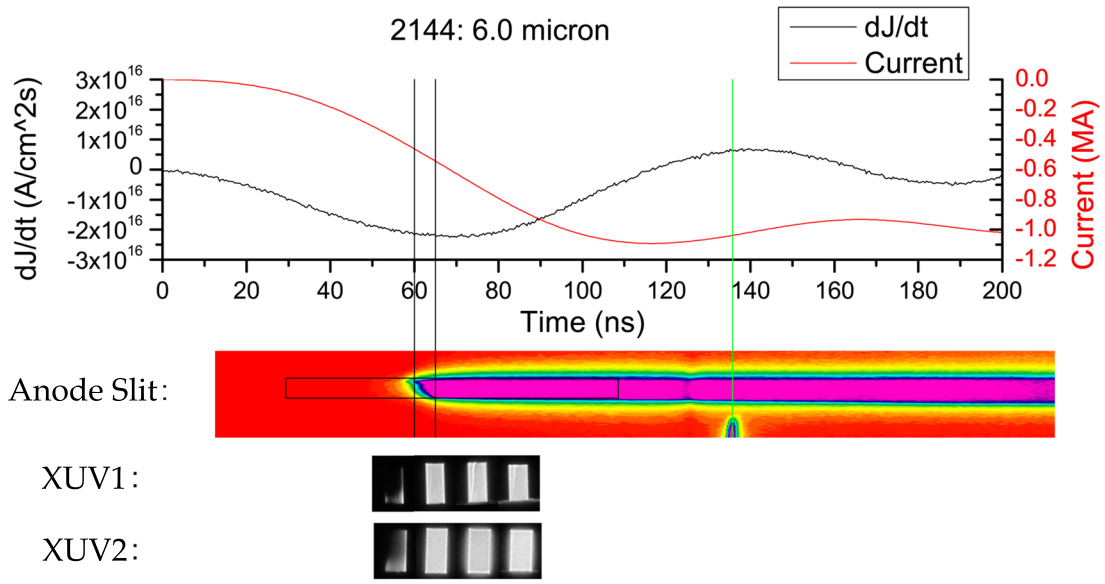

Figure 4.7: Sample data of a medium thickness liner showing fairly quick initiation behavior.

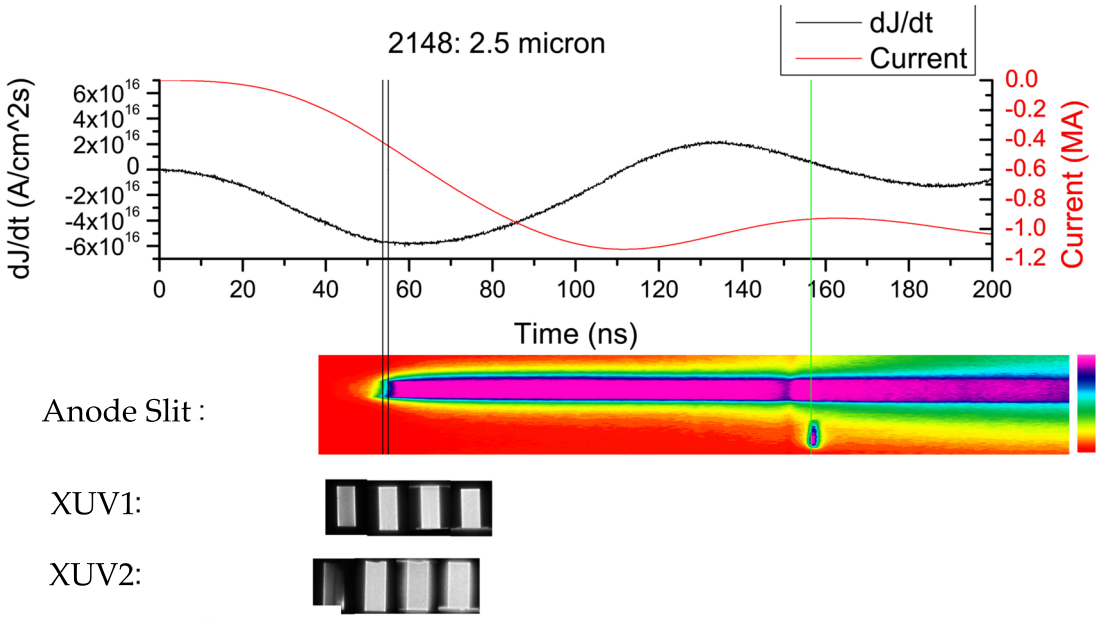

Figure 4.8: Sample data of a thin liner showing very quick initiation behavior.

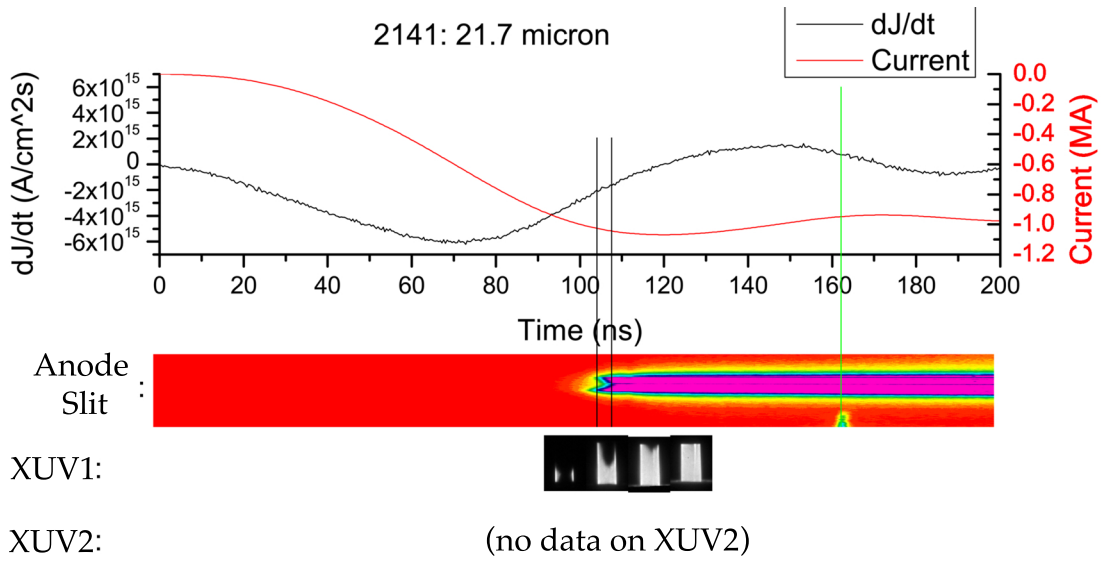

Figure 4.9: Sample data of an anomalous thick liner. Analysis of the streak image indicates a 4 ns initation, but analysis of the XUV images indicates about 20 ns initiation time.

section, a delta of only 4 ns is inferred. However, if the XUV images were used for analysis, one would see that it took about 3 frames (or 20 ns) to go from first light to full illumination. This shows that the analysis is not foolproof and in cases with extremely non-uniform initiation, the azimuthal location where the visible streak is being recorded can strongly influence the results.

The compiled data from every shot is shown as a plot of delta (in ns) vs. dJ/dt (in $Acm^{-2}s^{-1}$) in Fig. 4.10. Again, there is a clear trend shown. The thickest liners (lowest dJ/dt) take a long time to initiate. As the liners get thinner (dJ/dt gets higher), the initiation occurs quicker and quicker until the liners initiate nearly instantaneously. The threshold for instantaneous initiation was found to be a $dJ/dt > 3.5\times10^{16}$ $Acm^{-2}s^{-1}$. This is in good agreement, but slightly less than the $dJ/dt > 8 \times 10^{16}$ $Acm^{-2}s^{-1}$ from the SCORPIO experiments[56]. While the differences in the experimental setup from the SCORPIO experiments to these experiments are multifarious, both sets of data show that increasing dJ/dt in

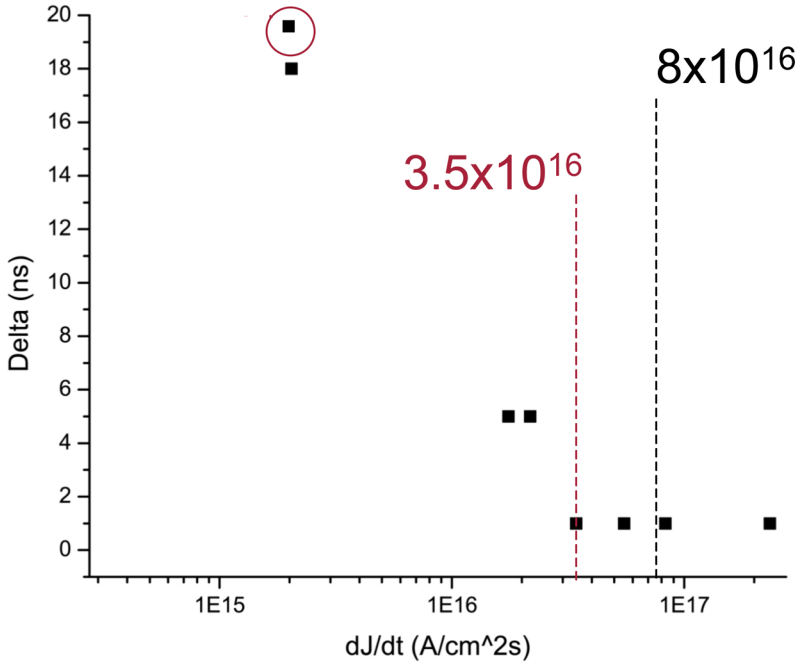

Figure 4.10: Compiled data from initiation experiments showing Delta vs. dJ/dt. One anomalous data point (circled) was analyzed differently from the rest. A threshold of $dJ/dt > 3.5 \times 10^{16}$ $Acm^{-2}s^{-1}$ was found which is in good agreement with the SCORPIO data.

the liner improves initiation.

4.4 Discussion

While a correlation between dJ/dt and the duration of initiation exists, at least three other possibilities have been proposed. The 2010 paper by Awe *et al.* have proposed that initiation will occur (in solid Aluminum rods) when the magnetic field at the surface reaches 2.2 MG (220 T)[57]. The 2009 paper by Chaikovsky *et al.* have proposed that the initiation time can be predicted using an action integral[58]. Lastly, J.C. Martin's textbook *J.C. Martin On Pulsed Power* has a

study of electrical breakdown in multichannel gaps that suggests a correlation between breakdown uniformity and electric field strength[59].

In Awe's 2010 paper titled "Threshold for Thermal Ionization of an Aluminum Surface by Pulsed Megagauss Magnetic Field," it is proposed that a necessary condition for plasma formation on the surface of 6061-alloy Aluminum (Al) rods is to reach a magnetic field strength of 220 T[57]. The study used Al rods with initial diameters ranging from 0.5 to 2.0 mm being driven by the Zebra Z-pinch driver at 1.0 MA with a rise time of 100 ns (same as COBRA). For the 2.0 mm rods, the magnetic field threshold was not reached and no plasma was formed (only resistive metal vapor). In this study, great care was taken to ensure plasma was produced by thermal mechanisms (e.g., ohmic heating, pdV work, thermal conduction, and radiation diffusion), instead of nonthermally (e.g., by electric-field-driven electron avalanche or arcing electrical contacts). This was largely achieved by very specialized load hardware that achieved excellent current contact far away from the region of interest.

Applying the Awe threshold to my thin foil liner experiments, one would realize that due to the larger radius of my loads, 220 tesla is never reached at the liner surface (see Fig. 4.11). In fact, the highest fields reached were around 100 T and those produced the worst initiation characteristics. The cause for this discrepancy is most likely due to the fact that it was more difficult to mitigate nonthermal mechanisms with the liner designs on COBRA.

In Chaikovsky's 2009 paper titled "Electrical Explosion of Metals in Fast-Rising Megagauss Magnetic Fields," it is proposed that the action integral determines at what time plasma formation occurs[58]. For uniformly (or quasiuniformly) distributed current throughout the conductor cross section, the specific

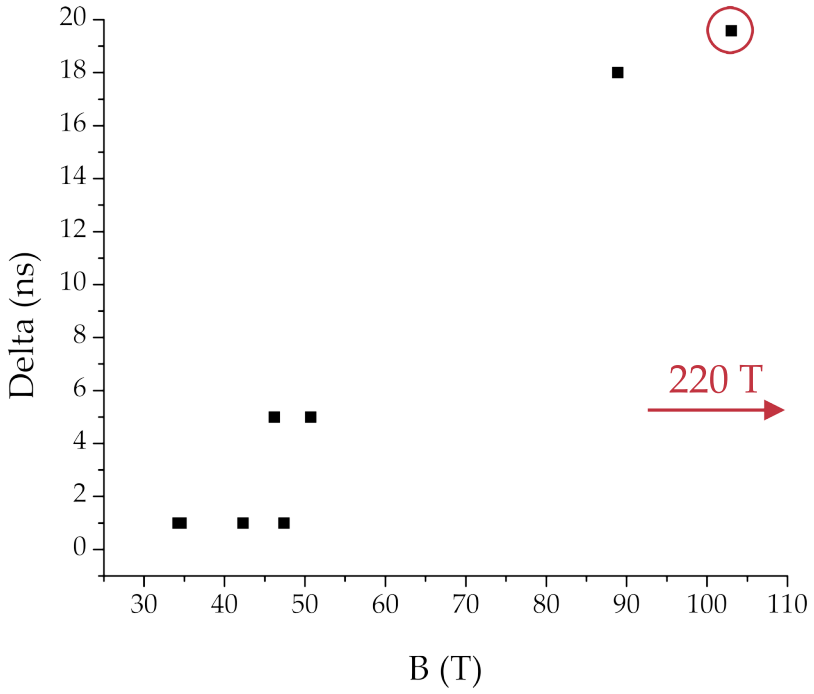

Figure 4.11: Compiled data from initiation experiments showing Delta vs. B, the magnetic field strength at the liner surface at the time of initiation. One anomalous data point (circled) was analyzed differently from the rest. The Awe threshold of 220 T is never reached. The best initiation results actually occurred with the smallest magnetic fields.

action integral is defined as

$$h = \int_0^{t_{ex}} j^2 \, \mathrm{d}t = \int_{\varepsilon_0}^{\varepsilon_w} \sigma \, \mathrm{d}\varepsilon_w \tag{4.3}$$

where h is the specific action integral, t_{ex} is the time of explosion, j is the uniformly distributed current density, ε_w is the energy density delivered to the conductor, and σ is the specific conductivity of the conductor. In copper foils of 2 mm diameter and a thickness of 20 μm fired on the MIG generator (current rise time of 100 ns with an amplitude of 3 MA), the explosion (initiation) occurred at current densities of $(7.5 \pm 0.5) \times 10^8$ A/cm^2, and the specific action integral was estimated to be $(5 \pm 1) \times 10^9$ A^{2}s/cm^4.

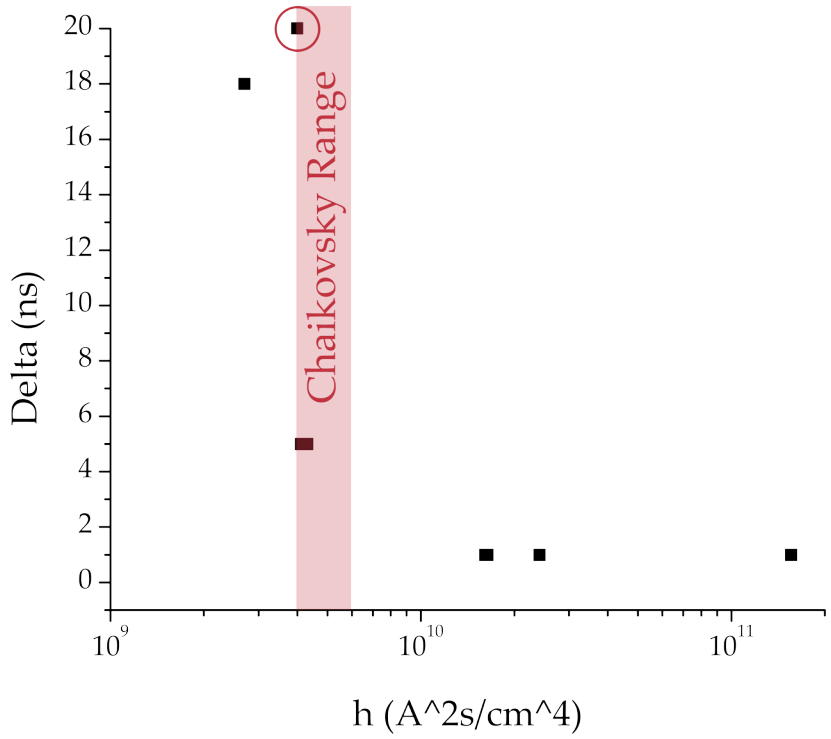

Figure 4.12: Compiled data from initiation experiments showing Delta vs. h, the specific action integral of the material up to the time of initiation. One anomalous data point (circled) was analyzed differently from the rest. Three data points lie within the Chaikovsky range of $(5 \pm 1) \times 10^9$ A^2s/cm^4, with a fourth nearby.

Applying Eq. 4.3 to my thin foil liner experiments (which meet the uniformly distributed current requirement), the integral of j^2 should be equal to the value found in the MIG experiments (i.e. $(5 \pm 1) \times 10^9$ A^2s/cm^4), or at the very least constant. However, as shown in Fig. 4.12, only a few of the liners (the heavier ones) fall within or near the same range. The thinnest liners, which initiated the most uniformly, all have specific action integrals much greater than the Chaikovsky range.

In *J.C. Martin On Pulsed Power*, there is a section covering electrical breakdown of multichannel gaps[59]. In it, he gives an expression for the useful in-

terval during which current channels may close in a multichannel switch as

$$\triangle T = 0.1\tau_{tot} + 0.8\tau_{trans} \tag{4.4}$$

where τ_{trans} is the transit time isolation between adjacent current channels and τ_{tot} is the sum of the e-folding inductive time, τ_L, and the e-folding resistive time, τ_R. All the terms in Eq. 4.4 are dependent on n, the number of current channels that are formed. The inductive term and the transit time isolation both go as as $1/\mathrm{n}$ and the resistive term goes as $1/\mathrm{n}^{1/3}$. Therefore, the more current channels that form (equivalent to uniformity of initiation), the faster the switch closes (equivalent to initiation time). He further defines the deviation in time which a single channel will form as

$$\delta(t) = V\sigma(V)\left(\frac{dV}{dt}\right)^{-1} = T\sigma(t) \tag{4.5}$$

where $\sigma()$ represents the standard deviations, and all other values are taken at the time of breakdown. To "an adequate degree of accuracy," $\triangle T$ from Eq. 4.4 is equal to $2T\sigma(t)$ from Eq. 4.5.

Combining Martin's equations and applying them to my dataset, we see that the initiation duration should be linearly proportional to the voltage divided by the voltage rate of rise

$$\triangle T = 2V\sigma(V)\left(\frac{dV}{dt}\right)^{-1}. \tag{4.6}$$

The inductive voltage, $V = L_0\frac{dI}{dt}$, can be calculated from the directly measured dI/dt and the initial inductance of the liners. Also, the derivative of the voltage can be performed numerically. There is not enough data to perform standard deviation calculations, so that term will be left as a constant unknown. Figure 4.13 shows the plot of Eq. 4.6. The data clearly shows that initiation durations are not linearly proportional to $2V\left(\frac{dV}{dt}\right)^{-1}$. Therefore, liner initiation does not appear to be analogous to multichannel switches.

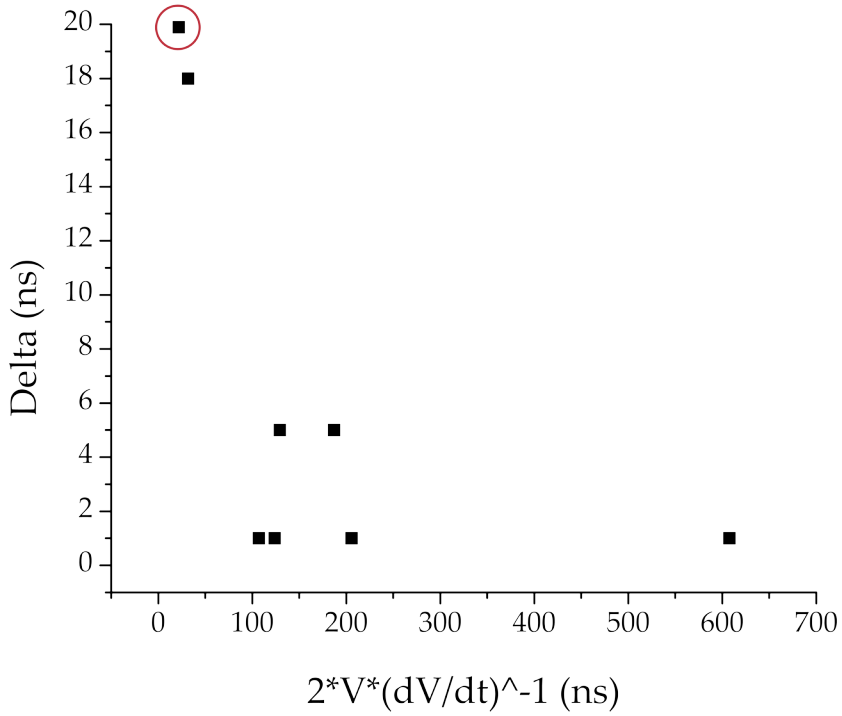

Figure 4.13: Compiled data from initiation experiments showing output of Eq. 4.6. One anomalous data point (circled) was analyzed differently from the rest. The data does not show a linear dependance.

However, if one looks only at the the inductive voltage at the time of initiation, one finds a very strong (inverse) correlation. Figure 4.14 shows a plot of delta versus inductive voltage at the time of initiation. As voltage increases, the duration of initiation decreases. Above about 100 kV, the initiation occurs nearly instantaneously. The linear fit has an R^2 value of 0.98.

An interesting note about Fig. 4.14 is that because all of the loads had the same overall dimensions (only thickness changed) and had roughly the same current pulse, the time-dependant voltage applied to them was nearly identical. The reason why the thinner targets have a larger initiation voltage is because they initiated near peak dI/dt (near peak voltage) whereas the thicker liners initiated near peak I (near minimum voltage). The reason for the differences

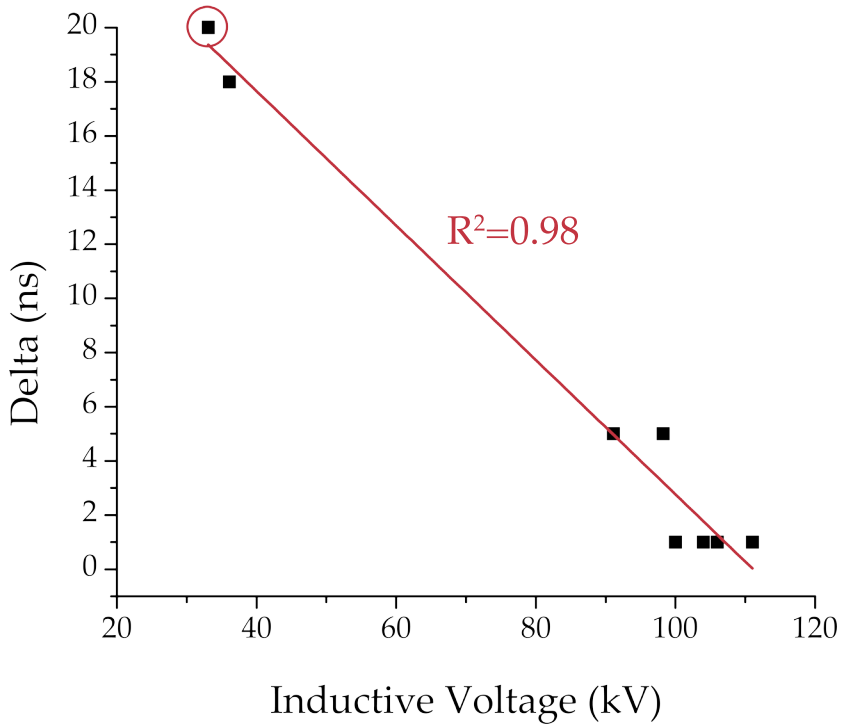

Figure 4.14: Compiled data from initiation experiments showing delta vs. inductive voltage showing a strong (R^2 = 0.98) inverse correlation. One anomalous data point (circled) was analyzed differently from the rest. Above about 100 kV, initiation occurs nearly instantaneously.

in time to initiation is likely due to energy deposition, which is similar to the Chaikovsky hypothesis.

Of all the relations presented, the presence of a dJ/dt threshold and the dependance on applied voltage at the time of initiation have the strongest supporting evidence in our data set. In order to time the initiation such that it occurs near peak dI/dt (which affects both dJ/dt and the inductive voltage), one may have to account for the amount of energy deposited to the target, which is related to the action integral in Eq. 4.3.

Furthermore, to bring the comparison back to wire-arrays, the inductive

voltage could explain why wire-array initiation is less troublesome. As discussed in Section 3.2, wire-arrays have a much higher inductance, which will lead to a much larger voltage. Therefore, they would be more likely to initiate quickly and uniformly based off the findings in Fig. 4.14.

CHAPTER 5

AXIAL X PINCH BACKLIGHTER

5.1 Motivation

The primary motivation for the axial X pinch backlighter was to expand the diagnostic capabilities of COBRA as well as the general Z-pinch community. There are three main categories of imaging diagnostics: self emission, refraction, and absorption. Self emission imaging is usually done with pinholes creating an image onto film or an MCP camera (Sec. 2.3.6) and can utilize visible, XUV, or x-ray photons. These images give qualitative information about the temperature of the plasma. Refraction imaging is performed via laser backlighting (Sec. 2.3.5). If set up as an interferometer, these images can provide quantified information about electron density in the plasma. Absorption imaging is performed via point-projection x-ray backlighting (Sec. 2.3.4). If coupled with a stepwedge calibration system, x-ray backlighting can provide quantitative information about ion density in the plasma. Together, these three imaging techniques compliment each other very nicely.

Since the mid 1990's, these three types of imaging diagnostics have been available for radial (side-on) imaging of Z-pinches. Axial (end-on) imaging is also important for Z-pinch studies because it allows an unobstructed view of every radius (in radial imaging, the wires of an array or the wall of the liner obstruct the view partially or completely, respectively). Self emission pinhole imaging and laser interferometry have been utilized axially for some time, but axial x-ray backlighting had remained elusive... until now!

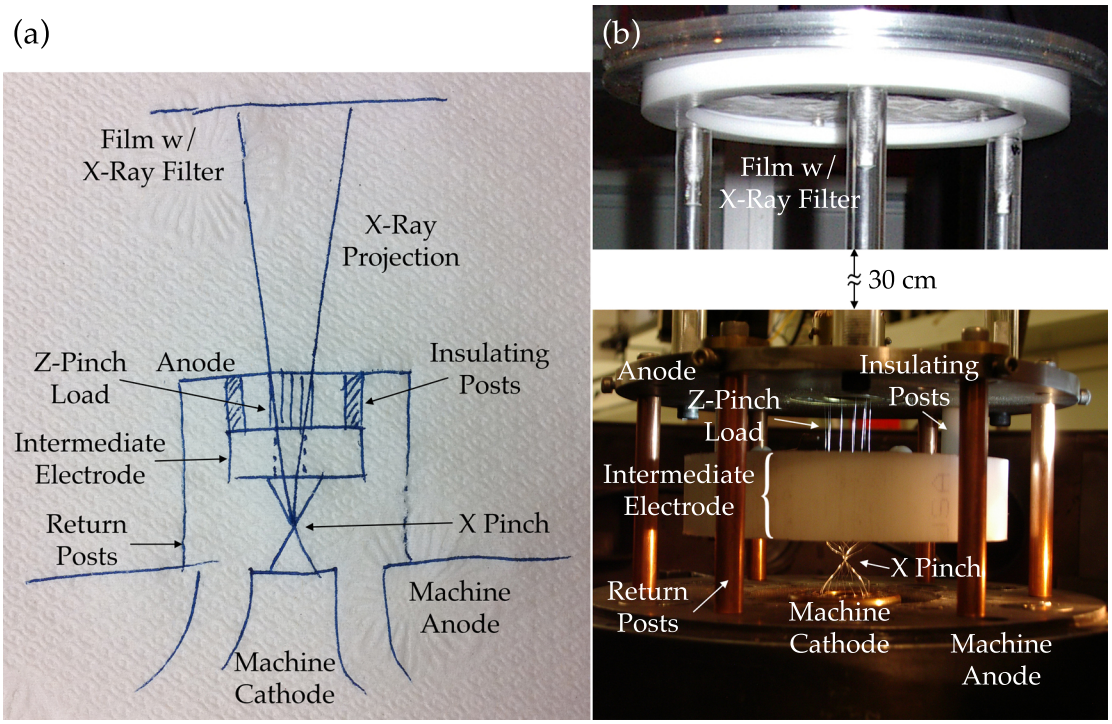

Figure 5.1: (a) Artist's impression of initial design sketch and (b) photographs of original hardware for axial X pinch backlighter.

5.2 Development

The initial concept for the diagnostic was nothing more than a sketch on a scrap piece of paper (Fig. 5.1 (a)). After impressing my advisor with my artistic abilities, I set forth to turn the sketch into the real, usable hardware shown in Fig. 5.1 (b).

About two years later, and 10 series of shots, the original hardware was changed numerous times. These changes fall into three main categories: improving machine operation, improving X pinch characteristics, and decreasing background exposure.

5.2.1 Improving Machine Operation

Many changes were made because the added complexity of the hardware negatively impacted the performance of COBRA and/or the Z-pinch load.

Supporting the Intermediate Electrode

The first change that was made was to change the way the intermediate electrode was supported. The intermediate electrode should be electrically floating - acting as the anode of the X pinches and the cathode of the Z-pinch. Originally, this was attempted using "insulating" plastic posts in parallel with and at a larger radius than the Z-pinch. In retrospect, this was supremely naïve. *Fool me once...* As soon as the plastic posts were exposed to the UV radiation from the Z-pinch, they began to conduct. And because they were a less inductive path than the Z-pinch, they shunted most of the current.

To overcome this, it was decided to support the intermediate electrode off to the side, by long, "insulating" plastic rods (Fig. 5.2 (a)). *Fool me twice...* All of this additional plastic in the load region caused a severe crowbarring of the machine current.

Finally, it was decided to remove all plastic components that might have the opportunity to carry current. The intermediate electrode was made of brass and supported by long brass rods (Fig 5.2 (b)). These brass rods are grounded, but are sufficiently inductive as to not shunt current away from the Z-pinch.

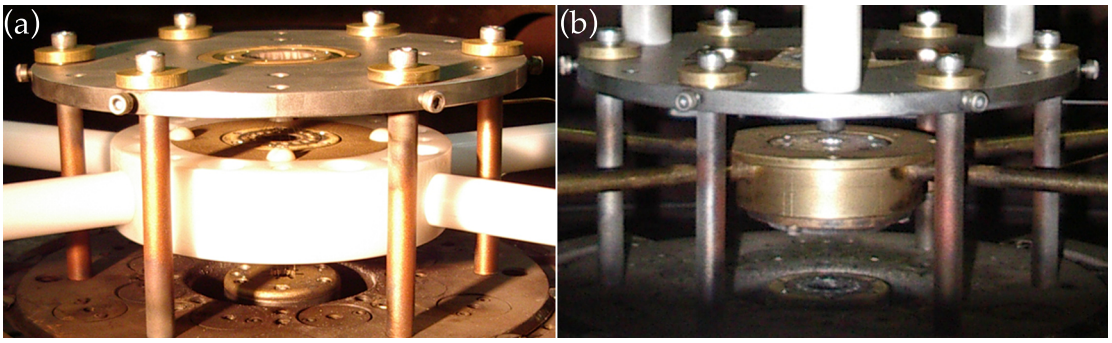

Figure 5.2: Changes to intermediate electrode support (a) using plastic insulating rods and (b) using inductively isolating brass rods.

Eliminating Electrical Breakdown

Throughout the testing of the hardware, there was evidence of electrical breakdown, usually near corners and edges of the extra hardware. The final load design uses rounded surfaces and the gaps between charged surfaces are kept large enough to prevent breakdown from occurring.

Minimizing Added Inductance

With all of the added hardware and complexity, it was inevitable that inductance would be larger than a standard COBRA load. However, wherever possible, we made changes to minimize the inductive hit.

By necessity, the radius of the return current was increased to accommodate that added hardware. This larger radius increased the inductance, but that effect was minimized by increasing the number of return posts from four to six and increasing the diameter of each of the return posts as much as possible.

The height of the Z-pinch load region was only 1 cm, whereas the typical

height of the load region is 2 cm. This not only kept the inductance to a minimum, but also aided in the axial radiography. Because the images are axially averaged, keeping the height of the load as short as possible minimizes the errors that can occur due the divergence of the source.

Having two X pinches in parallel not only minimizes the initial inductance of the X pinch region, but more importantly it minimizes the transient inductance during pinching. When the imaging X pinch pinches, it becomes extremely inductive. If it were the only path for current to flow, the entire load current would suffer. The parallel X pinch provides an alternative current path, minimizing the effect of the added inductance during pinching.

Overall, the inductance did increase, but not very dramatically. This can be seen in the impact of the load current traces. Typical COBRA current is about 1 MA delivered in 100 ns zero-to-peak rise time. With the extra inductance from the added hardware, the 1 MA of current was delivered in 125 ns zero-to-peak.

5.2.2 Improving X Pinch Characteristics

X pinches can be finicky. Most of the information known about what makes a good X pinch is purely empirical and often times poorly documented. In this section, I will attempt to relate what I have heard and learned about X pinch performance. For the purposes of this discussion, a "good" X pinch means: reliably produce a small source size ($\lesssim$5 μm), single hot spot, with a short pulse (<1 ns).

Material

Pretty much any material can make a good X pinch. In my experience, I have seen X pinches ranging from carbon (Z=6) to tungsten (Z=74) produce X pinches. However, the material does change the spectral characteristics of the X pinch emission. For good point-projection imaging, one wants to use the continuum radiation from the X pinch as opposed to the line radiation because the line radiation tends to come from a larger, longer-lived source. Therefore, one needs to find a good combination of X pinch material and x-ray filter material. At Cornell, the most common combination is a molybdenum (Mo) X pinch with a titanium (Ti) filter. Molybdenum only has a few lines in the Ti passband that tend not to disrupt the imaging characteristics too much. Niobium is an even better match for a titanium filter but is not as easy to procure as Mo.

Crossing Angle

The internal angle at which the wires of an X pinch meet is of some importance. It is best to keep the angle between about 60 and 80 degrees. For nested X pinches (see below), that angle is measured using the outermost diameter.

Twisting Angle

An X pinch is usually formed by stringing wires as if one was building a cylindrical wire array. Then, once all the wires are loaded, twist one of the electrodes until the wires cross at a single point. The conventional wisdom is to twist the electrode until the wires just barely touch (I usually say 180° + <30°). However, it is better to overtwist than to undertwist. Therefore, if you are having

difficulties, it is recommended to "twist the shit out of it [60]."

Number of Wires

Four wires tend to work better than two. Beyond that, increasing the number of wires neither helps nor hinders the X pinch, except for the fact that for very massive X pinches you either need to use many small wires or a few large wires. Neither of these options is particularly attractive, because it leads to a sloppy crossing point and therefore a large source size. A good solution to this problem is to use a nested X pinch [46].

Nesting the wires, in two or three layers with varying sizes and/or material leads to a much more ordered crossing point. In this way, even massive X pinches can perform well.

The original design used a simple, multiwire X pinch. Later, thanks to Sergei and Tania, the X pinch was switched to a nested configuration.

Parallel X Pinches

It has been found that two X pinches in parallel tend to work better than a single X pinch on its own. Specifically, single hot spot formation is more common when two X pinches are near eachother. The reasoning for this is because if current continues to flow through an X pinch after it has pinched, it will tend to re-pinch. If, however, there is another path for the current to go after an X pinch has pinched (and become extremely inductive), it will do that and prevent the first pinch from re-pinching. It seems, however, that the alternative path needs

to be of comparable inductance (e.g. another X pinch) to the first X pinch in order for this benefit to occur. I have tried alternatives, but another X pinch just seems to work best.

Having two X pinches in parallel can also be beneficial in lowering the current through the X pinch as compared to having all the current flow through a single pinch. This is beneficial because, as stated above, having a very massive X pinch can cause complications with good pinch formation.

For simplicity, the original design only used a single X pinch. Later, two X pinches were used in parallel, but with only one of the X pinches (the imaging X pinch) on axis. The other X pinch (the side X pinch) was just a dummy load to take the current after the imaging X pinch pinched. Additionally, the side X pinch was overmassed so that it would not radiate strongly and interfere with the calibration of the images.

X Pinch Mass

The timing of an X pinch is linearly proportional to the mass per unit length of the X pinch [61]. Also, X pinches tend to work best when they pinch between peak dI/dt and peak I.

Directionality of X Pinch Radiation

Due to the cylindrical symmetry of an X pinch, the radiation produced from an X pinch is azimuthally uniform. In fact, because the source is so small and often taken to be a point source, the emitted radiation is most-likely spherically uni-

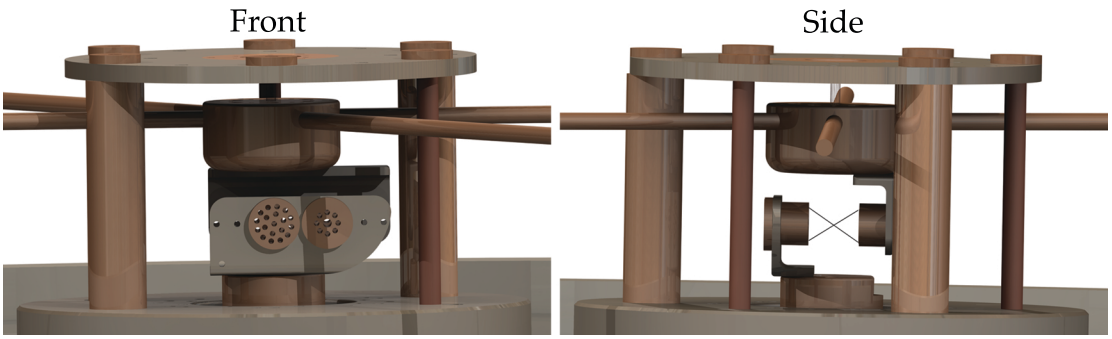

Figure 5.3: Front and side views of parallel, sideways X pinch hardware for axial X pinch backlighting. Note: only one of the X pinches is on axis with the load.

form. However, the distribution of plasma around the point source is not uniformly distributed. Above and below the pinch, dense jets form due to ablated material coming off normal to the wires. These jets absorb the radiation from the pinch, causing poor imaging characteristics from the axes of the X pinch.

The original design had the Z-pinch located directly above the axis of the X pinch. The X pinch was later reoriented 90° to the original location so that the Z-pinch was "off to the side" of the X pinch. This produced much nicer images, but significantly complicated the load hardware.

After adding a parallel X pinch and turning them on their sides, renderings of the hardware are shown in Fig. 5.3

5.2.3 Decreasing Background Exposure

It is important to have the same level of exposure on both the imaging film and the calibration film. This can be difficult to achieve because the two films have separate fields of view. The imaging film can have a line of sight to the anode-

cathode gap of the machine where strong x-rays can be produced. Additionally, its location above the anode of the load puts it in the path of energetic electrons that can get accelerated in the load region. For these reasons, if no precautions were taken, the imaging film would receive a larger x-ray flux and the calibration would be difficult or impossible. To combat this problem, several steps have been taken.

Location of Imaging Film

With the original hardware design (FIg. 5.1) there were many problems with background exposure levels in addition to image resolution. One suggestion was to switch the location of the X pinch and the Z-pinch, putting the X pinch on top and the Z-pinch on bottom. In this way, the imaging film would be placed below the cathode (which is a possibility with COBRA's design). With the imaging film below the cathode, energetic electrons from the load region would no longer be a problem. This idea was tested out, but it turned out to only make the problem worse. The background exposure level was much worse when the imaging film was located below the cathode. The exposure was from extremely energetic x-rays, enough to make it through 175 μm of lead with energies >70 keV. X-rays that energetic were most-likely created by electrical breakdown in the convolute region creating bremmsstrahlung radiation. Because of this strong background radiation, further attempts to image below the cathode were not attempted.

Electron Blockers

With the imaging film above the anode, the background radiation was very uneven and splotchy. This indicated that it was a local source and it was thought that electrons were reaching the x-ray filter adjacent to the film and creating bremmsstrahlung radiation. Electrons have a much larger cross section than photons and are therefore easier to stop. Therefore, we chose a material (~120 μm polypropylene) that would not affect the 3-5 keV imaging x-rays but would block electrons below about 100 keV. This electron blocker was placed about halfway between the anode and imaging film. Blocking the electrons would cause bremmsstrahlung, but because it was created farther from the film and in a low Z material, the x-rays would be less problematic. This worked very well, but did not completely solve the background radiation problem.

Background Collimator

Because the electron blocker was stopping electrons below 100 keV and the background exposure was not completely eliminated we began investigating other sources of exposure. One possibility was that x-rays were making it to the film by way of grazing angle reflections. To eliminate stray x-rays from reaching the film, the entire film holder apparatus was surrounded by a ~1 mm polyethylene sheet, forming what we called the chimney. This chimney made it so that the only way for x-rays to reach the film was through the hole in the top of the anode, which is where the imaging X pinch x-rays travel. The chimney lowered the background exposure, but some radiation persisted.

Electron Diverter

Going back to the energetic electron problem, it was possible that electrons with energies greater than 100 keV were making it through the blocker and reaching the x-ray filter. It is not possible to block these more energetic electrons without starting to attenuate the imaging x-rays. Therefore, we attempted to take advantage of their charge by diverting them out of the way using permanent magnets. A set of magnets, producing a field of about 0.1 T over a roughly 1 $in.^2$ area near the anode is strong enough to deflect electrons with energies up to 500 keV out of the field of the film. The magnets further reduced the background exposure. While the background levels are not always identical, they are usually close enough as to not cause significant errors in calibration. Figure 5.4 shows a histogram analysis of the background levels between the imaging film and the calibration film. The average 16-bit gray level between the two regions are within 3.2% of each other.

After all of the changes to the hardware, the final design is shown in Fig. 5.5.

5.3 Sample Images

Figure 5.6 shows a selection of sample images of loads with three different diameters and two different materials. In general, any load material and diameter will work, provided the correct magnification and x-ray filter are used. For the magnification typically used with this setup, 16 mm is about the largest diameter load that can be used. For the 3-5 keV x-rays selected with the 12.5 μm

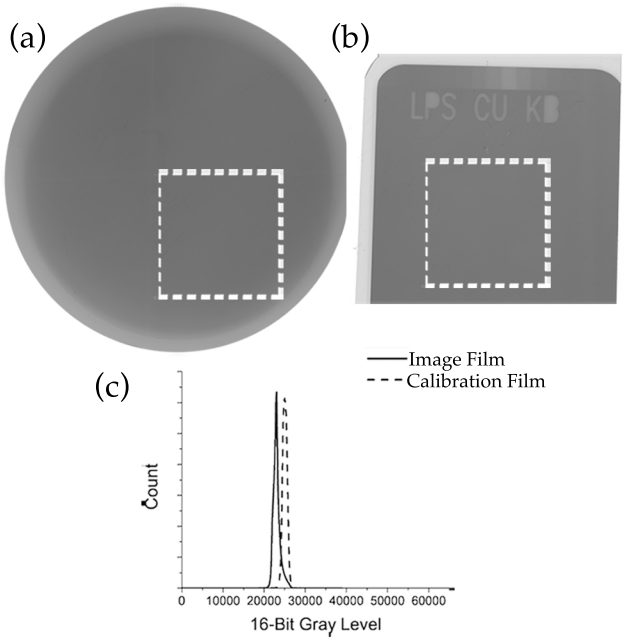

Figure 5.4: Histogram analysis of ackground levels. (a) Image film with indicated histogram area, (b) calibration film with step wedges and indicated histogram area, and (c) histograms showing the image film (solid) at 22,900±600 and the calibration film (dashed) at 25,000±600.

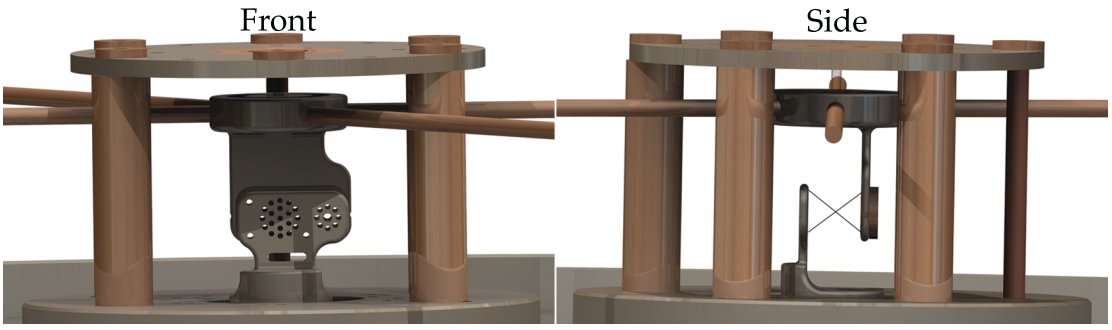

Figure 5.5: Front and side views of finalized hardware. Not shown above anode: permanent magnets, polypropylene electron blocker, titanium x-ray filter, and film cassette.

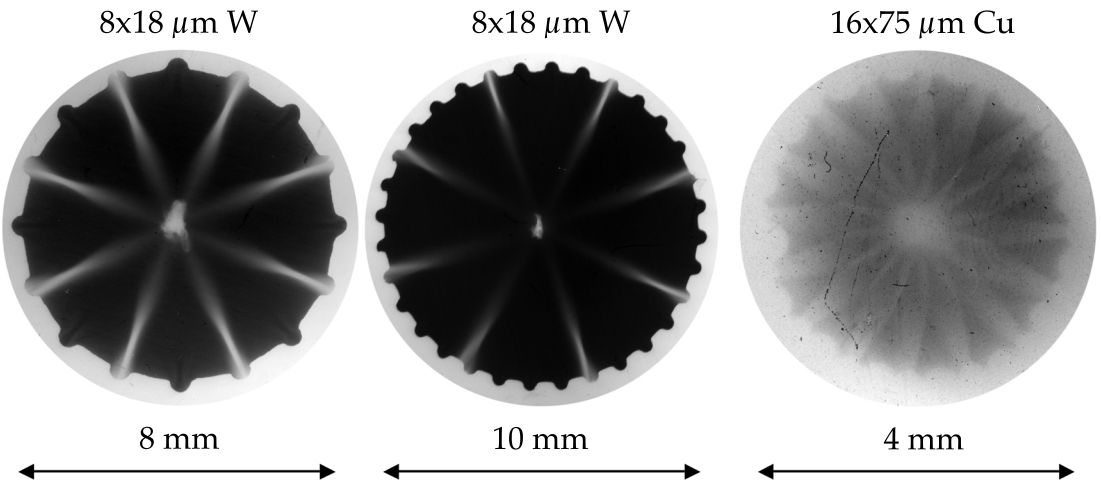

Figure 5.6: Sample images from three different wire-arrays: 8x18 μm W at 8 mm diameter, 8x18 μm W at 10 mm diameter, and 16x75 μm Cu at 4 mm diameter.

titanium filter, the load material needs to be of at least moderate atomic number (e.g. iron (Z=26) or higher). Aluminum (Z=13) tends not to absorb strongly enough to provide adequate contrast. Even copper (Z=29) has somewhat poor contrast (see Fig. 5.6).

5.4 Known Deficiencies

The axial X pinch radiography diagnostic is capable of producing stunning images with quantitative data, but there are some known deficiencies. While the background exposure level has been mostly fixed (Sec. 5.2.3), occasionally the levels will be too far off to be able to give an accurate calibration. In part, this is due to poor X pinch performance, which has been the greatest challenge to solve so far (Sec. 5.2.2). With a strong pinch, the small differences in the background levels are less important. Also related to X pinch performance is the reliability

of the diagnostic. After all of the improvements made, it still only produced nice images about 2/3 of the time. Thankfully, there exists a possible solution to these problems, as discussed below in the next section.

One problem that cannot be fixed, however, is a divergence problem. Due to the point-source nature of the X pinch and the extended nature of the object, a single "ray" of light will be absorbed by plasma at different radii.

The divergence problem is illustrated in Fig. 5.7. The divergence of the source is most problematic when large radial gradients in density exists on scale-lengths comparable to the Δr of a given ray. For example, a ray that passes through the center of the load has $\Delta r = 0$, and therefore does not pose a problem. Likewise, rays passing through the center 2/3 of the load have a small Δr, but pass through a relatively small radial density gradient in the plasma of that region. The main problem exists near the perimeter of the load. There, both Δr and the radial density gradient are at their greatest. A ray that passes through the outermost region of the load can travel through only a ~1 mm region of wire core and the remaining ~9 mm path will be through coronal density. This ray will effectively be labeled as if it traveled straight up through 10 mm of the wire core. In the illustration, the densest portion is recorded as about 10^{19} cm^{-3}. That volume density was calculated assuming the full height of the load. But as mentioned earlier, most of its absorption only occurred in a 1 mm region, so the actual density that should be represented could be an order of magnitude higher. In fact, side-on radiography of similar loads indicates that the density is indeed greater than 10^{20} cm^{-3}[62].

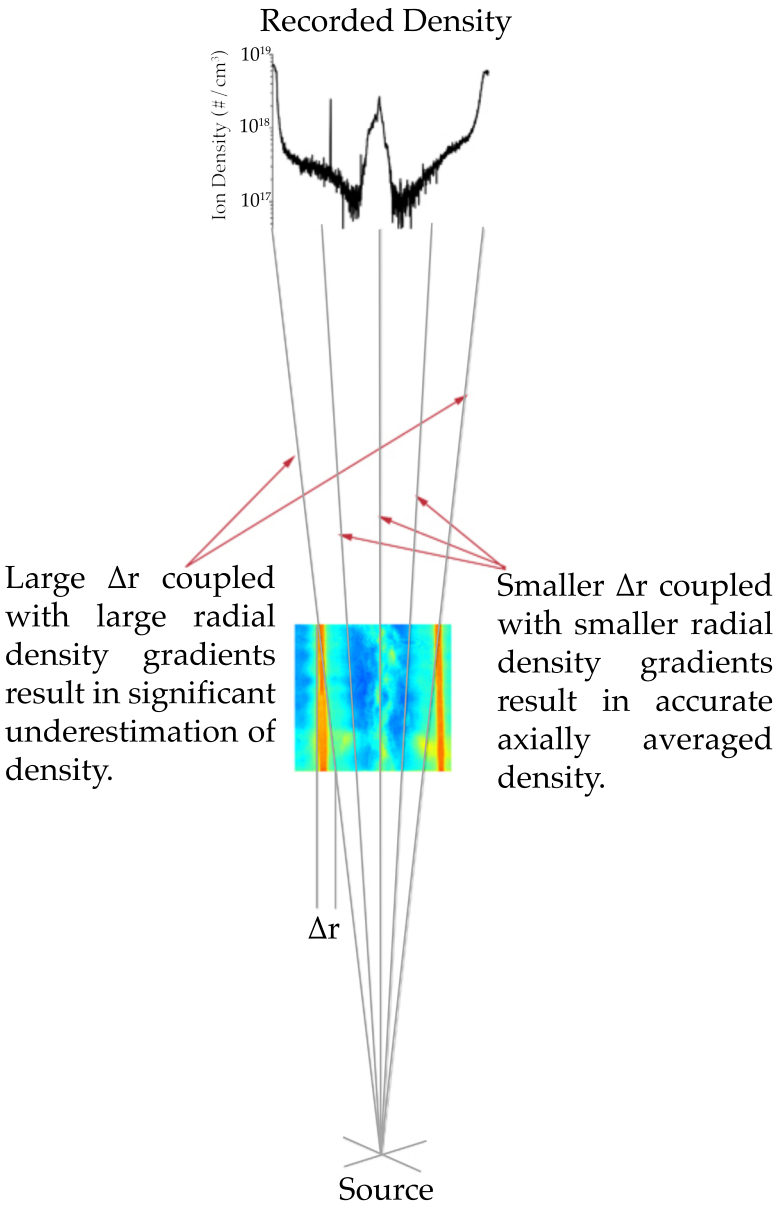

Figure 5.7: Illustration of the divergence problem for axially averaged volume densities. The sample side-on radiograph is located and scaled to the size of loads in the experiments presented, accurately representing the angles and Δr's.

5.5 Possible Improvements

The single greatest improvement to the axial X pinch backlighter diagnostic that can be made is to improve the X pinch operation. Improving the X pinch operation will increase reliability and minimize calibration problems due to poor signal to noise ratios. Presently, the best way to improve the X pinch operation would be to switch to a new kind of X pinch: the recently developed hybrid X pinch[47].

Hybrid X pinches consist of a pair of conical electrodes connected by a short segment of a single wire. Because of the fewer parameters involved, hybrid X pinches are easier to "tune" and are able to produce the same spatial and temporal characteristics of nested or standard X pinches. As a further benefit, hybrid X pinches are much simpler to load, requiring only a single wire each, along with carefully spacing the conical electrodes. In comparison, between the imaging X pinch and the side X pinch used in the experiments presented in this research, I had to carefully load 27 wires. This typically took about an hour and was one of the limiting factors to how quickly shots could be taken.

The simplicity of the hybrid X pinch, alone, is reason enough to make the switch. With some tuning, it is possible for them to produce a single hotspot more reliably and of greater intensity than nested X pinches.

CHAPTER 6

ABLATION AND PRECURSOR FORMATION OF WIRE-ARRAYS VS. THIN FOIL LINERS

6.1 Motivation

In wire-arrays, plasma is ablated approximately uniformly around each wire. Plasma that is created on the inside of the array reaches its way to the axis via a global $\vec{J}\times\vec{B}$ force. Additionally, ablation plasma that is created on the outside of the wire (with respect to the array axis) is swept around the still mostly solid wire core also making its way to the axis via $\vec{J}\times\vec{B}$ forces. In liners, however, plasma that is created on the outside of the liner cannot reach the axis prior to implosion because the solid liner is continuous. Therefore, only plasma that is created on the inside of the liner has a chance to make it to the axis and form a precursor prior to implosion. Also, because the liner will partially prevent field penetration, most of the ablation will occur on the outside.

We present experimental results showing the radial mass distribution of wire-arrays and solid liners made of copper (Cu). The results show that solid liners produce much less precursors than equally massed wire-arrays. However, thin liners are very sensitive to their initial conditions and can produce enhanced ablation and precursors under less than ideal conditions.

6.2 Experimental Setup

The load hardware for these experiments is shown in Fig. 5.5 and is explained in more detail in Ref. [63]. The X pinch x-ray source [44] is located 5.6 cm below the top of the load and allows for an imaging film, placed 33 cm above the top of the load, to capture the attenuation due to the ion density in the r-θ plane of the load. A separate calibration film was located off to the side of the X pinch at the same distance as the imaging film. Both films used a 12.5 μm titanium (Ti) foil as the main x-ray filter. The Ti filter passed x-rays in the 3-5 keV range, where the emission from the X-pinch is primarily continuum. This configuration allows for a diffraction-limited spatial resolution of 3.5 μm (using the 5 keV peak in the Ti transmission window).

Calibration is achieved by using stepwedges on the calibration film, as described in Ref. [63]. The stepwedges in these experiments were varying thickness of copper (Cu). On both the imaging film and the calibration film, the x-rays from the X pinch are attenuated by Cu ions. On the calibration film, the attenuation occurs through a known thickness of solid density, room temperature, Cu stepwedge. On the imaging film, the attenuation occurs through the unknown density, not room temperature, Cu. Depending on the material, the temperature difference can significantly change the opacity, but for Cu it is assumed not to be an issue. By processing the films identically, one can map the known areal density of the steps (and interpolate between the steps) on the calibration film to the unknown density of the imaging film. For more information on stepwedge calibration of radiographs, see for example Ref. [53]. A conversion to average volume density is done by dividing the mapped areal density by the height of the load. Axially averaging the ion density does not mean to im-

ply that the plasma is uniformly distributed throughout the height of the load. These loads are assumed to exhibit a similar axial perturbation that is regularly seen in other Z-pinch loads[3, 64, 65, 66].

In general, the error on the calibrated ion density is approximately ±10% [63], except at the lowest density levels and near the perimeter of the image. At the lowest density levels, the small amount of attenuation is barely noticeable compared to the background (no attenuation) level, which leads to a low signal to noise ratio. Therefore, densities near the lowest step can be off by nearly a factor of 2. Near the perimeter of the image, the combination of the divergence of the point x-ray source and the strong radial density gradients increase the error in converting areal density measurements to average volume densities. The top of the load hardware acts as the final limiting aperture for the imaging x-rays. Therefore, the perimeter of the image is attenuated by only a small (axially) region of plasma near the edge. The rest of the attenuation occurs at a smaller radius and a lower height. This is particularly problematic when large radial densities are present near the perimeter (e.g. near wire cores). The attenuation due to a ~1 cm height of ablated plasma is very minor compared to the attenuation of <1 mm of a near solid density wire core. However, the attenuation path is assumed to be uniform and therefore the <1 mm of solid attenuation is treated as the full height (1 cm). Therefore, quoted densities within ~.25 mm of the perimeter of the image can be greater than an order of magnitude off (too low) and should only be used for qualitative comparisons.

The wire-array loads consisted of sixteen 75 μm Cu wires on a diameter of 4 mm with a height of 10 mm. The liners had the same diameter and height, but to achieve the same mass, were only 6 μm thick. The liners were manufactured at

General Atomics by depositing a very thin layer of copper (<100 nm) on acrylic mandrels and then electroplating the bulk of the thickness. Once the liners were received at Cornell, they were mounted in specially designed hardware (see Fig. 4.1 (a)) and the acrylic mandrel was removed by a leaching process. Once the acrylic was removed, the liners became delicate and care had to be taken to keep them from crinkling or deforming.

The shape of the liner (see Fig. 4.1 (b)) allowed for good contact to be achieved at the cathode, but required the mounting hardware to be constructed out of two separate pieces and bolted together afterward. While achieving good current contact was readily accomplished, it occasionally resulted in pinching the liner and causing a crinkle. These crinkles were undesirable because they negatively affected the uniformity of plasma development. The quality of the current contact was primarily determined by radiographic evidence during the shot. When good contact was achieved, plasma was created uniformly around the liner. When poor contact was achieved (or only good contact in one particular region), plasma formation was not uniform and was enhanced in the regions that were pinched.

6.3 r-θ Density Maps

Three representative radiographs are shown Fig. 6.1 along with their calibrated false-colored counterparts. All three images were taken near peak current (1 MA with a rise time of 125 ns) and represent three different loads. The sixteen wire, 75 μm Cu array (Fig. 6.1 (a) and (b)) shows a well-formed, dense precursor and a complex interaction structure from all the mass that has been ablated from

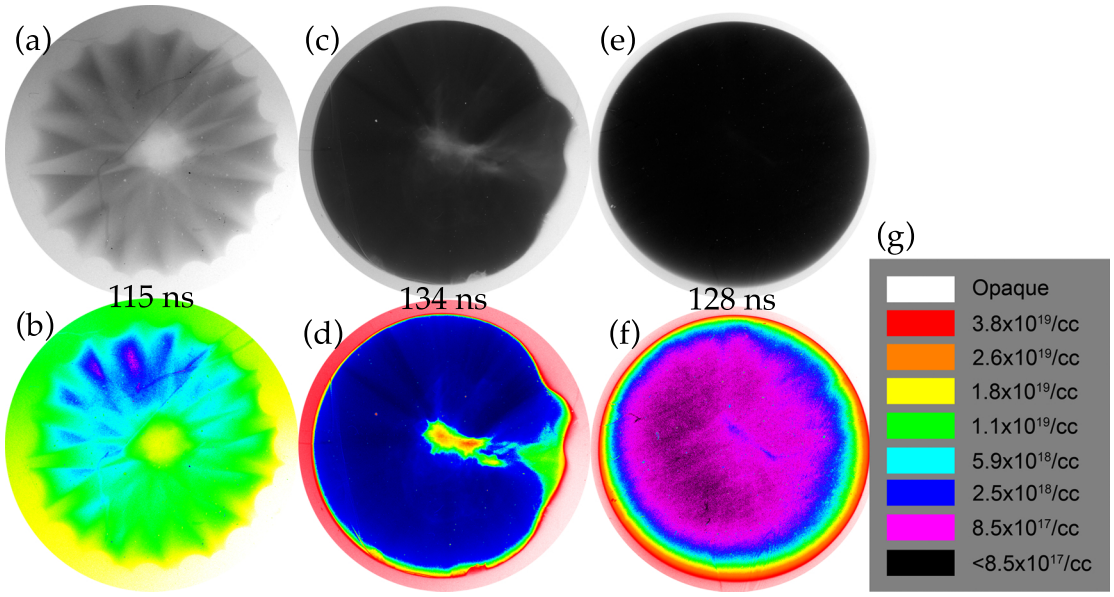

Figure 6.1: Gray scale and calibrated false-colored radiographs of (a) and (b): 16-wire, 75 μm Cu array; (c) and (d): 6 μm Cu liner with crinkle in 3 o'clock position; (e) and (f): 6 μm Cu liner with no perturbations. The legend in (g) shows the calibrated axially averaged ion density for the three false-colored images. All loads were 4 mm diameter and 10 mm tall.

each wire. The 6 μm Cu liner with a perturbation (Fig. 6.1 (c) and (d)) shows a dense precursor and uniform, lower density ablation, except near the perturbation. Near the perturbation, there is nearly an order of magnitude increase in ablation density that is the prime contributor to the precursor mass. The 6 μm liner without perturbation (Fig. 6.1 (e) and (f)) shows a nearly uniform prefill plasma produced symmetrically around the azimuth with only a small increase in density near the center.

The differences between the wire-array and the two liners is very striking. With the wire-array, each individual wire core is producing a primary plasma region, as one would expect. However, because the wires used in these experiments consisted of very thick copper, they have expanded dramatically. The expanded wire cores have merged between each ablation stream, resulting in

a secondary interaction region that is about twice the density of the primary region. Farther in toward the axis, two secondary regions meet and appear to form a shock, just prior to reaching the precursor plasma. These tertiary regions are again about double the density of the nearby contributing secondary regions and are located in line with the original, primary ablation stream. The precursor, despite being formed from such a complex source, is relatively uniform and centered on the axis.

To check whether it is reasonable to assume shocks are present, one can look at the ion-ion collision frequency for two interpenetrating beams, as shown in Ref. [67].

$$\nu_{ii} = \frac{n_i Z^4 e^4 \ln \Lambda}{4\pi\epsilon_0^2 M_i^2 V^3} \tag{6.1}$$

where n_i is the ion density, Z is the average charge state of the ions, e is the electron charge, ln Λ is the Coulomb logarithm, ϵ_0 is the vacuum permittivity, and M_i is the ion mass. The mean free path is then $\lambda = V/\nu_{ii} \sim V^4$. Because the streams are not travelling directly into each other, but at a half angle of 6.25°, the orthogonal velocity of the ~65 km/s streams become ~7 km/s. Using $n_i \sim 10^{19}$ cm^{-3}, $Z \sim 5$, and $V \sim 7$ km/s results in a mean free path of <1 nm which is obviously very collisional. The reason for the high degree of collisionality is due to the V^4 scaling of λ and the fact that the streams are colliding at a small angle. Nonetheless, if one were to use a larger stream velocity or a larger collision angle, Eq. 6.1 would still result in a collisional plasma for any reasonable conditions. This calculation also indicates that the secondary region is collisional and the sharp interactions at those locations represent shocks.

Compared to the wire-array, both the perturbed and non-perturbed liners are relatively simple, but the differences and similarities between the two are

very interesting. Both liners show an overall tendency to produce plasma uniformly around most of their azimuth. This plasma is 2 to 10 times lower in density than the ablated plasma from the wire-array. However, at the perturbation, the ablated plasma is about the same density as the wire-array ablation and produces a slightly off-axis precursor of comparable density to the wire-array. The perturbation was caused by the segmented load hardware (Fig. 4.1 (a)). The two pieces of hardware pinched the liner on one side. It is unclear whether or not the ablated plasma at the perturbation extends the full height of the load, but it is likely that the plasma is concentrated near the cathode and could be a factor of two higher density (if it only extends the bottom half of the liner). Due to the increase in ablation at that location, there appears to be more current flowing there. The increased ablation could have weakened that location, causing a hole that would allow the plasma that builds up on the outside of the liner to penetrate and make its way to the axis. The liner without a perturbation shows uniform contribution to the plasma prefill from around its azimuth with an order of magnitude less density throughout the inside as compared to the wire-array.

The reason these liners ablate at all on the inside, is because they are much thinner than the skin depth of copper on COBRA. Using room temperature resistivity and the 125 ns sine-squared current pulse from these experiments, the skin depth of copper is 33 μm and will only increase as the liner is heated. Plasma that is ablated from the inside wall of the liner is immediately swept to the liner axis.

6.4 Radial Mass Profiles

The radial distributions of mass for the sixteen wire, 75 μm array and the unperturbed 6 μm liner are shown in Figs. 6.2 and 6.3, respectively. Each figure shows a section of the radiographs from Figs. 6.1 (a) and (e). An illustration of the overlapping streams from the wire-array is provided in Fig. 6.2 (b). In the simple illustration, three identical streams are overlapped creating perfectly straight overlapping regions. In contrast, particularly in the tertiary region of the radiograph, one can see that the overlapped section is formed at a different angle from the two incoming secondary regions. As discussed earlier, this change in angle is indicative of a shock caused by the interaction of two secondary regions.

The data in the plots of Figs. 6.2 and 6.3 include the entire area of the radiograph, not just the section shown. The first plot shows mass density in mg/cm^3 as a function of radius. Each individual gray data point represents the density in one 7 μm pixel in the frame of the load. Multiple points at a given radius represent different azimuthal positions. The two lineouts in Fig. 6.2 (c) were taken as indicated in Fig. 6.2 (a). The second plot in each figure shows the mass fraction (ablated mass inside a given radius divided by total load mass) in percent as a function of radius. This data was calculated by performing a surface integral over the entire region of the calibrated film.

The differences between the wire-array and the unperturbed liner that were discussed previously are also visible in these plots versus radius. The large variations in density at any given radius in Fig. 6.2 (c) are indicative of the large azimuthal variation in the ablation pattern of the wire-array. Compare that to

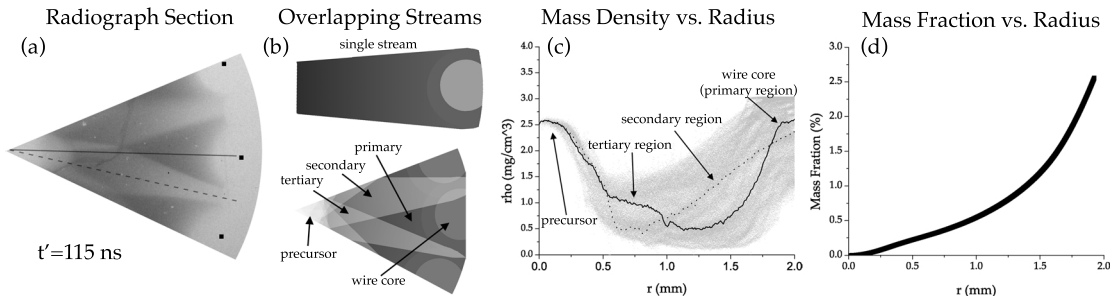

Figure 6.2: (a) Radiograph section of 16x75 μm Cu wire array along with (b) an illustration of the overlapping plasma regions. (c) Mass density and (d) mass fraction as a function of radius for the wire-array. The solid and dotted lines in (c) represent lineouts taken from (a) as indicated.

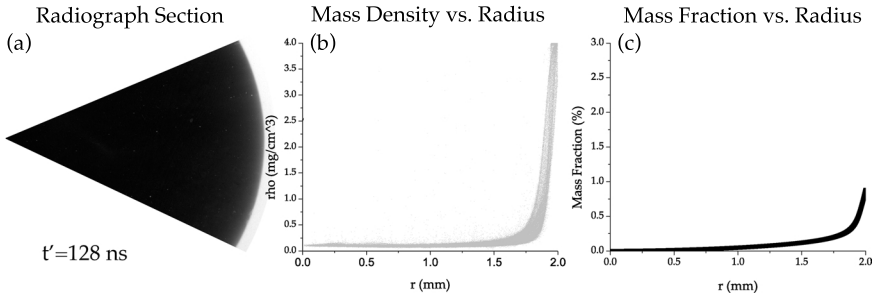

Figure 6.3: (a) Radiograph section of 6 μm Cu liner with no perturbation. (b)Mass density and (c)mass fraction as a function of radius for the liner.

the relatively narrow distribution of densities at any given radius for the liner (Fig. 6.3 (b)). Also, the complex interaction patterns in the wire array are clearly identifiable in the two lineouts in Fig. 6.2 (c). The solid lineout was taken along the original wire position whereas the dotted lineout was taken between two wire positions (in line with the secondary plasma region). Following these lineouts on the graph, starting at r=2 mm and working toward r=0, one first sees the wire core in the primary region being the higher density. Next, farther in, the secondary region where two primary regions are overlapping, is at the higher density. Then, still farther in, two of the secondary regions overlap in line with the primary region, creating the tertiary region before reaching the precursor.

Looking at the overall mass density versus radius between the wire-array and liner, one can see that there is, on average, about an order of magnitude less mass at any radial position in the liner as compared to the wire-array. Additionally, the total fraction of mass inside a given radius is very different. Inside a radius of 1.75 mm (recall that the data beyond that radius is underestimated due to the divergence of the x-ray source), the wire-array has accumulated about 2% of its total mass whereas the liner has only accumulated about 0.25%. In both cases, almost all of the mass is still stationary at the original load radius. The reason for that is both of these loads were extremely overmassed so that they would not implode and produce x-rays which would cause problems with the radiographs by completely washing out the image.

6.5 Comparison with Rocket Model

The ablated plasma from stationary wire cores can be represented by the rocket model [65], which uses momentum balance between magnetic field and the ablated mass:

$$V\frac{d\hat{m}}{dt} = -\frac{\mu_0 I^2}{4\pi R_0} \tag{6.2}$$

where V is the ablation velocity, $\hat{m}$ is the mass per unit length of ablated material, μ_0 is the permeability of free space, I^2 is the current delivered to the array, and R_0 is the array radius.

For a given ablation velocity, Eq. 6.2 can be integrated to determine the total mass per unit length that has been ablated, which is given by

$$\delta\hat{m}\,(t') = \frac{\mu_0}{4\pi V R_0}\int_0^{t'} I^2 dt. \tag{6.3}$$

From Eq. 6.2, it is also possible to construct the radial mass distribution at some time, t', taking into account the time delay required for material to reach some radial postion, r. By doing this, the azimuthally averaged mass density can be written as:

$$\rho(r,t') = \frac{\mu_0}{8\pi^2 R_0 r V^2}\left[I\left(t' - \frac{R_0 - r}{V}\right)\right]^2. \tag{6.4}$$

For times $t' > R_0/V$ it is assumed the ablated plasma is accumulated in the precursor plasma with radius R_p. Using Eq. 6.3 and integrating up to $t' - (R_0 - R_p)/V$ and dividing by the area of the precursor leads to the mass density of:

$$\rho_p(t') = \frac{\mu_0}{4\pi^2 R_p^2 V R_0}\int_0^{t'-[(R_0-R_p)/V]} I^2 dt \tag{6.5}$$

Figure 6.4 shows the azimuthally averaged mass density found by averaging over all of the azimuthal data at every radius from the radiograph data in Fig. 6.2 (c) for the sixteen wire, 75 μm Cu array. Equations 6.4 and 6.5 have also been plotted for various ablation velocities, using $I = I_0 sin^2(\pi t/125ns)$, $I_0 = 1$ MA, $R_p = .25$ mm (from radiograph), and $t' = 125$ ns.

The best rocket model fit for the data is obtained with an ablation velocity of around 65 km/s. This value matched the build up of plasma near the precursor very nicely, but underestimated the stream density and overestimated the precursor density. All of the precursor densities for the various ablation velocities were overestimated. For 65 km/s, a precursor density of 169 mg/cm^3 was calculated using the rocket model, as compared to an experimentally observed value of only 2.5 mg/cm^3.

An ablation velocity of 65 km/s is lower than results from other experiments[65, 67, 68]. The reason for this difference as well as the relatively poor fit of the rocket model for a large portion of the data could be due to the

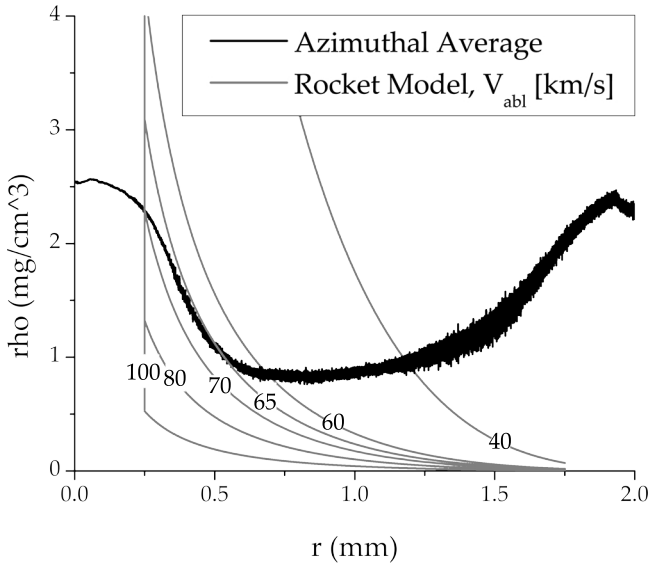

Figure 6.4: Azimuthally averaged mass density taken from radiograph data compared with various rocket model velocities.

compact nature of the array. The combination of large (~500 μm diameter) expanded wire cores located at a small array radius leads to an unusually disproportionate amount of the array consisting of dense, mostly stationary plasma. The coronal plasma around each wire core is much denser and slower moving than the ablation streams. As plasma leaves the wire core and passes through the coronal region, it gets accelerated up to the ablation velocity along with a corresponding drop in density. The rocket model, therefore, is only applicable outside the corona radius (approximately 0.5 mm inside the original array radius). In more typical array sizes, with small wires at a radius of 8 mm, this corona region only occupies a small portion of the load and the rocket model tends to provide a closer fit.

6.6 Discussion

The r-θ density maps and radial mass profiles show strong differences in ablation and precursor formation between wire-arrays and liners. Due to their discrete nature, wire-arrays have complex, azimuthally varying ablation structures that lead to dense precursor formations. Ablated plasma from outside the wires, with respect to the axis, is allowed to flow between the solid wire cores and reach the axis. Liners, however, tend to remain solid and prevent plasma formed on the outside of the liner from reaching the axis prior to implosion. Therefore, only plasma created on the inside of the liner can reach the axis. Due to the partial shielding of the field, much less material is ablated on the inside of the liner as compared to the outside which leads to a greatly reduced precursor mass as compared to wire-arrays. Additionally, ablation on the inside of the liner is minimized because the ablated plasma is immediately swept toward the axis instead of getting pushed back into the liner as is the case on the outside (or due to the local field around individual wires in wire-arrays).

The initial conditions of the liner are important to their final behavior. If perturbations exist, ablation can occur non-symmetrically which typically leads to uneven and increased precursor formation.

The rocket model does not closely match the ablation and precursor densities throughout our data. This is likely due to combination of a small array radius and large, expanded wire cores. The plasma leaving the wire cores undergoes an acceleration phase over a few hundred micrometers prior to entering the ablation stream. In the case of these small arrays, the acceleration region accounts for about a quarter of the load radius. Therefore, the rocket model, which as-

sumes a constant ablation velocity, is not valid over an unusually large portion of our load region.

CHAPTER 7

INSTABILITY ANALYSIS OF WIRE-ARRAYS VS. THIN FOIL LINERS

7.1 Motivation

As mentioned in Sec. 3.2, one consequence of the continuous nature of liners (versus the discrete nature of wire-arrays) is that plasma builds up on the outside of liners. In wire-arrays, plasma that is created on the outside of the wires gets swept around the wire and makes its way to the array axis through the spaces between the wires. In liners, however, the plasma on the outside just gets pushed back onto the liner, where it builds up and ablates the liner surface. As it turns out, this build up of plasma on the outside of the liner is unstable and behaves quite differently than the well-studied axial instability in wire-arrays.

7.2 Evidence

The difference between the wire-array and liner instabilities was noticed in laser shadowgraph images. Figure 7.1 shows a timeline of shadowgraph images for 16x75 μm Cu wire-arrays (top) and 6 μm Cu liners (bottom). It is very evident that the instability on the liners grows to a much larger amplitude and develops a much longer wavelength than in wire-arrays. In all of the images, the original 4 mm load diameter is indicated by a pair of thin white lines. In all cases, the plasma has expanded outward from the original position. In the wire-array images, a very fine-structure instability is present, but it is barely visible because the individual instabilities from multiple wires end up overlapping. In liners,

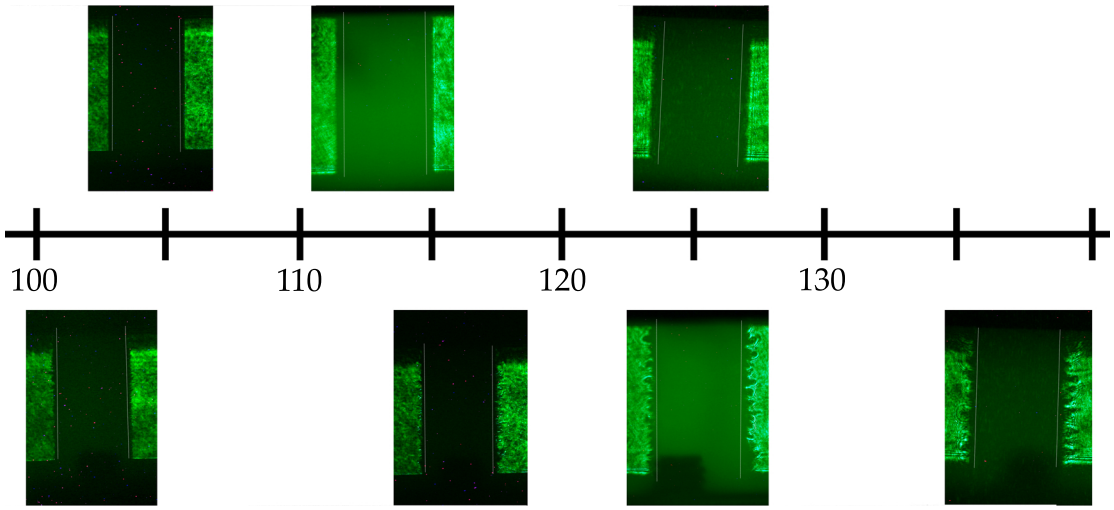

Figure 7.1: Timeline of shadowgraph images showing the differences in instability growth between 16x75 μm wire-arrays (top) and 6 μm liners (bottom). The original load diameter (4 mm in all cases) is indicated by a pair of thin white lines in each image. The liner instability grows to a much larger amplitude and develops a much longer wavelength than the equivalent wire-array instability.

however, the instabilities are able to be azimuthally correlated and because the plasma has no means of reaching the axis (at this time in the current pulse), the instability grows.

Figure 7.2 better illustrates the differences between instability development in wire-arrays compared to liners. The two images, both taken at peak current (125 ns), show significantly different behavior. Both plasmas have expanded beyond the original 4 mm diameter of the load (indicated by the thin white lines). However, the liner shows a large amplitude, long wavelength instability whereas the wire-array is relatively smooth. Again, this is most-likely because the short wavelength instabilities on each of the closely spaced wires has overlapped in the image, causing a smoothing effect.

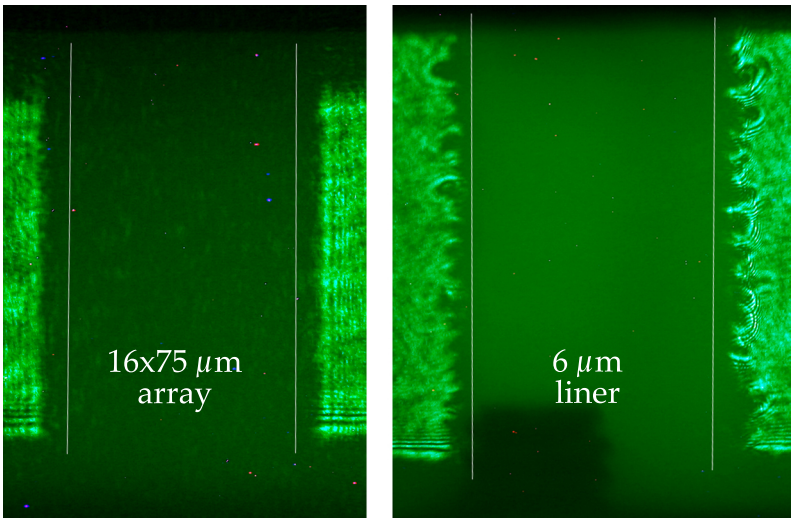

Figure 7.2: A zoomed in view of two images from Fig. 2.10 taken at 125 ns. The pair of white lines in each image indicate the original 4 mm diameter of each load. The instability of the 6 μm liner is significantly larger amplitude and longer wavelength than the wire-array instability.

7.3 Simulation Analysis

In order to determine a possible cause of this new instability, I performed a series of simulations using the recently developed PERSEUS code.

7.3.1 PERSEUS

PERSEUS (Plasma as an Extended-MHD Relaxation System using an Efficient Upwind Scheme) was developed by Martin and Seyler at Cornell[69]. For details of the overall algorithm, see Martin's thesis[70]. A unique aspect of PERSEUS is that a given simulation (initial conditions, boundary conditions, conductivity models, etc.) can be performed in either a resistive magnetohydrodynamics (MHD) mode, or an extended MHD (XMHD) mode by simply

commenting out a few lines of code (and uncommenting some others).

The XMHD model is a two-fluid model that includes electron inertia and the Hall effect, which show up in the full Generalized Ohm's Law (GOL):

$$\frac{\partial \mathbf{J}}{\partial t} = -\nabla \cdot \left(\mathbf{vJ} + \mathbf{Jv} - \frac{1}{ne}\mathbf{JJ} - \frac{e}{m_e}\bar{\mathbf{I}}p_e \right) + \frac{ne^2}{m_e}\left(\mathbf{E} + \mathbf{v} \times \mathbf{B} - \frac{1}{ne}\mathbf{J} \times \mathbf{B} - \eta \mathbf{J} \right) \tag{7.1}$$

where $\mathbf{E}$, $\mathbf{v}$, $\mathbf{B}$, and $\mathbf{J}$ are the vector electric field, bulk plasma flow velocity, magentic field, and current density; $\bar{\mathbf{I}}$ is the identity tensor; n is the plasma denisty; e is the electron charge; p_e is the electron pressure; m_e is the electron mass; and η is the plasma resistivity. Following the relaxation method from Ref. [69] where the characteristic time scales of interest are much slower than the characteristic electron plasma and electron cyclotron frequencies and the ratio of the characteristic spatial scale to the electron inertial length is large, Eq. 7.1 reduces to:

$$\mathbf{E} + \mathbf{v} \times \mathbf{B} = \eta \mathbf{J} + \frac{1}{ne}\mathbf{J} \times \mathbf{B} - \frac{1}{ne}\nabla p_e. \tag{7.2}$$

Each term in the GOL represents an electric field in V/m and can represent a force if multiplied through by a charge. The first term on the right hand side (RHS) of Eq. 7.2 is the resistive term. The second term on RHS of Eq. 7.2 indicates that the electrons and ions can decouple and move separately, leading to the Hall term. Finally, the third term on the RHS of Eq. 7.2 represents the force due to gradients in the electron pressure.

For the simulations presented later in this chapter, the electron pressure term in 7.2 was neglected, resulting in Hall MHD with the following GOL:

$$\mathbf{E} + \mathbf{v} \times \mathbf{B} = \eta \mathbf{J} + \frac{1}{ne}\mathbf{J} \times \mathbf{B}. \tag{7.3}$$

Resistive MHD additionally considers the Hall term to be negligible, resulting in:

$$\mathbf{E} + \mathbf{v} \times \mathbf{B} = \eta \mathbf{J}. \tag{7.4}$$

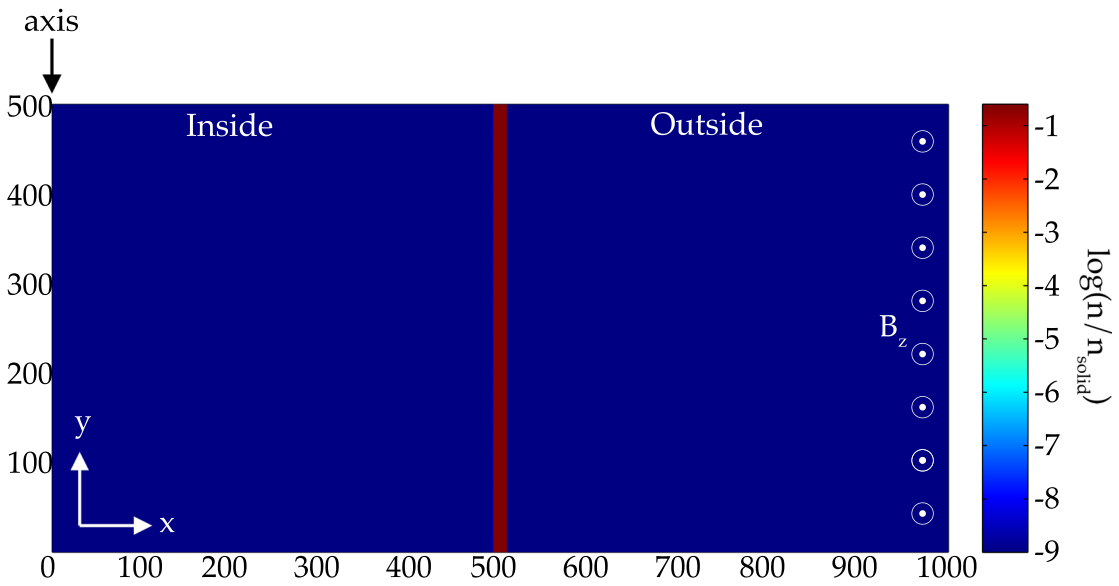

Figure 7.3: Initial conditions for both MHD and Hall MHD simulations showing a solid density slab in the center of the domain.

7.3.2 Simulation Parameters

The initial conditions for the simulations discussed in this chapter are illustrated in Fig. 7.3. The simulations were 2D (xy) with 1 μm resolution. A slab (infinite in the z-direction) of solid density aluminum plasma is initialized with a ±20% random density perturbation between 500 and 515 micrometers on the x-axis. The left edge (with a reflecting boundary condition) represents the axis of a cylinder (if it were an r-z simulation) and along the two right-most cells (with an open boundary condition), a time-dependant magnetic field is applied such that it drives a 1 MA sine-squared, 125 ns current pulse in the plasma. The top and bottom boundary conditions are periodic. If driven to implosion, the slab would move from the center of the domain to the far left. Aluminum was used in the simulations (instead of copper, which was used in the experiments) because it simplifies the requirements of the code. With higher atomic number materials, resistivity models get more complicated and radiation effects can

become important. With aluminum, a modified Lee-More-Desjarlais resistivity model can be used and radiation is relatively unimportant.

Again, the initial conditions described above were exactly the same between the MHD and Hall MHD simulations. The only difference lies in the GOL, as discussed in Sec. 7.3.1. Also, for MHD, an artificial vacuum resistivity must be used to keep current from flowing in the vacuum. For these simulations, a factor of $2 \times 10^4 \cdot rh\_floor$ was used (with $rh\_floor = 1.0 \times 10^{-9}$).

7.3.3 MHD vs. Hall MHD

The time-evolution of the plasma slab for MHD and Hall MHD is shown in Fig. 7.4. Even as early as 10 ns, the two simulations show differences. The plasma slab in the MHD simulation expands uniformly and stays confined about its original position, whereas in the Hall MHD simulation, the plasma on the inside of the slab begins to accelerate toward the left (axis). At 20 ns in the MHD simulation, the plasma on the left of the slab begins accelerating toward the axis, much like in the Hall MHD case. However, by 20 ns, the Hall MHD simulation has already formed a very fine-structure instability on the right-hand side of the slab.

Over the next three frames of Fig. 7.4, the MHD simulation continues to expand, roughly uniformly, and plasma flows toward the left whereas the instability formed in the Hall MHD plasma continues to grow. This trend continues throughout most of the current pulse, until the bulk of the slab begins to implode. At that point, the MHD slab begins forming a typical magnetic Rayleigh-Taylor (MRT) instability on the right-hand side of the imploding slab.

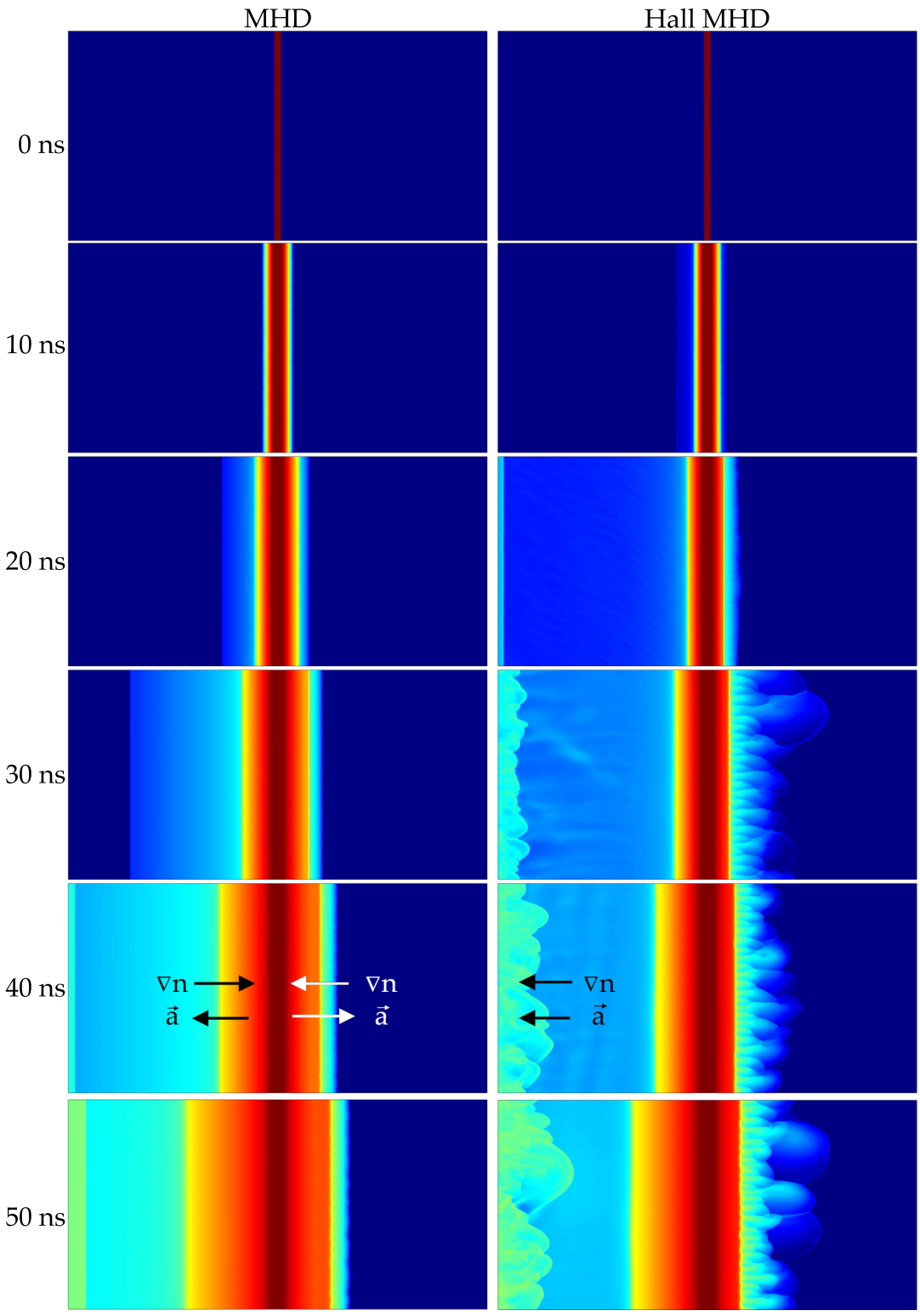

Figure 7.4: Time sequence of density plots comparing instability development between MHD and Hall MHD simulations.

The reason that the slab in the MHD simulation does not form an instability is because it is, in fact, MRT and m=0 stable throughout most of the current pulse. In order for an MRT instability to develop, the acceleration vector and density gradients need to be pointing in the same direction. For the MRT instability, the light fluid is the magnetic field and the heavy fluid is the plasma. If the kinetic pressure is greater than the magnetic pressure, the plasma will expand (see Bennett equilibrium Sec. 1.2) due to a net outward force. This is the case during the majority of the current pulse for the simulations (and for all of the images presented in Fig. 7.4). It is not until near peak current where the magnetic field pressure is greater than the kinetic pressure and the plasma begins to accelerate toward the axis due to a net inward force. At that point, the plasma is MRT unstable and the instability begins to develop in MHD. Additionally, the plasma is m=0 stable, because in the 2D simulation, there is no x-dependance on the magnetic field on the outside of the plasma. In radial geometry, any plasma that gets perturbed to a larger radius than the bulk will experience less magnetic pressure and expand even further outward (unstable). In slab geometry, the magnetic field is constant on the outside of the slab, so there is no runaway effect.

These conditions hold for both the MHD and Hall MHD simulations. Therefore, for the Hall MHD simulation to be unstable, it must be something other than MRT or m=0 instability.

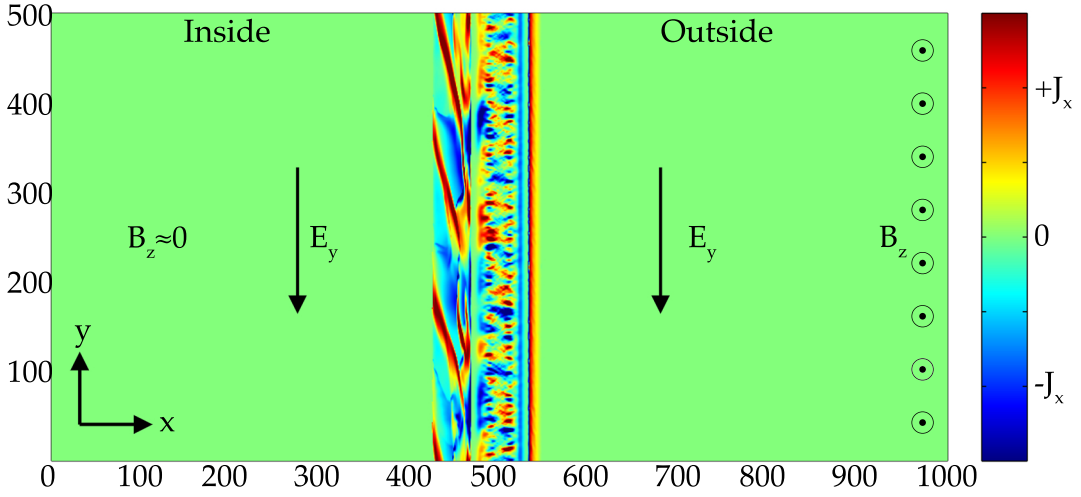

Figure 7.5: Early time (10 ns) plot of horizontal current density, J_x, from Hall MHD simulation. The Hall term in the Generalized Ohm's Law causes a current density flowing to the right (shown in red and yellow) on the outside of the liner.

7.3.4 Possible Source of Instability

In looking closely at the simulation data for the Hall MHD case, it appears that the instability is caused by a shear flow. Early in time, at about 10 ns, an outward current density is established due to the Hall term in the GOL (see Fig. 7.5 and Eq. 7.5). By taking the y-components of Eq. 7.3, we get

$$E_y = -\frac{1}{ne} J_x B_z. \tag{7.5}$$

Because E_y is negative and B_z is positive, J_x must be positive (flowing to the right).

The outward current density, J_x, interacts with the applied magnetic field, B_z, via the momentum equation to produce a downward flow velocity, v_y (see Fig. 7.6 and Eqs. 7.6 and 7.7). The momentum equation is

$$\rho\left(\frac{\partial \mathbf{v}}{\partial t} + \mathbf{v}\cdot\nabla\mathbf{v}\right) + \nabla p = \mathbf{J}\times\mathbf{B} \tag{7.6}$$

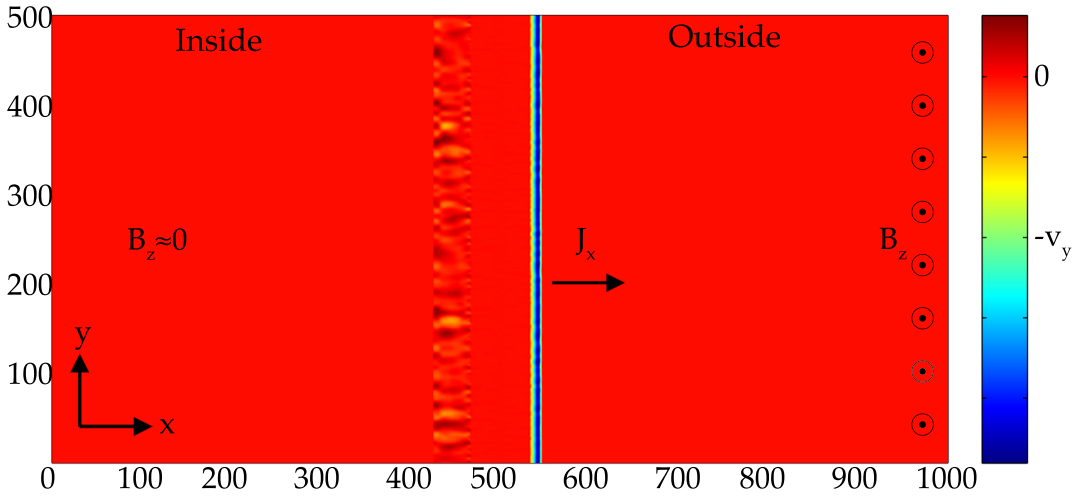

Figure 7.6: Early time (10 ns) plot of vertical plasma flow, v_y, from Hall MHD simulation. The outward current density, J_x, developed in Fig. 7.5, along with the applied B_z produce a downward v_y (shown in blue) via the momentum equation.

and by taking the y-components (and once again neglecting the pressure gradient) leads to

$$\rho \frac{\partial v_y}{\partial t} = -J_x B_z. \tag{7.7}$$

Because J_x and B_z are both positive, Eq. 7.7 leads to a negative (downward) acceleration of the plasma.

Finally, this downward plasma flow is shear unstable and develops later in time to a much larger instability (see Fig. 7.7).

7.4 Discussion

While the shear flow seems to be the cause of the instability in the Hall MHD simulations, it is not the only possibility. For the experiment, two other possibilities are the electrothermal instability or the m=0 instability. I've tried to rule

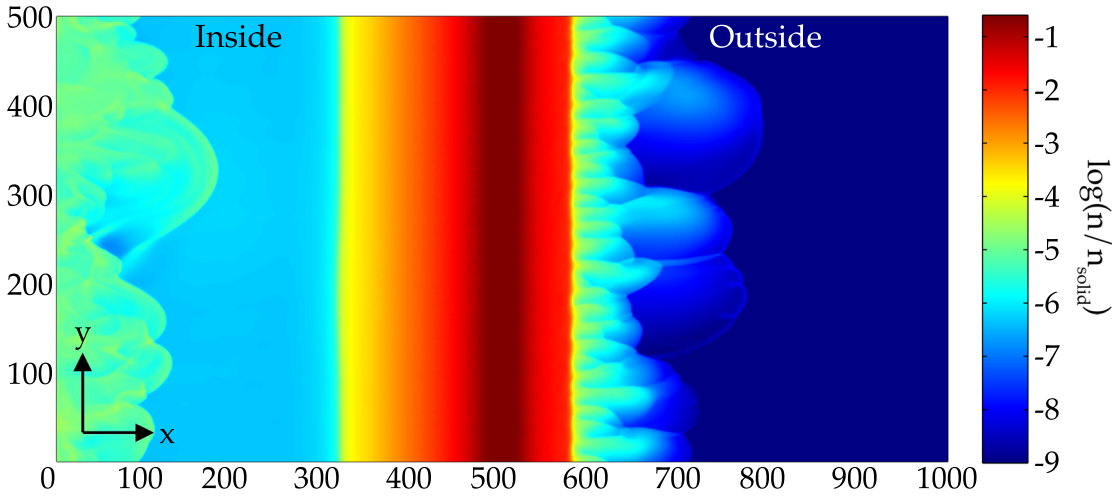

Figure 7.7: Mid time (50 ns) plot of plasma density, n, from Hall MHD simulation. The downward flow, v_y, developed in Fig. 7.6 is shear unstable and develops into the instability throughout the rest of the current pulse.

those out in the simulations, however.

As previously discussed, the 2D (xy) slab simulations eliminate the possibility of an m=0-like instability to develop. The electro-thermal instability, however, is a little more challenging. In my opinion, I have eliminated that possibility by using identical resistivity models. Additionally, I have tried seeding a ±20% thermal perturbation (as opposed to the density perturbation in the simulations presented above). After these attempts, there were still some questions as to whether or not the grid size is fine enough to resolve the electrothermal instability. At present, 1 micron grids are the smallest I have simulated. The 1000x500 simulations presented above each took about a week to run and I am not interested in running at a finer resolution. This could be something to look into with a more powerful simulation computer. However, even if the electrothermal instability is the cause of the instability in the experiments, it is still interesting and useful to identify issues that resistive MHD codes are unable to

produce.

Finally, just because the Hall MHD simulations qualitatively reproduce a similar instability that is seen in experiments, it does not mean that is the cause of the real (experimentally observed) instability. Unfortunately, however, micron-scale resolution of all of the plasma properties and field strengths is not available in experiments so pinning down the exact cause of the instability is extremely challenging.

7.5 Addendum

After the work in this chapter was completed, further simulations were performed using the full XMHD formulation, including electron pressure (i.e. Eq. 7.2). In these simulations, the electron pressure term tends to counteract the Hall term, which reduces the shear flow. A similar instability still exists in these XMHD simulations, but the origin is not as simple as with the Hall MHD case. This is further evidence that the physics missing in resistive MHD codes with respect to XMHD codes (i.e. Hall effect and electron pressure) can have important consequences in Z-pinch studies.

CHAPTER 8

CONCLUSIONS

Liners have become an attractive load design for both alternative fusion concepts (MagLIF) and for general Z-pinch studies. The reason for this is that their mass is easily scalable with larger current drivers and for the potential benefits that a continuous metal shell has over discrete wires. However, until recently, solid liners have remained relatively unstudied by the fast Z-pinch community. For this reason, it was decided to investigate the early stage developments (initiation, ablation and precursor formation, and instability analysis) of solid liner Z-pinches on COBRA.

For the initiation experiments presented in Ch. 4, it was found that thinner liners initiated sooner, more quickly, and more uniformly than thicker liners. This correlated well with both an increase in instantaneous dJ/dt at the time of first emission as well as the inductive voltage at the time of first emission. This result is in contrast to Awe's magnetic field threshold [57] and Chaikovsky's action integral studies[58]. Uniform initiation is important for liners because nonuniformities could lead to enhanced instabilities and poor liner performance (compression, x-ray production, etc.). For this reason, it would be worthwhile for future experiments to try to separate the dJ/dt and inductive voltage effects to see if one is more dominant than the other (while also keeping an eye on magnetic field strength and the total energy deposited into the liner).

The r-θ density maps and radial mass profiles of wire-arrays and liners presented in Ch. 6 show strong differences in their ablation and precursor formation stages. Wire-arrays develop complex, azimuthally varying ablation structures that lead to dense precursor formations. Liners, however, show signifi-

cantly reduced and azimuthally uniform ablation leading to an order of magnitude less dense precursor on axis. This is likely due to the discrete versus continuous nature of wire-arrays versus liners. With wire-arrays, plasma that is created on the outside of the wires can reach the array axis by being swept through the gaps between the stationary wire cores. In contrast, liners have no "gaps" for plasma to flow through. Therefore, any plasma that is created on the outside of the liner is trapped there until the bulk of the liner moves with the implosion. Consequently, only the plasma that is created on the inside of the liner is able to contribute to precursor formation. This is an important result because reduced precursor formation is important for fuel compression and heating in MagLIF. Less precursor can also lead to enhanced x-ray production because there is less mass on axis to cushion the conversion of kinetic energy into x-rays during the implosion/stagnation phases. Neither of these conclusions have been conclusively tested because we were unable to drive the liners in these experiments to implosion. This would make for a very interesting study on a larger machine capable of driving such liners to implosion.

Finally, in the experiments presented in Ch. 7, it was observed that liners develop a much larger amplitude instability on their outside surface as compared to wire-arrays. This is an important discovery and could be detrimental to liner performance (compression, x-ray production, etc.) because it could lead to enhanced magnetic Rayleigh-Taylor (MRT) instability during the implosion phase. Again, this consequence is still untested because COBRA is incapable of driving these liners to implosion. It would be interesting to see how the potential benefits of a lower precursor mass counterbalance the potential hindrance of enhanced instabilities.

A possible source of the enhanced instability was found using 2D (xy) PERSEUS simulations comparing the results of MHD and Hall MHD simulations. The instability only developed in the Hall MHD case. The 2D nature of the simulation, along with all other simulation parameters being equal between the two cases, rules out the possibility of MRT or m=0 for the cause of the instability (in the simulation). It was found that the Hall term was responsible for causing a shear-flow instability that developed later in time to resemble the experimental results. Finding the exact cause of the experimentally observed instability remains a difficult prospect.

As is often the case in science, it seems these studies have produced many questions and a few answers.

APPENDIX A

AXIAL X-RAY BACKLIGHTING OF WIRE ARRAY Z-PINCHES USING X PINCHES

Axial x-ray backlighting of wire-array Z-pinches using X pinches

I. C. Blesener,[a] J. B. Greenly, S. A. Pikuz, T. A. Shelkovenko, S. Vishniakou, D. A. Hammer, and B. R. Kusse
Laboratory of Plasma Studies, Cornell University, 439 Rhodes Hall, Ithaca, New York 14853, USA

(Received 17 September 2009; accepted 13 November 2009; published online 23 December 2009)

For the first time, a geometry has been developed to allow for an axial imaging system for wire-array Z-pinch experiments that produce high-resolution x-ray images. The new geometry required a significant redesign of the electrode hardware. Calibrated areal density measurements of the Z-pinch plasma including wire cores, coronal plasma, streaming plasma, and the precursor were obtained. The system used eight-wire molybdenum (Mo) X pinches in series with and directly below the Z-pinch axis to provide micron-scale x-rays sources for point-projection radiography. The images formed on the x-ray sensitive film had a 15 mm diameter field of view at the center height of the array and a magnification of about 7.5:1. Titanium (Ti) filters in front of the film transmitted radiation in the spectral range of 3–5 keV. For calibration, a separate film with the same thickness Ti filter was placed the same distance from the X pinch. This film had an unobstructed path that bypasses the Z-pinch but included step wedges for calibration of the Z-pinch plasma. The step wedges had thicknesses of tungsten (W) ranging from 0.015 to 1.1 μm to obtain areal density measurements of the W plasma from the wire-array. Images had subnanosecond temporal resolution and about 10 μm spatial resolution. © *2009 American Institute of Physics.*
[doi:10.1063/1.3271388]

I. INTRODUCTION

Wire-array Z-pinches are of great interest to the scientific community due to the high efficiency with which they generate >100 TW x-ray pulses. Such x-ray sources have many applications, including inertial confinement fusion,[1] laboratory astrophysics,[2] high energy density physics,[1] and radiation science.[3]

The Cornell Beam Research Accelerator (COBRA) (Ref. 4) is a nominal 1 MA and 100 ns zero-to-peak risetime pulsed-power generator that drives wire-array Z-pinches. Current from the driver is passed through a cylindrical array of wires (typically 8–32 wires having array diameters ranging from 6 to 16 mm and heights from 8 to 20 mm), which vaporize and form plasma. The global magnetic field of the wire-array causes the plasma to be swept toward the array axis. Once most of the mass reaches the axis, the resulting hot dense plasma emits an intense soft x-ray pulse. Experiments have shown that COBRA can convert electrical energy to x rays with ~10% efficiency.[5]

Side-on x-ray backlighting diagnostics for wire-array Z-pinches using X pinches[6–11] or laser-produced soft x-ray sources have been used on university level experiments as well as on larger facilities such as the Z machine at Sandia National Laboratories.[12] X pinches are favorable for university-scale experiments because of the lower cost compared to laser-produced soft x-ray sources. An X pinch consists of two or more wires crossed at a single point and driven by a high current pulsed-power generator.[13] At the crosspoint, a small (micron-scale) and short-lived (<1 ns) soft x-ray source is created.[14] This source can be used for point-projection x-ray backlighting.[15]

Here, we introduce a new X pinch backlighting geometry that allowed axial (end-on) x-ray backlighting of Z-pinches to complement laser shadowgraphy/interferometry and self-emission diagnostics. This new geometry required a redesign of the electrode hardware, the details of which are described in the next section. X-ray backlighting is required because of the high density plasmas ($>10^{20}$/cc ion density) involved. X-ray backlighting is also the only diagnostic that is directly sensitive to mass density. This system enabled calibrated high-resolution measurements of the plasma areal density profile throughout the entire volume of a small diameter (<15 mm) wire-array Z-pinch.

Unlike side-on imaging, which produces r-z projections, axial backlighting produces time resolved r-θ images. Having two separate orthogonal views is useful because each view contains information the other cannot produce. For instance, r-θ profiles contain densities and azimuthal widths of the plasma streaming toward the array axis, neither of which can be obtained from side-on images. Axial backlighting is also useful for loads where side-on imaging is difficult or impossible, such as cylindrical thin foil Z-pinches. Finally, axially averaged r-θ profiles are also more easily compared with two-dimensional simulations than cord averaged r-z projections. Below, we describe the experimental setup, present sample images, and discuss accuracy and error.

II. EXPERIMENTAL SETUP

This new axial x-ray backlighting system uses X pinch point-projection imaging in conjunction with step wedge at-

[a]Electronic mail: icb3@cornell.edu.

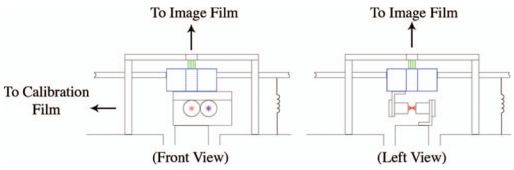

FIG. 1. (Color) Front and left views of hardware showing imaging X pinch (red), auxiliary X pinch (purple), intermediate electrode (blue), and array (green). The intermediate electrode is inductively isolated from ground. 120 μm of polypropylene and 12.5 μm Ti filters (not shown) were placed in the path between the imaging X pinch and the two films.

tenuators to produce high-resolution radiographs with calibrated mass density. Two X pinches (in parallel) are placed in series with and below a wire-array Z-pinch such that the crosspoint of one of the X pinches (called the imaging X pinch) is centered on the Z-pinch axis, while the other X pinch (called the auxiliary X pinch) is off-axis, as shown in Fig. 1. The purpose of the auxiliary X pinch is to provide a path for current to flow after the imaging X pinch has pinched. The auxiliary X pinch also had the effect of reducing the amount of current in each X pinch by a factor of two. This allowed lighter X pinches to be used, which typically result in better temporal and spatial resolution.[14] The resulting images had a field of view of 15 mm diameter with about 7.5× magnification at the center of the array height. Images had subnanosecond temporal resolution because of the short duration of the X pinch burst.[14]

Due to the added complexity to the electrode geometry, steps were taken wherever possible to minimize load inductance. It was necessary to increase the anode-cathode vertical separation from 2 to 8.5 cm to accommodate the X pinches in series with the Z-pinch. Also, the return current radius was increased from 4.4 to 6.7 cm. Six return current paths were used in place of four to offset some of the added inductance. The bulk of the added path lengths was solid conductors, and the high inductance wire loads were made as least inductive as possible. The Z-pinch height was reduced from 2 to 1 cm, which also helps minimize geometry-related errors that are discussed later. Two X pinches were used instead of one. This had the effect of not only minimizing the initial inductance but also of minimizing the time-dependance inductance caused when the imaging X pinch necks down to a very small current channel during pinching. The overall impact on the current drive of the generator was a change from 1 to 0.8 MA on a 100 ns risetime pulse. There was no detectable inductive dip in the current trace during the pinching of the imaging X pinch.

The X pinches used for these experiments consisted of eight Mo wires (imaging X pinch: 25–35 μm; auxiliary X pinch: 50 μm), which produced micron-scale high-intensity 3–5 keV point sources when they pinched. A 12.5 μm Ti foil in front of the x-ray sensitive film acted as the main x-ray filter to block broadband radiation below 2.5 keV as well as the intense Mo spectral lines near 2.5 keV. A 120 μm polypropylene filter was placed in front of the Ti filter to act as a shield to prevent energetic electrons from reaching the film. In this setup, the auxiliary X pinch was deliberately overmassed so that it did not pinch and radiate in the 3–5 keV band that was used for imaging. It was important to have only a single radiation source in the 3–5 keV band so that the exposure on the film could be calibrated as described below. For this reason, the Z-pinch itself was overmassed so that it would not radiate above 3 keV.

Diffraction limited spatial resolution provides a best-case scenario for the image resolution of our system and is determined by

$$\delta_{xd} = \sqrt{\frac{\lambda a b}{b+a}}, \tag{1}$$

where δ_{xd} is the diffraction limited spatial resolution in microns, λ is the wavelength of incident radiation in angstroms, a is the distance from source to object in centimeters, and b is the distance from object to detector in centimeters. For this setup, the wavelength of incident radiation (peak of the Ti transmission window) was 2.5 Å, the distance from the source to the center of the object was 3.1 cm, and the distance from the center of the Z-pinch to the film was 23.3 cm. This leads to a diffraction limited spatial resolution of about 3 μm.

Geometric spatial resolution is determined by

$$\delta_{xg} = \Phi \frac{b}{b+a}, \tag{2}$$

where δ_{xg} is the geometry limited spatial resolution, Φ is the spot size of the source, and a and b are the same as above. Source size measurements of multiwire 0.5 MA X pinches with 100 ns risetimes is limited. Extensive studies of Mo X pinches at 0.5 MA and 50 ns risetimes indicate source sizes of approximately 1 μm.[16] Similar studies of Mo X pinches at 1 MA and 100 ns risetimes indicate source sizes of approximately 40 μm.[17] The source size of the X pinches used in these experiments was likely somewhere between the two cited numbers. The sharp boundaries of the 25 μm W reference wires, for example, in Fig. 3, imply that the source was small compared to the wires (i.e., <25 μm). The overall resolution of the system is estimated to be less than 10 μm. However, because the Z-pinch was 1 cm tall and the resulting image was essentially an integration of absorption through that height, few, if any, features of that size exist in the images.

The timing of the backlighter can be roughly controlled by varying the mass of the X pinch. A given diameter of wire will produce generally repeatable timing within ±5 ns for a standard current pulse. The X pinch timing was monitored using an IRD AXUVHS1 silicon x-ray sensitive photodiode. The silicon diode was biased with 40 V and filtered with the same 12.5 μm Ti as the films. The X pinch continuum radiation has been measured by an x-ray streak camera to last less than 150 ps,[18] which determines the temporal resolution of the images. The silicon diodes, however, have a turn-on time of 250 ps. The timing signals were acquired at a rate of 200 ps/point, and cable delays were measured with an accuracy of about 500 ps. Therefore, the timing of each image was accurate to about 500 ps.

By comparing the film exposure caused by x-rays that passed through the tungsten (W) Z-pinch plasma to the film

exposure that resulted from the x-rays passing through W steps of known thicknesses, plasma areal densities can be measured.[15] The W steps had a clear line of sight to the point x-ray source and had step thicknesses of 150, 300, 750, 1500, 3000, 5000, and 10 000 Å. These steps were manufactured by magnetron sputtering W directly onto the 12.5 μm Ti x-ray filters. The actual thickness was then inferred by measuring the thickness of a "witness" sample after each sputtering run. In addition, the thickness was measured with an accuracy of about 100 Å by a profilometer. These step wedges and film were placed off to the side of the X pinch at the same distance and with the same filtering as the film that records the Z-pinch image, as shown in Fig. 1.

Various assumptions were made in order to use these step wedges to calculate areal densities of the Z-pinch plasma. One correction that was not made is the difference in opacity due to the temperature difference between the hot plasma and the cold step wedges. Previous experiments have shown that this is not a problem for W when imaged with 3–5 keV x-rays.[8] Another assumption was that the imaging X pinch radiation was azimuthally isotropic and was the only source of 3–5 keV x-rays. Care was taken to make sure the auxiliary X pinch and the Z-pinch itself did not emit x-rays above the 3 keV range. This was simply done by overmassing them so they would not pinch. Other methods exist to prevent x-rays from an imploding Z-pinch from reaching the films, but they have not been tested in this geometry. Instead of overmassing the Z-pinch, it may be possible to shield the films from the radiating areas[19] or to prevent radiation by quenching the central column with a large monofilament.[8] However, nothing can be done to completely block scattered radiation from reaching the films, which can produce nonuniform exposure.

As mentioned above, it was important for the same intensity of radiation to be present at both the imaging film and the calibration film. To make sure this was the case, several null tests were performed with no Z-pinch in the load region, just a hollow short circuit. In this way, both films had nothing directly in the path of the x-rays and should show the same level of background radiation. Histograms of each film showed that the 16-bit black levels of the background exposure are within 10% of each other, as shown in Fig. 2. The indicated region shown in Fig. 2(a) was selected to avoid the region of the film with the fiducial wires that happen to be barely visible due to the low contrast of the image but would have skewed the results.

III. SAMPLE IMAGES

Images were taken of three different wire-array materials (aluminum, copper, and tungsten), two different array diameters (8 and 16 mm), and four different wire numbers (4, 8, 16, and 32). Figure 3 shows an analysis of a wire-array that consisted of eight 25 μm W wires on an 8 mm diameter. This image was taken 80 ns into a 125 ns zero-to-peak 1 MA current pulse. The volumetric densities quoted were calculated assuming a uniform density along the entire 1 cm height of the array. Because the absorption is through the entire height of the array, low density plasma features (e.g., the ablation streams near the precursor) of a few $\times 10^{16}$/cc ion density can be resolved. The two thin lines crossing perpendicular to each other in Fig. 3 are 25 μm wires at 2:1 magnification, which were used as a reference for determining the quality of the X pinch source.

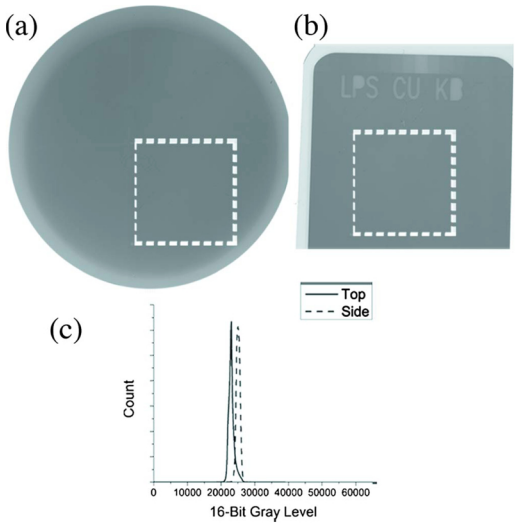

FIG. 2. (Color online) Histogram analysis. (a) Top image with indicated histogram area, (b) side image with step wedges and indicated histogram area, and (c) histograms showing the top film (solid) at 22 900 ± 600 and side (dashed) at 25 000 ± 600.

IV. ACCURACY AND ERROR

Several factors can lead to error associated with these measurements. Error can be introduced by radiation in the 3–5 keV passband of the Ti filter from the object or the auxiliary X pinch, film developing nonuniformities, multiple x-ray bursts from the imaging X pinch, energetic electrons, scattered 3–5 keV radiation from the imaging X pinch, conversion from areal to volumetric densities, and $1/R^2$ intensity variation.

When the object or the auxiliary X pinch produce radiation in the passband of the Ti filter, the resulting images cannot be calibrated. In experiments performed to date with this setup, the object (Z-pinch) has never produced any problematic radiation because it was significantly overmassed for the driver. In one instance, the auxiliary X pinch radiated and produced an image of the imaging X pinch on the calibration film. That shot was unusable and subsequent shots used a heavier (50 μm instead of 40 μm Mo) auxiliary X pinch.

The large size of the films used in these experiments creates the problem that different portions of the same film or the two separate films themselves may develop at different rates. Each imaging film, along with its calibration film, was developed at the same time and in the same developer bath. If films were not developed properly, they could show cloudiness or unnatural unevenness. To remove all develop-

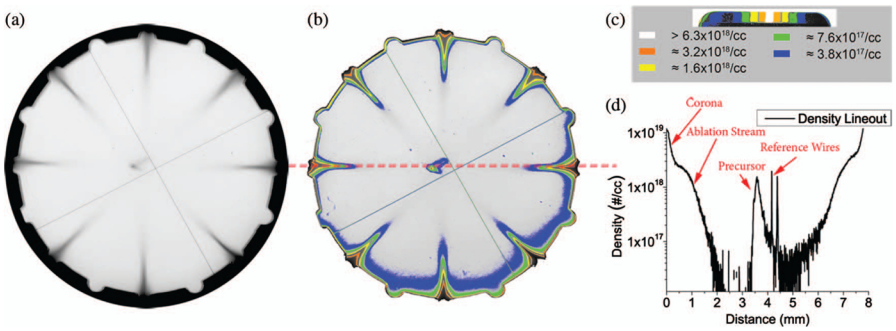

FIG. 3. (Color) Analysis of eight-wire, 25 μm W, and 8 mm diameter array. Image was taken 80 ns into a 125 ns zero-to-peak 1 MA current pulse. (a) Original film. (b) False-color image showing density isocontours corresponding to step wedges shown in (c). (d) Calibrated lineout of image at the location of the dashed red line. Densities above the thickest step wedge and below the thinnest are extrapolated.

ing related aberrations, the films were constantly agitated in developer that was diluted so that the films fully developed in approximately 5 min.

The most common problem in analyzing the images came from multiple x-ray sources in the imaging X pinch. When the multiple source was of comparable intensity, an overestimation of the mass in the plasma occurred. This error was as much as 50%–100% due to the overlapping of plasma features.[8] This error typically occurs in roughly 50% of Mo X pinches.[7] In these experiments, it occurred in roughly 65% of the experiments. The higher failure rate was likely due to the unusual geometry and relatively higher mass X pinches than are typically used. With more experiments and fine-tuning of the X pinches, the failure rate should be closer to the 50% mark, which, although better, is still far from ideal. Another solution, as described by Shelkovenko *et al.*,[20] is to use a nested X pinch geometry that allows for a tighter and more predictable and symmetric crosspoint.

Energetic electrons have been a problem with calibrating the exposure of the films. Initially, during null test shots (with no Z-pinch, just a hollow short circuit), the top image film was being completely saturated. It was determined that energetic electrons were the source of the exposure. The problem was solved by placing 120 μm of polypropylene between the top of the load and the film. The polypropylene was sufficient to block the electrons but lets the x-rays pass with minimal attenuation. The same thickness polypropylene was also placed between the imaging X pinch and the calibration film to keep filtering the same.

Scattered radiation was a common problem but resulted in less dramatic errors. Scattered x-rays have the effect of making all objects in the image appear less opaque. This is clearly seen when there is a large opaque object (e.g., 1/4 in. of steel or a few 100 μm of lead) that appears to have some transmission "through" it. This results in a significant underestimation in the amount of mass present at the highest areal densities. This effect can be seen to some extent in every image.

The conversion from areal to volumetric densities can introduce errors. The Z-pinches used in these experiments were 1 cm tall, so exposure on the film is essentially an integration of attenuation along the length of the Z-pinch. Only the axially averaged volumetric density can be inferred from the areal density. Additionally, because the x-ray source diverges, there exists a path length difference between the center of the Z-pinch and the perimeter. This difference in path length is less than 1%.

Although the overall path length of a ray that goes through the edge of the array compared to one that goes through the center is nearly identical, the radial spread of each ray is very different. With the geometry used in these experiments, at the edge of the array, a single ray sampled radially over approximately 1 mm. Halfway to the edge of the array, a single ray sampled over approximately 0.5 mm. This radial averaging linearly decreases until the center of the array where the radial averaging is zero. This caused problems where there were large radial density gradients along the path of a ray. At the edge of the array, such density gradients existed and the averaging resulted in recorded densities that were much lower than the actual densities in the array. For example, the highest density regions of the film in Fig. 3 are approximately 1×10^{19}/cc ion density. These regions are known to be greater than 10^{20}/cc ion density for similar arrays in other experiments. This indicates that the density around the perimeter of the array is underestimated by at least an order of magnitude. This error at the edge of the array can be minimized by increasing the distance from the X pinch to the object and by decreasing the thickness of the object but can never be totally eliminated.

Finally, radiation from a point source onto a flat film will introduce $1/R^2$ effects. For the geometry of these experiments, the R^2 difference from the center of the imaging plane to the edge of the array on the imaging plane was approximately 1% and was therefore negligible.

V. CONCLUSION

The axial radiography system is a new diagnostic and a very useful tool that supplements previously existing diagnostics. The unusual geometry, unique to axial X pinch imaging, required a significant redesign of the electrode hardware. The added hardware increased the inductance of the power feed but had only minor effects on the generator performance. This imaging system has a large field of view, can

penetrate the dense precursor and streams of wire-array Z-pinches, and can reliably calibrate the areal density of the plasma at the center of an array.

This geometry for axial X pinch imaging to produce r-θ radiographs could be implemented on any pulsed-power machine with sufficient current and risetime for X pinches. This diagnostic would also be very useful for imaging cylindrical thin foil Z-pinches where transverse imaging is difficult if not impossible.

ACKNOWLEDGMENTS

The authors would like to thank several individuals for their valuable contributions. Kate S. Blesener manufactured and measured the W step wedges at the Cornell Nanofabrication Facility; without her work, calibrating the images would not have been possible. Harry Wilhelm and J. Todd Blanchard, technicians at the Laboratory of Plasma Studies, contributed immensely in the operation and maintenance of COBRA as well as in the fabrication of the specialized hardware used in these experiments. The described procedure of using step wedges to calibrate X pinch radiographs was heavily influenced by the procedure developed by Jon D. Douglass.

This research was supported by the Stewardship Sciences Academic Alliances program of the National Nuclear Security Administration under DOE Cooperative Agreement No. DE-FC03-02NA00057.

[1] M. K. Matzen, M. A. Sweeney, R. G. Adams, J. R. Asay, J. E. Bailey, G. R. Bennett, D. E. Bliss, D. D. Bloomquist, T. A. Brunner, R. B. Campbell, G. A. Chandler, C. A. Coverdale, M. E. Cuneo, J. P. Davis, C. Deeney, M. P. Desjarlais, G. L. Donovan, C. J. Garasi, T. A. Haill, C. A. Hall, D. L. Hanson, M. J. Hurst, B. Jones, M. D. Knudson, R. J. Leeper, R. W. Lemke, M. G. Mazarakis, D. H. McDaniel, T. A. Mehlhorn, T. J. Nash, C. L. Olson, J. L. Porter, P. K. Rambo, S. E. Rosenthal, G. A. Rochau, L. E. Ruggles, C. L. Ruiz, T. W. L. Sanford, J. F. Seamen, D. B. Sinars, S. A. Slutz, I. C. Smith, K. W. Struve, W. A. Stygar, R. A. Vesey, E. A. Weinbrecht, D. F. Wenger, and E. P. Yu, Phys. Plasmas **12**, 055503 (2005).

[2] B. A. Remington, R. P. Drake, and D. D. Ryutov, Rev. Mod. Phys. **78**, 755 (2006).

[3] J. E. Bailey, G. A. Chandler, D. Cohen, M. E. Cuneo, M. E. Foord, R. F. Heeter, D. Jobe, P. W. Lake, J. J. MacFarlane, T. J. Nash, D. S. Nielson, R. Smelser, and J. Torres, Phys. Plasmas **9**, 2186 (2002).

[4] J. B. Greenly, J. D. Douglas, D. A. Hammer, B. R. Kusse, S. C. Glidden, and H. D. Sanders, Rev. Sci. Instrum. **79**, 073501 (2008).

[5] R. D. McBride, T. A. Shelkovenko, S. A. Pikuz, D. A. Hammer, J. B. Greenly, B. R. Kusse, J. D. Douglass, P. F. Knapp, K. S. Bell, I. C. Blesener, and D. A. Chalenski, Phys. Plasmas **16**, 012706 (2009).

[6] D. H. Kalantar and D. A. Hammer, Rev. Sci. Instrum. **66**, 779 (1995).

[7] J. D. Douglass, S. A. Pikuz, T. A. Shelkovenko, D. A. Hammer, S. N. Bland, S. C. Bott, and R. D. McBride, Phys. Plasmas **14**, 012704 (2007).

[8] J. D. Douglass and D. A. Hammer, Rev. Sci. Instrum. **79**, 033503 (2008).

[9] S. V. Lebedev, F. N. Beg, S. N. Bland, J. P. Chittenden, A. E. Dangor, M. G. Haines, K. H. Kwek, S. A. Pikuz, and T. A. Shelkovenko, Phys. Plasmas **8**, 3734 (2001).

[10] V. Alexandrov, I. Frolov, M. Fedulov, E. Grabovsky, K. Mitrofanov, S. Nedoseev, G. Oleinik, I. Porofeev, A. Samokhin, P. Sasorov, V. Smirnov, G. Volkov, M. Zurin, and G. Zukakischvili, IEEE Trans. Plasma Sci. **30**, 559 (2002).

[11] E. V. Grabovskii, K. N. Mitrofanov, G. M. Oleinik, and I. Y. Porofeev, Plasma Phys. Rep. **30**, 121 (2004).

[12] D. B. Sinars, G. R. Bennett, D. F. Wenger, M. E. Cuneo, D. L. Hanson, J. L. Porter, R. G. Adams, P. K. Rambo, D. C. Rovang, and I. C. Smith, Rev. Sci. Instrum. **75**, 3672 (2004).

[13] S. Zakharov, G. Ivanenkov, A. Kolomenskij, S. Pikuz, A. Samokhin, and I. Ulshmid, Sov. Tech. Phys. Lett. **8**, 456 (1982).

[14] D. B. Sinars, S. A. Pikuz, T. A. Shelkovenko, K. M. Chandler, and D. A. Hammer, Rev. Sci. Instrum. **72**, 2948 (2001).

[15] S. A. Pikuz, T. A. Shelkovenko, A. R. Mingaleev, D. A. Hammer, and H. P. Neves, Phys. Plasmas **6**, 4272 (1999).

[16] B. M. Song, S. A. Pikuz, T. A. Shelkovenko, and D. A. Hammer, Appl. Opt. **44**, 2349 (2005).

[17] D. B. Sinars, S. A. Pikuz, J. D. Douglass, R. D. McBride, D. J. Ampleford, P. F. Knapp, K. Bell, D. Chalenski, M. E. Cuneo, J. B. Greenly, D. A. Hammer, B. R. Kusse, A. Mingaleev, T. A. Shelkovenko, and D. F. Wenger, Phys. Plasmas **15**, 092703 (2008).

[18] T. A. Shelkovenko, S. A. Pikuz, D. B. Sinars, K. M. Chandler, and D. A. Hammer, Phys. Plasmas **9**, 2165 (2002).

[19] S. V. Lebedev, F. N. Beg, S. N. Bland, J. P. Chittenden, A. E. Dangor, M. G. Haines, M. Zakaullah, S. A. Pikuz, T. A. Shelkovenko, and D. A. Hammer, Rev. Sci. Instrum. **72**, 671 (2001).

[20] T. A. Shelkovenko, S. A. Pikuz, R. D. McBride, P. F. Knapp, H. Wilhelm, D. A. Hammer, and D. B. Sinars, Phys. Plasmas **16**, 050702 (2009).

APPENDIX B

LINER DATA SHEETS FROM GENERAL ATOMICS

ORIGINATOR: E. GIRALDEZ

COMPONENT SHIPMENT DATA

ORDER #: CPM-Cornell Thin Foils-11A Copper Tubes

SPECIFICATION: Mandrel for Foils

CUSTOMER: LLNL

WebTRF: 728

DATE: 10/1/10

PAGE: 1 of 1

PART ID	SPECS.	#1-3	#2-3	#1-6	#2-6	#3-6	#4-6	#5-6	#6-6	#7-6	#8-6		
Top Flange Diameter (mm)	8.000 ± 0.200	7.999	7.999	7.996	8.000	8.002	8.003	8.000	8.000	7.998	8.000		
Spool Diameter (mm)	4.000 ± 0.030	3.999	4.000	3.997	3.999	3.998	4.000	4.001	4.000	3.999	4.000		
Bottom Flange Diameter (mm)	12.000 ± 0.200	11.999	11.999	11.997	12.001	11.999	12.000	12.001	12.001	11.999	12.001		
Spool Length (mm)	12.000 ± 0.200	12.022	12.015	12.022	12.006	12.021	12.023	12.013	12.007	12.017	12.017		
Hole Diamter (mm)	2.000 ± 0.200	2.020	2.020	2.020	2.020	2.020	2.020	2.020	2.020	2.020	2.020		
Top Flange Thickness (mm)	1.000 ± 0.200	0.970	1.002	1.002	0.998	1.006	1.002	1.009	1.001	0.999	0.998		
Bottom Flange Thickness (mm)	1.000 ± 0.200	1.033	1.018	1.015	1.029	1.010	1.012	1.014	1.024	1.024	1.016		
Chamfer Thickness (mm)	2.000 ± 0.200	1.972	1.975	1.980	1.980	1.982	1.963	1.970	1.989	1.972	1.964		
Copper Thickness (µm)	3.0 ± 1.0	2.1	3.3										
Copper Thickness (µm)	6.0 ± 1.0			8.9	5.3	5.1	6.0	5.4	5.0	5.0	5.3		

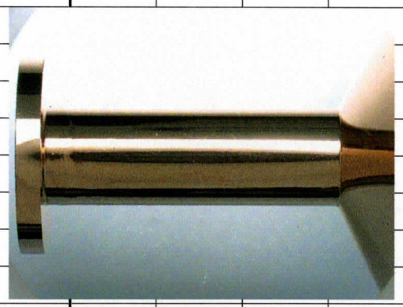

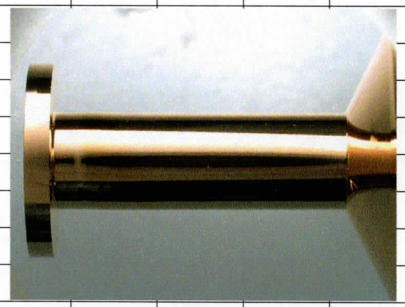

			#1-3							#1-6			

COMMENTS:

GENERAL ATOMICS

ORIGINATOR: E. GIRALDEZ

COMPONENT SHIPMENT DATA

ORDER #: CPM-Cornell Thin Foils-11B Copper Tubes

SPECIFICATION: Mandrel for Foils

CUSTOMER: LLNL

WebTRF: 728

DATE: 10/26/10

PAGE: 1 of 1

PART ID	SPECS.	#2	#4	#6
Top Flange Diameter (mm)	8.000 ± 0.200	8.001	8.000	8.004
Spool Diameter (mm)	4.000 ± 0.030	4.001	4.000	4.004
Bottom Flange Diameter (mm)	12.000 ± 0.200	12.001	11.999	12.004
Spool Length (mm)	12.000 ± 0.200	12.013	12.010	12.005
Hole Diamter (mm)	2.000 ± 0.200	2.100	2.100	2.100
Top Flange Thickness (mm)	1.000 ± 0.200	1.013	1.005	1.001
Bottom Flange Thickness (mm)	1.000 ± 0.200	1.006	1.004	1.019
Chamfer Thickness (mm)	2.000 ± 0.200	1.993	1.992	1.993
Copper Thickness at Spool (µm)	3.0 ± 1.0	4.3	2.5	4.3

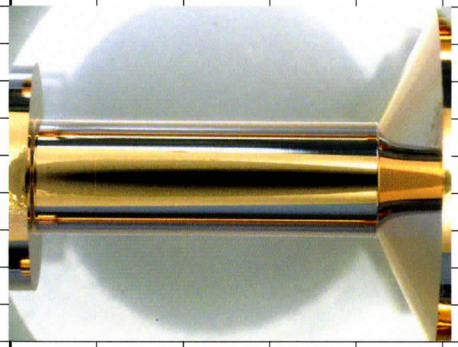

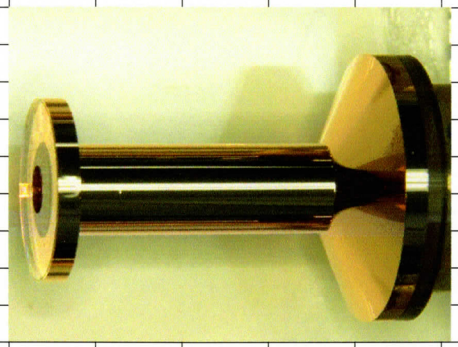

#2

COMMENTS:

GENERAL ATOMICS

ORIGINATOR: E. GIRALDEZ

COMPONENT SHIPMENT DATA

ORDER #: CPM-Cornell Thin Foils-11B Copper Tubes

SPECIFICATION: Mandrel for Foils

CUSTOMER: LLNL

WebTRF: 728

DATE: 10/26/10

PAGE: 1 of 1

PART ID	SPECS.	#1	#3	#5	#8	#10	#11	#12					
Top Flange Diameter (mm)	8.000 ± 0.200	8.001	8.002	7.997	8.003	8.001	8.000	7.999					
Spool Diameter (mm)	4.000 ± 0.030	4.000	4.002	3.997	4.003	4.000	3.999	4.000					
Bottom Flange Diameter (mm)	12.000 ± 0.200	12.000	12.002	11.997	12.005	12.001	12.000	12.000					
Spool Length (mm)	12.000 ± 0.200	12.001	12.005	12.007	12.018	12.014	12.012	12.001					
Hole Diamter (mm)	2.000 ± 0.200	2.100	2.100	2.100	2.100	2.100	2.100	2.100					
Top Flange Thickness (mm)	1.000 ± 0.200	1.005	1.009	1.008	1.015	1.008	1.007	1.004					
Bottom Flange Thickness (mm)	1.000 ± 0.200	1.007	0.994	1.012	1.007	1.009	1.000	1.017					
Chamfer Thickness (mm)	2.000 ± 0.200	1.992	1.996	1.992	1.995	1.989	1.997	1.992					
Copper Thickness at Spool (µm)	6.0 ± 1.0	6.3	6.4	7.3	6.6	6.7	6.0	6.9					

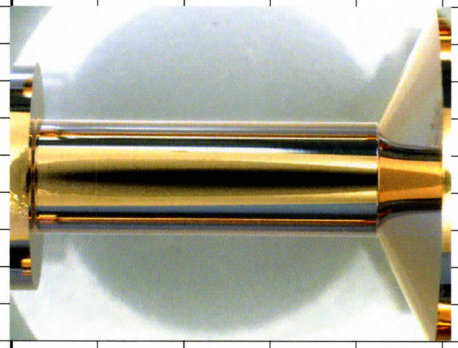

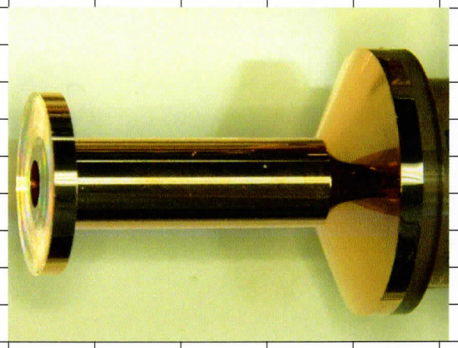

#1

COMMENTS:

GENERAL ATOMICS

ORIGINATOR: E. GIRALDEZ

COMPONENT SHIPMENT DATA

ORDER #: CPM-Cornell Thin Foils-11C Copper Tubes (1mic)

SPECIFICATION: Mandrel for Foils

CUSTOMER: LLNL

WebTRF: 728

DATE: 12/6/10

PART ID	SPECS.	2*	3*	9*	12*	15*							
Top Flange Diameter (mm)	8.000 ± 0.200	7.999	8.000	8.000	7.995	7.997							
Spool Diameter (mm)	4.000 ± 0.030	4.000	4.001	4.000	3.998	4.000							
Bottom Flange Diameter (mm)	12.000 ± 0.200	12.000	12.000	11.999	11.995	12.000		*	PEELING				
Spool Length (mm)	12.000 ± 0.200	12.013	11.981	12.020	12.011	12.010							
Hole Diameter (mm)	2.000 ± 0.200	2.156	2.156	2.156	2.156	2.156							
Top Flange Thickness (mm)	1.000 ± 0.200	1.003	1.006	0.992	1.008	1.003							
Bottom Flange Thickness (mm)	1.000 ± 0.200	0.978	1.023	0.998	0.978	0.978							
Chamfer Thickness (mm)	2.000 ± 0.200	1.983	1.982	1.978	1.960	1.983							
Copper Thickness at Spool (µm)	1.0 ± 0.5	1.2	1.3	1.6	1.8	0.6							

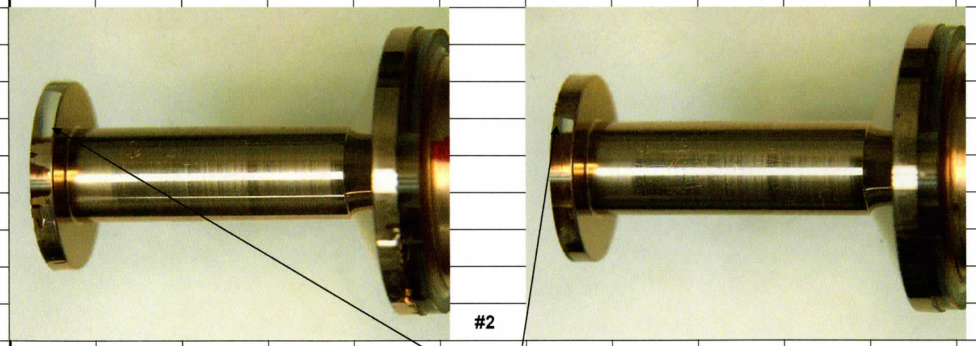

COMMENTS:

GENERAL ATOMICS

ORIGINATOR: E. GIRALDEZ

COMPONENT SHIPMENT DATA

ORDER #: CPM-Cornell Thin Foils-11C Copper Tubes (20 mic)

SPECIFICATION: Mandrel for Foils

CUSTOMER: LLNL

WebTRF: 728

DATE: 12/6/10

PAGE: 1 of 1

PART ID	SPECS.	1	5	6	7	13							
Top Flange Diameter (mm)	8.000 ± 0.200	8.000	7.999	8.001	7.999	8.000							
Spool Diameter (mm)	4.000 ± 0.030	4.000	3.999	4.000	4.000	4.000							
Bottom Flange Diameter (mm)	12.000 ± 0.200	12.000	12.000	11.999	11.999	11.999							
Spool Length (mm)	12.000 ± 0.200	11.995	11.987	11.984	11.977	11.986							
Hole Diameter (mm)	2.000 ± 0.200	2.156	2.156	2.156	2.156	2.156							
Top Flange Thickness (mm)	1.000 ± 0.200	1.032	1.026	1.028	1.022	1.008							
Bottom Flange Thickness (mm)	1.000 ± 0.200	0.974	0.988	0.954	0.983	0.983							
Chamfer Thickness (mm)	2.000 ± 0.200	1.982	1.986	1.982	1.983	1.986							
Copper Thickness at Spool (µm)	20.0 ± 1.0	23.0	20.2	23.5	21.7	20.5							

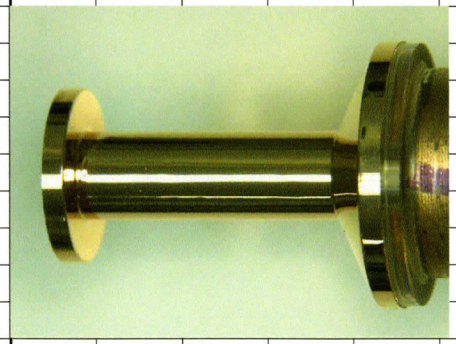

#1

COMMENTS:

GENERAL ATOMICS

APPENDIX C

DESCRIPTION OF LEACHING TECHNIQUE FOR THIN FOIL LINERS

Leaching the acrylic mandrel from the inside of the copper liners is both a simple and delicate process. Dissolving acrylic is as simple as submerging it in dichloromethane (DCM, a.k.a. methylene chloride). DCM, however, is a strong carcinogen and must be handled with care. Additionally, the copper liners can be extremely fragile once their acrylic support structure has been removed. Therefore, care must also be taken to minimize the amount of crinkling that occurs. In this appendix, I will discuss the procedure I developed to safely and carefully leach acrylic from the liners.

Because of the carcinogenic nature of DCM, it must be used inside of a proper fume hood. For this reason, I performed the leaching operation at Cornell's NanoScale Science & Technology Facility (CNF), but one could perform the procedure anywhere a fume hood and proper disposal protocols are followed.

The liners came from General Atomics (GA) with several inches of the acrylic mandrel sticking out from the cathode-side of the liners. In order to mount the liner (still on the mandrel) in the machine hardware, I first used a bandsaw to cut off most of the excess acrylic. Then, I mounted the liner-on-mandrel in the machine hardware and placed it upside down in a jig (see Fig. C.1(a)). At this point, there is still a large gap between the two cathode sections. The two cathode sections are held loosely in place by the adjustment bolts and the anode-cathode separation is held constant by the two support rods. The entire jig is then placed into a glass beaker (DCM will dissolve most plastics) that is taller than the jig.

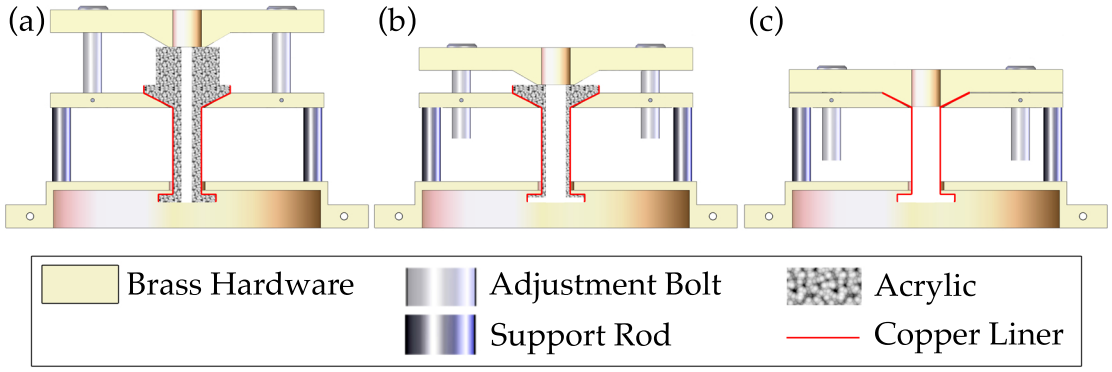

Figure C.1: Illustration of leaching process for removing acrylic mandrel from liners. (a) Initial position, (b) intermediate position, and (c) final position.

The glass beaker, with the jig inside, is then placed inside the fume hood and filled with approximately 250 mL of DCM (enough to cover all of the acrylic). At this point, the beaker should be covered to prevent evaporation of the DCM or any accidental spillage into or out of the beaker. For a cover, I used a disposable, stretchable paraffin membrane. After 30-45 minutes, most of the extra acrylic at the top of the jig should be dissolved. Gravity should have done its job to slide the top-most cathode piece closer to its matching set. If not, give it a light tap to help it slide down the adjustment bolts. Then, lightly tighten the adjustment bolts as indicated in Fig. C.1(b).

After about 2 hours have elapsed, all of the acrylic should be dissolved and once again, gravity should have slid the two cathode pieces into contact. Tighten all of the adjustment bolts so that the liner is firmly attached to the cathode (Fig. C.1(c)).

DCM must be disposed of separately from other chemicals. The approximately 250 mL of DCM is enough to dissolve multiple (5 or so) acrylic mandrels

before it becomes too saturated. DCM should be discarded with other halogens in the bottle marked "Halogens." Usually, the hardware and the liner will have a white residue left behind from the DCM/acrylic mixture. This should be rinsed off by submerging the entire jig in isopropanol and gently bobbing it up and down. The isopropanol/DCM mixture should also be dumped in with the halogens. Finally, the residual isopropanol can be rinsed off with deionized water and dumped down the drain.

Overall the process takes 2 or 3 hours, but it generally does not need to be constantly monitored. I usually had one liner leaching while another was in COBRA, pumping down and ready to fire. In this way, I was never waiting around for acrylic to dissolve.

BIBLIOGRAPHY

[1] C. Deeney, M. R. Douglas, R. B. Spielman, T. J. Nash, D. L. Peterson, P. L'Eplattenier, G. A. Chandler, J. F. Seamen, and K. W. Struve. Enhancement of x-ray power from a *Z* pinch using nested-wire arrays. *Phys. Rev. Lett.*, 81:4883–4886, Nov 1998.

[2] R. B. Spielman, C. Deeney, G. A. Chandler, M. R. Douglas, D. L. Fehl, M. K. Matzen, D. H. McDaniel, T. J. Nash, J. L. Porter, T. W. L. Sanford, J. F. Seamen, W. A. Stygar, K. W. Struve, S. P. Breeze, J. S. McGurn, J. A. Torres, D. M. Zagar, T. L. Gilliland, D. O. Jobe, J. L. McKenney, R. C. Mock, M. Vargas, T. Wagoner, and D. L. Peterson. Tungsten wire-array Z-pinch experiments at 200 TW and 2 MJ. *Phys. Plasmas*, 5:2105–2111, 1998.

[3] M. E. Cuneo, E. M. Waisman, S. V. Lebedev, J. P. Chittenden, W. A. Stygar, G. A. Chandler, R. A. Vesey, E. P. Yu, T. J. Nash, D. E. Bliss, G. S. Sarkisov, T. C. Wagoner, G. R. Bennett, D. B. Sinars, J. L. Porter, W. W. Simpson, L. E. Ruggles, D. F. Wenger, C. J. Garasi, B. V. Oliver, R A. Aragon, W. E. Fowler, M. C. Hettrick, G. C. Idzorek, D. Johnson, K. Keller, S. E. Lazier, J. S. McGurn, T. A. Mehlhorn, T. Moore, D. S. Nielsen, J. Pyle, S. Speas, K. W. Struve, and J. A. Torres. Characteristics and scaling of tungsten-wire-array *z*-pinch implosion dynamics at 20 MA. *Phys. Rev. E*, 71:046406, Apr 2005.

[4] T. J. Nash, M. S. Derzon, G. A. Chandler, R. Leeper, D. Fehl, J. Lash, C. Ruiz, G. Cooper, J. F. Seaman, J. McGurn, S. Lazier, J. Torres, D. Jobe, T. Gilliland, M. Hurst, R. Mock, P. Ryan, D. Nielsen, J. Armijo, J. McKenney, R. Hawn, D. Hebron, J. J. MacFarlane, D. Petersen, R. Bowers, W. Matuska, and D. D. Ryutov. High-temperature dynamic hohlraums on the pulsed power driver Z. *Phys. Plasmas*, 6:2023–2029, 1999.

[5] James H. Hammer, Max Tabak, Scott C. Wilks, John D. Lindl, David S. Bailey, Peter W. Rambo, Arthur Toor, George B. Zimmerman, and John L. Porter. High yield inertial confinement fusion target design for a z-pinch-driven hohlraum. *Phys. Plasmas*, 6:2129–2136, 1999.

[6] Michael E. Cuneo, Roger A. Vesey, John L. Porter, Gordon A. Chandler, David L. Fehl, Terrance L. Gilliland, David L. Hanson, John S. McGurn, Paul G. Reynolds, Laurence E. Ruggles, Hans Seamen, Rick B. Spielman, Ken W. Struve, William A. Stygar, Walter W. Simpson, Jose A. Torres, David F. Wenger, James H. Hammer, Peter W. Rambo, Darrell L. Peterson, and George C. Idzorek. Development and characterization of a Z-pinch-driven hohlraum high-yield inertial confinement fusion target concept. *Phys. Plasmas*, 8:2257–2267, 2001.

[7] S. A. Slutz, M. R. Douglas, J. S. Lash, R. A. Vesey, G. A. Chandler, T. J. Nash, and M. S. Derzon. Scaling and optimization of the radiation temperature in dynamic hohlraums. *Phys. Plasmas*, 8:1673–1691, 2001.

[8] J. E. Bailey, G. A. Chandler, S. A. Slutz, G. R. Bennett, G. Cooper, J. S. Lash, S. Lazier, R. Lemke, T. J. Nash, D. S. Nielsen, T. C. Moore, C. L. Ruiz, D. G. Schroen, R. Smelser, J. Torres, and R. A. Vesey. X-ray imaging measurements of capsule implosions driven by a Z-pinch dynamic hohlraum. *Phys. Rev. Lett.*, 89:095004, Aug 2002.

[9] R. A. Vesey, M. E. Cuneo, G. R. Bennett, J. L. Porter, R. G. Adams, R. A. Aragon, P. K. Rambo, L. E. Ruggles, W. W. Simpson, and I. C. Smith. Demonstration of radiation symmetry control for inertial confinement fusion in double Z-pinch hohlraums. *Phys. Rev. Lett.*, 90:035005, Jan 2003.

[10] M. Keith Matzen, M. A. Sweeney, R. G. Adams, J. R. Asay, J. E. Bailey, G. R. Bennett, D. E. Bliss, D. D. Bloomquist, T. A. Brunner, R. B. Campbell, G. A. Chandler, C. A. Coverdale, M. E. Cuneo, J.-P. Davis, C. Deeney, M. P. Desjarlais, G. L. Donovan, C. J. Garasi, T. A. Haill, C. A. Hall, D. L. Hanson, M. J. Hurst, B. Jones, M. D. Knudson, R. J. Leeper, R. W. Lemke, M. G. Mazarakis, D. H. McDaniel, T. A. Mehlhorn, T. J. Nash, C. L. Olson, J. L. Porter, P. K. Rambo, S. E. Rosenthal, G. A. Rochau, L. E. Ruggles, C. L. Ruiz, T. W. L. Sanford, J. F. Seamen, D. B. Sinars, S. A. Slutz, I. C. Smith, K. W. Struve, W. A. Stygar, R. A. Vesey, E. A. Weinbrecht, D. F. Wenger, and E. P. Yu. Pulsed-power-driven high energy density physics and inertial confinement fusion research. *Phys. Plasmas*, 12:055503, 2005.

[11] S. A. Slutz, M. C. Herrmann, R. A. Vesey, A. B. Sefkow, D. B. Sinars, D. C. Rovang, K. J. Peterson, and M. E. Cuneo. Pulsed-power-driven cylindrical liner implosions of laser preheated fuel magnetized with an axial field. *Phys. Plasmas*, 17:056303, 2010.

[12] D. D. Ryutov. Liner-on-plasma system near stagnation: Stabilizing effect of a magnetic cushion. *Phys. Plasmas*, 18:064509, 2011.

[13] M. Keith Matzen. Z pinches as intense x-ray sources for high-energy density physics applications. *Phys. Plasmas*, 4:1519–1527, 1997.

[14] D. D. Ryutov, M. S. Derzon, and M. K. Matzen. The physics of fast Z pinches. *Rev. Mod. Phys.*, 72:167–223, Jan 2000.

[15] R. F. Heeter, J. E. Bailey, M. E. Cuneo, J. Emig, M. E. Foord, P. T. Springer,

and R. S. Thoe. Plasma diagnostics for x-ray driven foils at Z. *Rev. Sci. Instrum.*, 72:1224–1227, 2001.

[16] S. V. Lebedev, J. P. Chittenden, F. N. Beg, S. N. Bland, A. Ciardi, D. Ampleford, S. Hughes, M. G. Haines, A. Frank, E. G. Blackman, and T. Gardiner. Laboratory astrophysics and collimated stellar outflows: The production of radiatively cooled hypersonic plasma jets. *Astrophys, J.*, 564(1):113, 2002.

[17] D. J. Ampleford, A. Ciardi, S. V. Lebedev, S. N. Bland, S. C. Bott, J. P. Chittenden, G. N. Hall, A. Frank, and E. Blackman. Jet deflection by a quasi-steady-state side wind in the laboratory. *Astrophys. Space Sci.*, 307:29–34, 2007.

[18] J. E. Bailey, G. A. Chandler, D. Cohen, M. E. Cuneo, M. E. Foord, R. F. Heeter, D. Jobe, P. W. Lake, J. J. MacFarlane, T. J. Nash, D. S. Nielson, R. Smelser, and J. Torres. Radiation science using Z-pinch x rays. *Phys. Plasmas*, 9:2186–2194, 2002.

[19] Peter J. Turchi and William L. Baker. Generation of high-energy plasmas by electromagnetic implosion. *J. Appl. Phys.*, 44:4936–4945, 1973.

[20] William L. Baker, Miles C. Clark, James H. Degnan, Gerald F. Kiuttu, Charles R. McClenahan, and Robert E. Reinovsky. Electromagnetic-implosion generation of pulsed high-energy-density plasma. *J. Appl. Phys.*, 49:4694–4706, 1978.

[21] R. B. Spielman, D. L. Hanson, M. A. Palmer, M. K. Matzen, T. W. Hussey, and J. M. Peek. Efficient x-ray production from ultrafast gas-puff Z pinches. *J. Appl. Phys.*, 57:830–833, 1985.

[22] M. Gersten, W. Clark, J. E. Rauch, G. M. Wilkinson, J. Katzenstein, R. D. Richardson, J. Davis, D. Duston, J. P. Apruzese, and R. Clark. Scaling of plasma temperature, density, size, and x-ray emission above 1 keV with array diameter and mass for aluminum imploding-wire plasmas. *Phys. Rev. A*, 33:477–484, Jan 1986.

[23] N. R. Pereira and J. Davis. X rays from z-pinches on relativistic electron-beam generators. *J. Appl. Phys.*, 64:R1–R27, 1988.

[24] C. Stallings, K. Nielsen, and R. Schneider. Multiple-wire array load for high-power pulsed generators. *Appl. Phys. Lett.*, 29:404–406, 1976.

[25] R. F. Benjamin, J. S. Pearlman, E. Y. Chu, and J. C. Riordan. Measurements of the dynamics of imploding wire arrays. *Appl. Phys. Lett.*, 39:848–850, 1981.

[26] J. Shiloh, A. Fisher, and N. Rostoker. Z pinch of a gas jet. *Phys. Rev. Lett.*, 40:515–518, Feb 1978.

[27] James H. Degnan, Robert E. Reinovsky, David L. Honea, and Roger D. Bengtson. Electromagnetic implosions of cylindrical gas "shells". *J. Appl. Phys.*, 52:6550–6561, 1981.

[28] T. W. L. Sanford, G. O. Allshouse, B. M. Marder, T. J. Nash, R. C. Mock, R. B. Spielman, J. F. Seamen, J. S. McGurn, D. Jobe, T. L. Gilliland, M. Vargas, K. W. Struve, W. A. Stygar, M. R. Douglas, M. K. Matzen, J. H. Hammer, J. S. De Groot, J. L. Eddleman, D. L. Peterson, D. Mosher, K. G. Whitney, J. W. Thornhill, P. E. Pulsifer, J. P. Apruzese, and Y. Maron. Improved symmetry greatly increases x-ray power from wire-array *Z*-pinches. *Phys. Rev. Lett.*, 77:5063–5066, Dec 1996.

[29] S. Wong, C. Gilman, P. Sincerny, and T. Young. A scaling law for k-line radiation in the imploding argon gas puff. *Proc. IEEE Conf. Plasma Sci.*, page 37, 1982.

[30] C. Deeney, T. Nash, R. R. Prasad, L. Warren, K. G. Whitney, J. W. Thornhill, and M. C. Coulter. Role of the implosion kinetic energy in determining the kilovolt x-ray emission from aluminum-wire-array implosions. *Phys. Rev. A*, 44:6762–6775, Nov 1991.

[31] W. H. Bennett. Magnetically self-focussing streams. *Phys. Rev.*, 45:890–897, Jun 1934.

[32] R. S. Pease. Equilibrium characteristics of a pinched gas discharge cooled by bremsstrahlung radiation. *Proc. Phys. Soc. B*, 70:11, 1957.

[33] S. I. Braginskiĭ. The behavior of a completely ionized plasma in a strong magnetic field. *Sov. Phys. JETP*, 6:494–501, 1958.

[34] S. Glasstone and R. H. Loveberg. *Controlled Thermonuclear Reaction*, chapter II. Van Nostrand, New York, 1960.

[35] Nino R. Pereira. A simple derivation of the Pease-Braginskiĭ current. *Phys. Plasmas*, 2:677–678, 1990.

[36] J.D. Douglass, J.B. Greenly, D.A. Hammer, B.R. Kusse, J.T. Blanchard, L.M. Maxson, R.D. McBride, H. Wilhelm, S.C. Glidden, S. Grasso, and H.D. Sanders. Capabilities of the reconfigured COBRA accelerator. In *Proceedings of the 15th IEEE International Pulsed Power Conference, 13-17 June 2005, Monterey, CA*, pages 273 –276, 2005.

[37] J. B. Greenly, J. D. Douglas, D. A. Hammer, B. R. Kusse, S. C. Glidden, and H. D. Sanders. A 1-MA, variable risetime pulse generator for high energy density plasma research. *Rev. Sci. Instrum*, 79:073501, 2008.

[38] W. Rogowski and W. Steinhaus. Die Messung der magnetischen Spannung. *Electrical Engineering (Archiv für Elektrotechnik)*, 1:141–150, 1912.

[39] L. A. Vermeulen and A. J. Harris. A diamond radiation detector. *J. Appl. Phys.*, 49:913–916, 1978.

[40] Rick B. Spielman, Lawrence E. Ruggles, Richard E. Pepping, Stephen P. Breeze, John S. McGurn, and Kenneth W. Struve. Fielding and calibration issues for diamond photoconducting detectors. *Rev. Sci. Instrum.*, 68:782–785, 1997.

[41] D. A. Hammer, S. A. Pikuz, and T. A. Shelkovenko. Fly By Night. *Nature Reviews Genetics*, 6(9):Cover, September 2005.

[42] J. D. Douglass, S. A. Pikuz, T. A. Shelkovenko, D. A. Hammer, S. N. Bland, S. C. Bott, and R. D. McBride. Structure of the dense cores and ablation plasmas in the initiation phase of tungsten wire-array Z pinches. *Phys. Plasmas*, 14:012704, 2007.

[43] D. B. Sinars, M. E. Cuneo, G. R. Bennett, D. F. Wenger, L. E. Ruggles, M. F. Vargas, J. L. Porter, R. G. Adams, D. W. Johnson, K. L. Keller, P. K. Rambo, D. C. Rovang, H. Seamen, W. W. Simpson, I. C. Smith, and S. C. Speas. Monochromatic x-ray backlighting of wire-array z-pinch plasmas using spherically bent quartz crystals. *Rev. Sci. Instrum*, 74:2202–2205, 2003.

[44] S. M. Zakharov, G. V. Ivanenkov, A. A. Kolomenksii, S. A. Pikuz, A. I. Samokhin, and J. Ullschmeid. Wire X pinch in a high-current diode. *Sov. Tech. Phys. Lett.*, 8:456, 1982.

[45] D. B. Sinars, S. A. Pikuz, T. A. Shelkovenko, K. M. Chandler, and D. A. Hammer. Temporal parameters of the X-pinch x-ray source. *Rev. Sci. Instrum*, 72:2948–2956, 2001.

[46] T. A. Shelkovenko, S. A. Pikuz, R. D. McBride, P. F. Knapp, H. Wilhelm, D. A. Hammer, and D. B. Sinars. Nested multilayered X pinches for generators with mega-ampere current level. *Phys. Plasmas*, 16:050702, 2009.

[47] T. A. Shelkovenko, S. A. Pikuz, A. D. Cahill, P. F. Knapp, D. A. Hammer, D. B. Sinars, I. N. Tilikin, and S. N. Mishin. Hybrid X-pinch with conical electrodes. *Phys. Plasmas*, 17:112707, 2010.

[48] J. D. Douglass and D. A. Hammer. COBRA-STAR, a five frame point-projection x-ray imaging system for 1-MA scale wire-array Z pinches. *Rev. Sci. Instrum*, 79:033503, 2008.

[49] S. V. Lebedev, F. N. Beg, S. N. Bland, J. P. Chittenden, A. E. Dangor, M. G. Haines, S. A. Pikuz, and T. A. Shelkovenko. Effect of core-corona plasma structure on seeding of instabilities in wire array *Z* pinches. *Phys. Rev. Lett.*, 85:98–101, Jul 2000.

[50] T.A. Pikuz, A.Ya. Faenov, S.A. Pikuz, V.M. Romanova, and T.A. Shelkovenko. Bragg x-ray optics for imaging spectroscopy of plasma microsources. *J. X-Ray Sci. Technol.*, 5:323 – 340, 1995.

[51] S. A. Pikuz, T. A. Shelkovenko, V. M. Romanova, D. A. Hammer, A. Ya. Faenov, V. A. Dyakin, and T. A. Pikuz. High-luminosity monochromatic x-ray backlighting using an incoherent plasma source to study extremely dense plasmas (invited). *Rev. Sci. Instrum.*, 68:740–744, 1997.

[52] T. A. Shelkovenko, D. B. Sinars, S. A. Pikuz, K. M. Chandler, and D. A. Hammer. Point-projection x-ray radiography using an x pinch as the radiation source. *Rev. Sci. Instrum.*, 72(1):667–670, 2001.

[53] S. A. Pikuz, T. A. Shelkovenko, A. R. Mingaleev, D. A. Hammer, and H. P. Neves. Density measurements in exploding wire-initiated plasmas using tungsten wires. *Phys. Plasmas*, 6:4272–4283, 1999.

[54] Prism Computational Sciences Inc. PrismSPECT. http://www.prism-cs.com/Software/PrismSpect/PrismSPECT.htm.

[55] S. N. Bland, S. V. Lebedev, J. P. Chittenden, G. N. Hall, F. Suzuki-Vidal, D. J. Ampleford, S. C. Bott, J. B. A. Palmer, S. A. Pikuz, and T. A. Shelkovenko. Implosion and stagnation of wire array z pinches. *Phys. Plasmas*, 14:056315, 2007.

[56] J. P. VanDevender. private communication, November 2010.

[57] T. J. Awe, B. S. Bauer, S. Fuelling, and R. E. Siemon. Threshold for thermal ionization of an aluminum surface by pulsed megagauss magnetic field. *Phys. Rev. Lett.*, 104:035001, 2010.

[58] S. A. Chaikovsky, V. I. Oreshkin, G. A. Mesyats, N. A. Ratakhin, I. M. Datsko, and B. A. Kablambaev. Electrical explosion of metals in fast-rising megagauss magnetic fields. *Phys. Plasmas*, 16:042701, 2009.

[59] J. C. Martin. *J. C. Martin On Pulsed Power*, pages 295–333. Plenum Press, New York, 1996.

[60] J. D. Douglass. private communication, 2007.

[61] T.A. Shelkovenko, S.A. Pikuz, D.B. Sinars, K.M. Chandler, and D.A. Hammer. X pinch plasma development as a function of wire material and current pulse parameters. *Plasma Science, IEEE Transactions on*, 30(2):567 – 576, apr 2002.

[62] J. D. Douglass. *An Experimental Study of Tungsten Wire-Array Z-Pinch Plasmas Using Time-Gated Point-Projection X-Ray Imaging*. PhD thesis, Cornell University, 2007.

[63] I. C. Blesener, J. B. Greenly, S. A. Pikuz, T. A. Shelkovenko, S. Vishniakou, D. A. Hammer, and B. R. Kusse. Axial x-ray backlighting of wire-array Z-pinches using X pinches. *Rev. Sci. Instrum.*, 80(12):123505, December 2009.

[64] D. B. Sinars, M. E. Cuneo, B. Jones, C. A. Coverdale, T. J. Nash, M. G. Mazarakis, J. L. Porter, C. Deeney, D. F. Wenger, R. G. Adams, E. P. Yu, D. E. Bliss, and G. S. Sarkisov. Measurements of the mass distribution and instability growth for wire-array z-pinch implosions driven by 14–20 ma. *Phys. Plasmas*, 12(5):056303, 2005.

[65] S. V. Lebedev, F. N. Beg, S. N. Bland, J. P. Chittenden, A. E. Dangor, M. G. Haines, K. H. Kwek, S. A. Pikuz, and T. A. Shelkovenko. Effect of discrete wires on the implosion dynamics of wire array z pinches. *Phys. Plasmas*, 8(8):3734–3747, 2001.

[66] P. F. Knapp, J. B. Greenly, P.-A. Gourdain, C. L. Hoyt, M. R. Martin, S. A. Pikuz, C. E. Seyler, T. A. Shelkovenko, and D. A. Hammer. Growth and

saturation of the axial instability in low wire number wire array z pinches. *Phys. Plasmas*, 17(1):012704, 2010.

[67] D. B. Sinars, M. E. Cuneo, E. P. Yu, S. V. Lebedev, K. R. Cochrane, B. Jones, J. J. MacFarlane, T. A. Mehlhorn, J. L. Porter, and D. F. Wenger. Measurements and simulations of the ablation stage of wire arrays with different initial wire sizes. *Phys. Plasmas*, 13(4):042704, 2006.

[68] M. E. Cuneo, D. B. Sinars, E. M. Waisman, D. E. Bliss, W. A. Stygar, R. A. Vesey, R. W. Lemke, I. C. Smith, P. K. Rambo, J. L. Porter, G. A. Chandler, T. J. Nash, M. G. Mazarakis, R. G. Adams, E. P. Yu, K. W. Struve, T. A. Mehlhorn, S. V. Lebedev, J. P. Chittenden, and C. A. Jennings. Compact single and nested tungsten-wire-array dynamics at 14–19 ma and applications to inertial confinement fusion. *Phys. Plasmas*, 13(5):056318, 2006.

[69] C. E. Seyler and M. R. Martin. Relaxation model for extended magnetohydrodynamics: Comparison to magnetohydrodynamics for dense z-pinches. *Phys. Plasmas*, 18(1):012703, 2011.

[70] M. R. Martin. *Generalized Ohms law at the plasma-vacuum interface*. PhD thesis, Cornell University, 2010.